

# SORPTION MODELING AND VERIFICATION FOR OFF-GAS TREATMENT

---

## Fuel Cycle

Dr. Lawrence L. Tavlarides  
Syracuse University

In collaboration with:  
Georgia Institute of Technology  
Prairie View A&M University  
Oak Ridge National Laboratory

Kimberly Gray, Federal POC  
Robert Jubin, Technical POC

# SORPTION MODELING AND VERIFICATION FOR OFF-GAS TREATMENT

**Final Report:** For the period November 1, 2011- December 30, 2014

*Prepared for:*

**U.S. Department of Energy Nuclear Energy University Program**  
NEUP Integration Office  
Center for Advanced Energy Studies  
P.O. Box 1625  
Idaho Falls, ID 83415

Contract No.: NFE-12-03822  
Program Manager: R.T. Jubin

*Prepared by:*

**Lawrence L. Tavlarides**  
**Ronghong Lin**  
**Yue Nan**

Department of Biomedical and Chemical Engineering  
Syracuse University

**Sotira Yiacoumi**  
**Costas Tsouris**  
**Austin Ladshaw**  
**Ketki Sharma**

School of Civil and Environmental Engineering  
Georgia Institute of Technology

**Jorge Gabitto**  
Chemical Engineering Department  
Prairie View A&M University

**David DePaoli**  
Nuclear Security and Isotope Technology Division  
Oak Ridge National Laboratory

February 15, 2015

## SUMMARY

The project has made progress toward developing a comprehensive modeling capability for the capture of target species in off gas evolved during the reprocessing of nuclear fuel. The effort has integrated experimentation, model development, and computer code development for adsorption and absorption processes.

For adsorption, a modeling library has been initiated to include (a) equilibrium models for uptake of off-gas components by adsorbents, (b) mass transfer models to describe mass transfer to a particle, diffusion through the pores of the particle and adsorption on the active sites of the particle, and (c) interconnection of these models to fixed bed adsorption modeling which includes advection through the bed. For single-component equilibria, a Generalized Statistical Thermodynamic Adsorption (GSTA) code was developed to represent experimental data from a broad range of isotherm types; this is equivalent to a Langmuir isotherm in the two-parameter case, and was demonstrated for Kr on INL engineered sorbent HZ PAN, water sorption on molecular sieve 3A sorbent material (MS3A), and Kr and Xe capture on metal-organic framework (MOF) materials. The GSTA isotherm was extended to multicomponent systems through application of a modified spreading pressure surface activity model and generalized predictive adsorbed solution theory; the result is the capability to estimate multicomponent adsorption equilibria from single-component isotherms. This advance, which enhances the capability to simulate systems related to off-gas treatment, has been demonstrated for a range of real-gas systems in the literature and is ready for testing with data currently being collected for multicomponent systems of interest, including iodine and water on MS3A. A diffusion kinetic model for sorbent pellets involving pore and surface diffusion as well as external mass transfer has been established, and a methodology was developed for determining unknown diffusivity parameters from transient uptake data. Two parallel approaches have been explored for integrating the kernels described above into a mass-transport model for adsorption in fixed beds. In one, the GSTA isotherm kernel has been incorporated into the MOOSE framework; in the other approach, a focused finite-difference framework and PDE kernels have been developed. Issues, including oscillatory behavior in MOOSE solutions to advection-diffusion problems, and opportunities have been identified for each approach, and a path forward has been identified toward developing a stronger modeling platform. Experimental systems were established for collection of microscopic kinetics and equilibria data for single and multicomponent uptake of gaseous species on solid sorbents. The systems, which can operate at ambient temperature to 250°C and dew points from -69 to 17°C, are useful for collecting data needed for modeling performance of sorbents of interest. Experiments were conducted to determine applicable models and parameters for isotherms and mass transfer for water and/or iodine adsorption on MS3A. Validation experiments were also conducted for water adsorption on fixed beds of MS3A.

For absorption, work involved modeling with supportive experimentation. A dynamic model was developed to simulate CO<sub>2</sub> absorption with chemical reaction using high alkaline content water solutions. A computer code was developed to implement the model based upon transient mass and energy balances. Experiments were conducted in a laboratory-scale column to determine model parameters. The influence of geometric parameters and operating variables on CO<sub>2</sub> absorption was studied over a wide range of conditions.

This project has resulted in 7 publications, with 3 manuscripts in preparation. Also, 15 presentations were given at national meetings of ANS and AIChE and at Material Recovery and Waste Forms Campaign Working Group meetings.

# Table of Contents

<b>OVERVIEW .....</b>	<b>1</b>
<b>ADSORPTION .....</b>	<b>2</b>
<b>1. EXPERIMENTAL STUDIES ON REMOVAL OF TRITIATED WATER AND RADIOACTIVE IODINE SURROGATES FROM OFF-GASES BY SOLID SORBENTS .....</b>	<b>2</b>
1.1 KEY PERSONNEL .....	2
1.2 SCOPE .....	2
1.3 WATER ADSORPTION ON SOLID SORBENTS .....	2
1.3.1 Introduction .....	2
1.3.2 Experimental setup and materials .....	3
1.3.3 Experimental conditions and procedure .....	6
1.3.4 Adsorption isotherms for water adsorption on MS 3A.....	6
1.3.5 Adsorption kinetics of water adsorption on MS 3A.....	10
1.3.6 Adsorption cycle test.....	22
1.3.7 Water adsorption-desorption column tests .....	24
1.3.8 Water adsorption on AgZ.....	24
1.4 IODINE ADSORPTION ON SOLID SORBENTS .....	25
1.4.1 Introduction .....	25
1.4.2 Experiments setup.....	26
1.4.3 Iodine adsorption on MS 3A - continuous flow experiment .....	28
1.5 SUMMARY .....	30
2.1 KEY PERSONNEL .....	31
2.2 SCOPE .....	31
2.3 MODELING APPROACH.....	31
<b>ACRONYM .....</b>	<b>32</b>
<b>NAME .....</b>	<b>32</b>
2.4 PARTIAL DIFFERENTIAL EQUATION KERNELS .....	33
2.4.1. MACAW.....	33
2.4.2. LARK .....	33
2.4.3. FINCH .....	35
2.5 EQUILIBRIA KERNELS .....	39
2.5.1 GSTA.....	39
2.5.2 MSPD .....	45
2.5.3 GPAST.....	47
2.5.4 MAGPIE .....	49
2.6 KINETIC KERNELS.....	51
2.6.1 SKIMMER .....	51
2.6.2 SKUA .....	55
2.7 TRANSPORT MODELING .....	59
2.7.1 OSPREY and the MOOSE Framework .....	59
2.7.2. FALCON .....	63



2.8 USER REQUIREMENTS AND DOCUMENTATION .....	65
2.9 CONCLUSIONS AND PATH FORWARD.....	65
<b>ABSORPTION .....</b>	<b>67</b>
<b>3. CO<sub>2</sub> ABSORPTION MODELING.....</b>	<b>67</b>
3.1 KEY PERSONNEL .....	67
3.2 SCOPE .....	67
3.3 TASK AND DESCRIPTION OF MAJOR MILESTONES: .....	67
3.4 TECHNICAL DESCRIPTION .....	68
3.4.1 <i>Dynamic Model</i> .....	68
3.4.2 <i>Solution Procedure</i> .....	76
3.4.3. <i>Experimental Part</i> .....	78
3.5 RESULTS AND DISCUSSION.....	82
4.4.1 <i>Experimental Results</i> .....	82
4.4.2 <i>Dynamic Simulation Results</i> .....	87
3.6 SUMMARY .....	103
<b>REFERENCES.....</b>	<b>105</b>
REFERENCES FOR SECTION 1.....	105
REFERENCES FOR SECTION 2.....	106
REFERENCES FOR SECTION 3.....	108
<b>PUBLICATIONS AND PRESENTATIONS.....</b>	<b>111</b>

## OVERVIEW

Future fuel recycling systems will be required to capture volatile fission products, including from dilute streams, with very high separation factors. This project has supported the efforts of the Material Recovery & Waste Form Development Campaign of the Fuel Cycle Technology Program toward the establishment of efficient off-gas treatment technologies by developing modeling capabilities for relevant adsorption and absorption processes. Process modeling can accelerate development of environmentally compliant recycle systems, by enabling prediction of the performance of off-gas treatment components under a variety of dynamic process conditions.

Adsorption modeling for the separation and recovery of radioisotopic gases in the off-gas stream of nuclear fuel reprocessing is a complicated, multi-scale problem involving tightly coupled systems of partial differential equations. The approach to modeling such a system is equally complicated and inevitably involves providing a methodology that can link the dependent variables across a range of scales, from as small as the molecular scale for molecule-molecule and molecule-surface interactions to as large as the macroscopic scale for systems design and engineering. Absorption processes represent dynamic, multicomponent systems dependent on mass transfer and reaction. The performance of process models for these systems is only as good as the parameters used in the models; experimental data are needed to accurately represent the equilibrium loading, as well as the mass-transfer characteristics of sorbates with sorbent materials of interest.

This project has involved the collaboration of researchers at Syracuse University, Georgia Institute of Technology, Prairie View A&M University, and Oak Ridge National Laboratory, with integrated efforts on experimentation, model development, and computer code development for adsorption and absorption processes. To ensure relevance of the work, interactions were conducted throughout the project with Off-Gas Sigma Team researchers at Idaho National Laboratory, Oak Ridge National Laboratory, and Pacific Northwest National Laboratory.

This report summarizes progress in the project with the following structure:

Section 1 – Adsorption Experimental Studies

Section 2 – Adsorption Model Development

Section 3 – Absorption Model Development and Experimental Validation

# **ADSORPTION**

## **1. Experimental studies on removal of tritiated water and radioactive iodine surrogates from off-gases by solid sorbents**

### **1.1 Key personnel**

Lawrence L. Tavlarides (PI), Ronghong Lin (Research Associate), Yue Nan (Graduate Student), Syracuse University

### **1.2 Scope**

The objective of this portion of the project was to establish an experimental capability to obtain fundamental equilibrium and kinetic data for application to adsorption of radioactive gases on solid sorbents, and to demonstrate the capability by collecting data relevant to modeling the capture of iodine and tritiated water. Single-component adsorption equilibrium data were obtained to determine the adsorption capacity and to evaluate the parameters of equilibrium models. Some multi-component equilibrium data were obtained at selected conditions for future evaluation of predictive multi-component equilibrium models that will be based on single-component isotherms. Kinetic data were obtained to determine the intraparticle mass transfer and reaction parameters for the adsorption models. Adsorption systems studied include (1) water adsorption on molecular sieve (MS) 3A, (2) water adsorption on silver-exchanged mordenite, (3) iodine adsorption on MS 3A, and (4) water/iodine co-adsorption on MS 3A.

### **1.3 Water adsorption on solid sorbents**

#### **1.3.1 Introduction**

The removal and immobilization of tritium from spent nuclear fuels are important for reducing tritium emissions into the environment. The state-of-the-art in tritium removal is represented by converting tritium to tritiated water followed by adsorption on solid sorbents. The selective removal of tritiated water vapor from spent fuel reprocessing off-gases by various sorbents has been proposed and widely investigated.<sup>1-8</sup> These sorbents include silica gel, molecular sieves (3A, 4A, 5A, 13X), Drierite and activated alumina, among which molecular sieves have been most widely used for removal and temporary storage of tritiated water.

Design of high efficient adsorption systems and modeling and simulation of adsorption bed dynamics require experimental data on adsorption isotherms and on adsorption kinetic parameters. To serve this purpose, water adsorption on single-layer of MS 3A over a wide range of adsorption temperature and water vapor pressure was investigated. Adsorption isotherms were determined and water uptake dynamics were modeled. In addition, isotherms of water adsorption on AgZ were obtained for the future modeling of iodine and water co-adsorption on AgZ.

### 1.3.2 Experimental setup and materials

A continuous flow adsorption system was developed for the study of water adsorption on solid sorbents. A schematic diagram of the system is shown in **Figure 1** and a photograph is shown in **Figure 2**. Known amount of sorbent was loaded on a screen pan hanging on a microbalance inside a sample tube as shown in **Figure 3**. Air of controlled water vapor pressure was passing upward over the sample and through the sample tube. Dynamic water uptakes were measured by the microbalance (CI Precision, UK) and recorded by the data acquisition system. The balance head had a loading capacity of 5 g (5 g for sample and 5 g for counterweight), a dynamic weighing range of  $\pm 500$  mg (weight gain or loss), and sensitivity of 0.1  $\mu$ g. The head was purged with nitrogen at a flow rate of less than 50 ml/min to prevent the damage of the head due to adsorption carrier gas on the head. The balance was connected to and controlled by a balance control unit that was connected to a data acquisition system.

Water vapor was generated by bubbling water in a controlled manner. Dry air from a gas cylinder was split into two streams, the carrier stream and the makeup stream, controlled by two mass flow controllers. The carrier stream passed through 1-3 glass tubes containing deionized water. The glass tubes were immersed in a water bath, the temperature of which was controlled at a value between 4-20 °C. By controlling the gas flow rates of the two streams and water temperature, desired water concentrations were produced. The water vapor pressures (dew points) were measured by a hygrometer (Easidew Online, Michell Instruments) by passing the gas stream through a gas sampler (Easidew Sampler, Michell Instruments). Adsorption temperature was controlled by a second water bath.

The MS 3A used in this work is the UOP type zeolite 3A (CAS#:308080-99-1; Product #: 208582; Lot #: MKBH6237V) purchased from Sigma-Aldrich. The chemical composition of this adsorbent provided by the supplier is  $K_{7.2}Na_{4.8}(AlO_2)_{12}(SiO_2)_{12} \cdot x H_2O$ . Characteristics of the adsorbent are given in **Table 1**. The sorbents received from the supplier were 8-12 mesh beads. The beads were further sieved by an 8-mesh stainless steel screen to narrow down the pellet size distribution, and the measured average radius of the pellets was 1.18 mm. The macroporosity and density of the pellets determined by a third party by Mercury Porosimetry were 0.272 and 1.690  $\pm$  0.001 g/ml, respectively. Molecular sieve beads are composed of microparticles (or crystals) and binder materials. The size of the microparticles of the MS 3A was 1.5-2.5  $\mu$ m in radius assuming spherical particles, as indicated by the supplier. The theoretical equilibrium water adsorption capacities of the MS 3A powder (without binder material) and beads were 23 wt% and 21 wt%, respectively, as indicated by the supplier. Assuming that the binder material does not adsorb water, the corresponding content of binder material in the MS 3A was about 9 wt%.

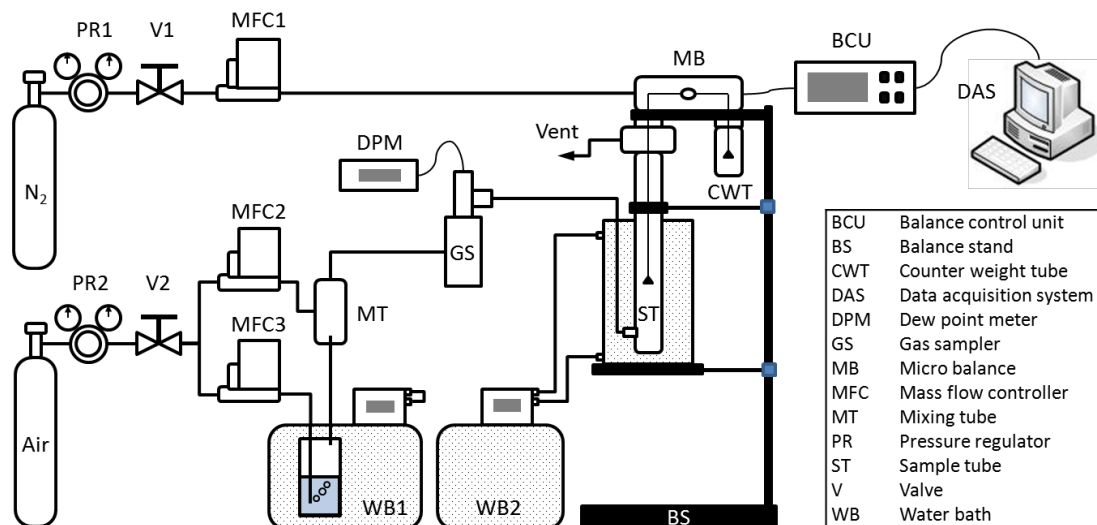


**Figure 1. Schematic diagram of the continuous-flow water adsorption system.**

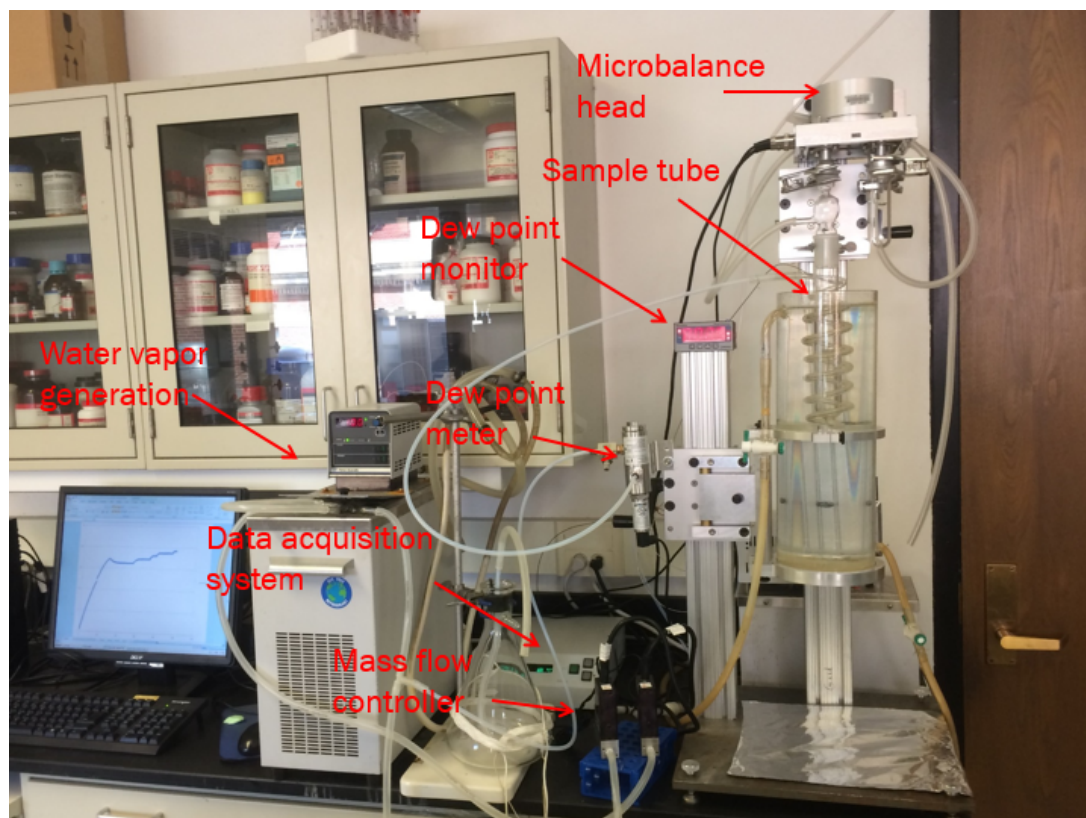


**Figure 2. A photograph of the water adsorption system.**

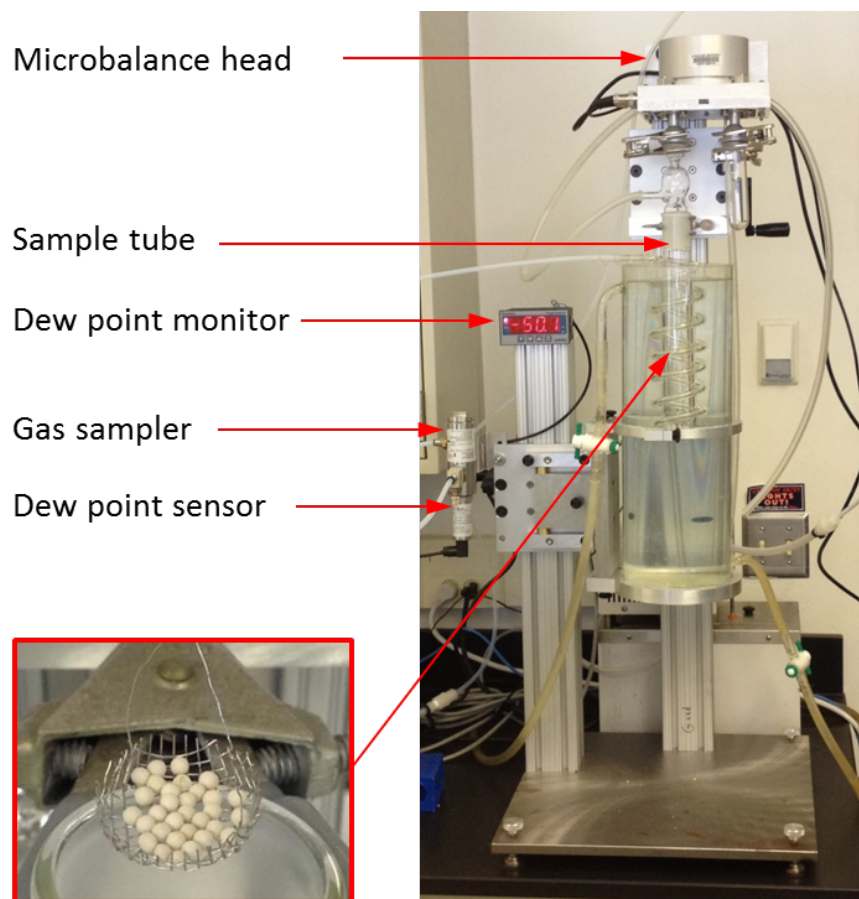


**Figure 3. Photos of the adsorption unit (right) and the stainless steel screen pan with single-layer sorbents loaded (left).**

**Table 1. Properties and characteristics of molecular sieve 3A used in this study.<sup>a</sup>**

Properties/Characteristics	Value
Form	Bead
Moisture, %	1.5
Equilibrium H <sub>2</sub> O capacity (theory), %	21
Regeneration temperature, °C	175-260
Radius of pellets ( $R_p$ ), mm	1.18 <sup>b</sup> (8 mesh)
Radius of microparticles (crystals) ( $R_c$ ), $\mu\text{m}$	1.5-2.5
Macroporosity ( $\epsilon_p$ )	0.272 <sup>b</sup>
Pellet density ( $\rho_p$ ), g/cm <sup>3</sup>	1.690 $\pm$ 0.001 <sup>b</sup>

<sup>a</sup> The data shown in the table are provided by the material supplier, unless noted in the table.

<sup>b</sup> These values were measured in this study.

### 1.3.3 Experimental conditions and procedure

The MS 3A was degased using the ASAP 2020 Physisorption Analyzer to remove residual water prior to use. Degasing was performed under vacuum at 230 °C for 8 hours to a final pressure of less than 0.5 Pa. All samples were degased and stored for less than one day before use to minimize uncertainty caused by possible water adsorption on the sorbents during storage in the degas tube.

The adsorption system was run for several hours to several days to establish desired experimental conditions. The pre-running duration was largely dependent of the desired dew points. After establishment of the desired condition, degased MS 3A (~ 0.27 g) was loaded onto the stainless steel screen pan, and water uptake data were recorded. Adsorption experiments were conducted at 25, 40, 60 and 80 °C over a wide range of dew points from -69 °C to 17 °C. The total gas flow rate was set to a value between 0.050-1.400 L/min for all runs, and the corresponding gas velocity inside the sample tube was 0.001-0.033 m/s, considering a tube inner diameter of 0.3 cm.

### 1.3.4 Adsorption isotherms for water adsorption on MS 3A

Water adsorption isotherms were measured at adsorption temperature of 25, 40, 60, and 80 °C and over water dew points from -70 to 20 °C (or water vapor pressure from 0.001 to 15 hPa). Results shown in **Figure 4** indicate that the water uptake capacity increases with water vapor pressure but decreases with adsorption temperature.

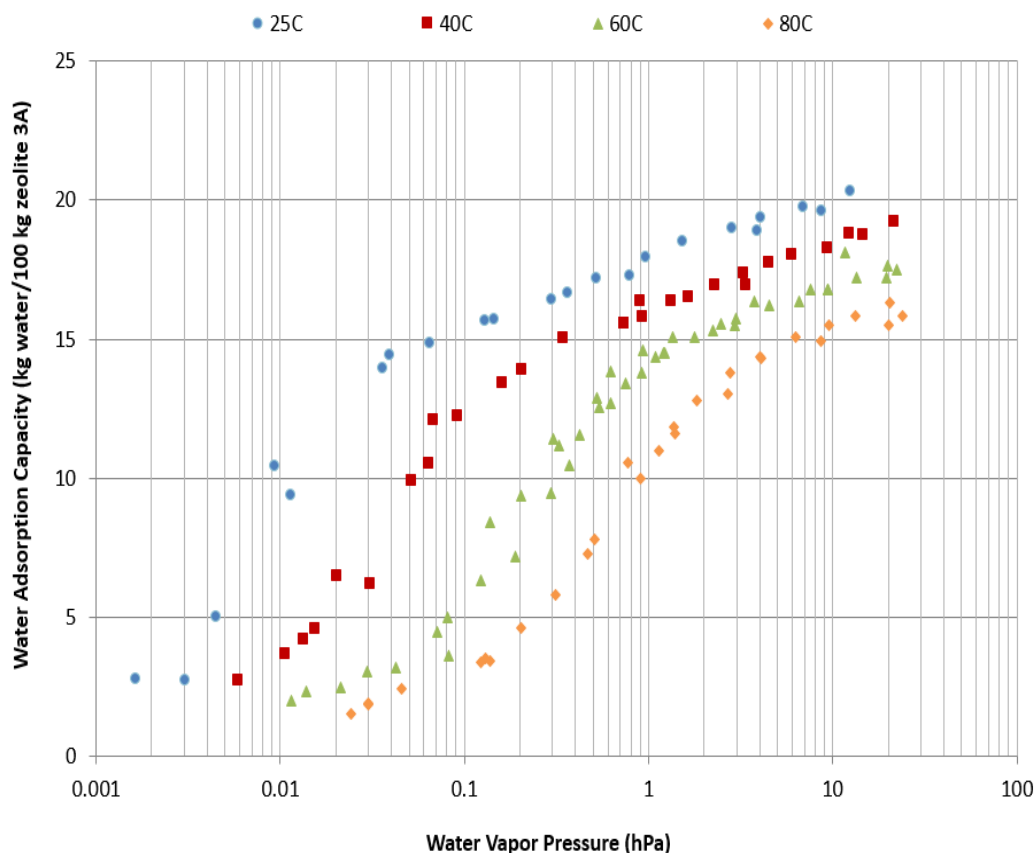


**Figure 4.** Adsorption isotherms for water adsorption on MS 3A at 25, 40, 60 and 80 °C.

As shown in **Table 2**, several models have been previously applied to model zeolite adsorption isotherms. These models include the GSTA model, the Langmuir model, the Toth model, the Slips model, the UNILAN model, and the Dubinin-Astakhov model.<sup>9</sup> These models were examined with water adsorption data obtained in this work by nonlinear curve fitting with MATLAB function *lsqcurvefit* to minimize the following objective function.

$$F_{\text{obj}} = \frac{1}{N} \sum_{i=1}^N (C_{\text{calc},i} - C_{\text{exp},i})^2 \quad (1)$$

**Table 2. Isotherm models previously used for modeling zeolite adsorption isotherms.**<sup>9</sup>

Model	Equation	Parameters
GSTA	$\frac{q_e}{q_m} = \frac{1}{m} \left[ \frac{\sum_{n=1}^m n K_n p^n}{1 + \sum_{n=1}^m K_n p^n} \right]$	$q_m, m, K_i$
Langmuir	$\frac{q_e}{q_m} = \frac{bp}{1 + bp}$	$q_m, b$
Toth	$\frac{q_e}{q_m} = \frac{bp}{[1 + (bp)^n]^{1/n}}$	$q_m, b, n$
Slips	$\frac{q_e}{q_m} = \frac{(bp)^{1/n}}{1 + (bp)^{1/n}}$	$q_m, b, n$
UNILAN	$\frac{q_e}{q_m} = \frac{1}{2n} \ln \left[ \frac{1 + bp \exp(n)}{1 + bp \exp(-n)} \right]$	$q_m, b, n$
Dubinin-Astakhov	$\frac{q_e}{q_m} = \exp \left\{ - \left[ \frac{RT}{E} \ln \left( \frac{p^{sat}}{p} \right) \right]^n \right\}$	$q_m, E, n$

**Figure 5** shows an example of the curve-fitting of water adsorption isotherm at 60 °C by these models. The results indicate that the GSTA model has a best fit of the isotherm data, which agrees well with a previous study.<sup>9</sup> Therefore, the GSTA model was used to model water adsorption isotherms and incorporated into the column adsorption model being developed. **Figure 6** shows the modeling of water adsorption isotherms with the GSTA model (see section 2.5.1). A nearly perfect agreement between the prediction and experimental data is shown in the plot.



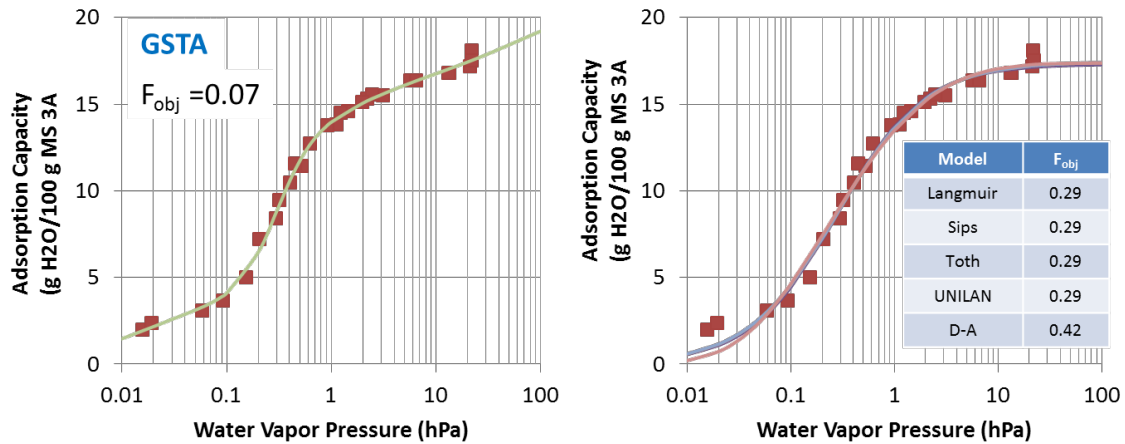


**Figure 5.** Curve fitting of water adsorption isotherm at 60 °C with different isotherm models, showing the best fit by the GSTA model.

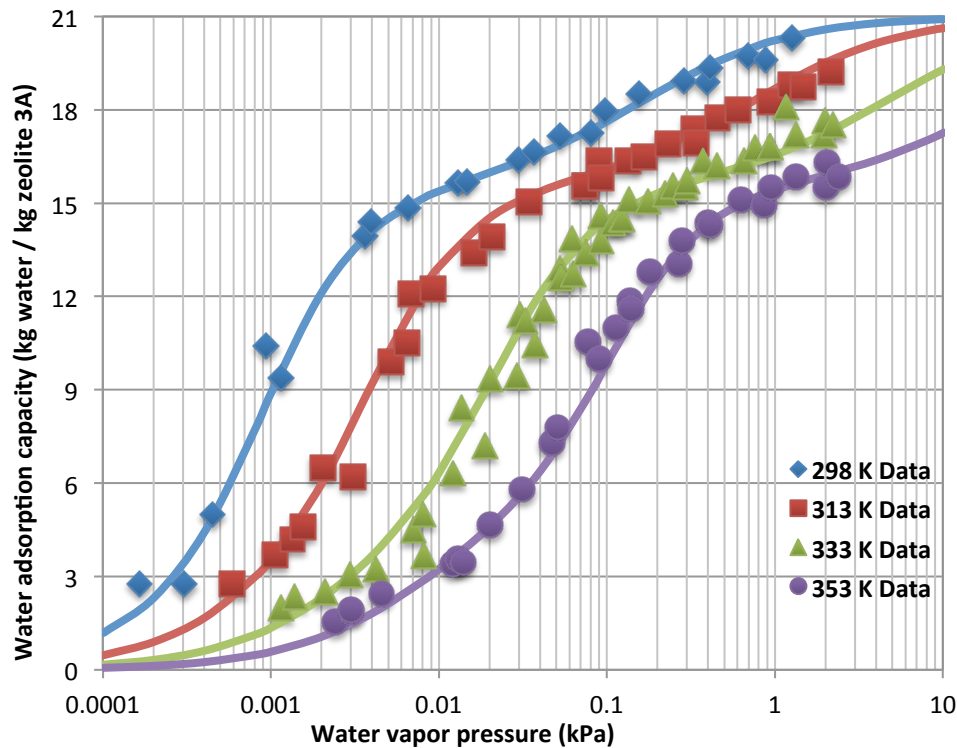


**Figure 6.** Prediction of water adsorption capacity by GSTA model. Dots are experimental data and solid lines are model prediction.

**Figure 7** shows a comparison of current experimental data with literature data<sup>10</sup>, and large differences were found between the two groups of isotherm data. The differences could be caused by difference adsorption characteristics of binder materials, by the effect of cations in zeolites and by difference properties of sorbent such as porosity and effective pore volume. The

commercial UOP zeolite 3A used in this work contained 43 mol%  $K^+$  and 57 mol%  $Na^+$ , while the MS 3A reported in the literature, produced by Grace Davison (GD), contained 38 mol%  $K^+$  and 62 mol%  $Na^+$ . The elemental analysis of UOP zeolite 3A was done with both inductively coupled plasma atomic emission spectroscopy (ICP-OES) and energy dispersive spectroscopy (EDS), and the results agreed well. The GD zeolite 3A was analyzed with EDS. Experiments were done to study the first two possible reasons for the differences between the data.

To investigate the adsorption capacity of binder materials in the MS 3A beads, a water adsorption isotherm on commercial UOP MS 3A powder was obtained at 40 °C. This powder contains only MS 3A crystals which were received from the same supplier and have the same cation composition as the MS 3A beads used in this work. Results are plotted in **Figure 7**. Considering that the beads contain 10% binder material, an isotherm for 90% of the adsorption capacity of the powder crystals was also plotted. It was found that this isotherm agreed very well with the isotherm for MS 3A beads, which suggests that the binder material does not adsorb water and has no effect on adsorption isotherms.

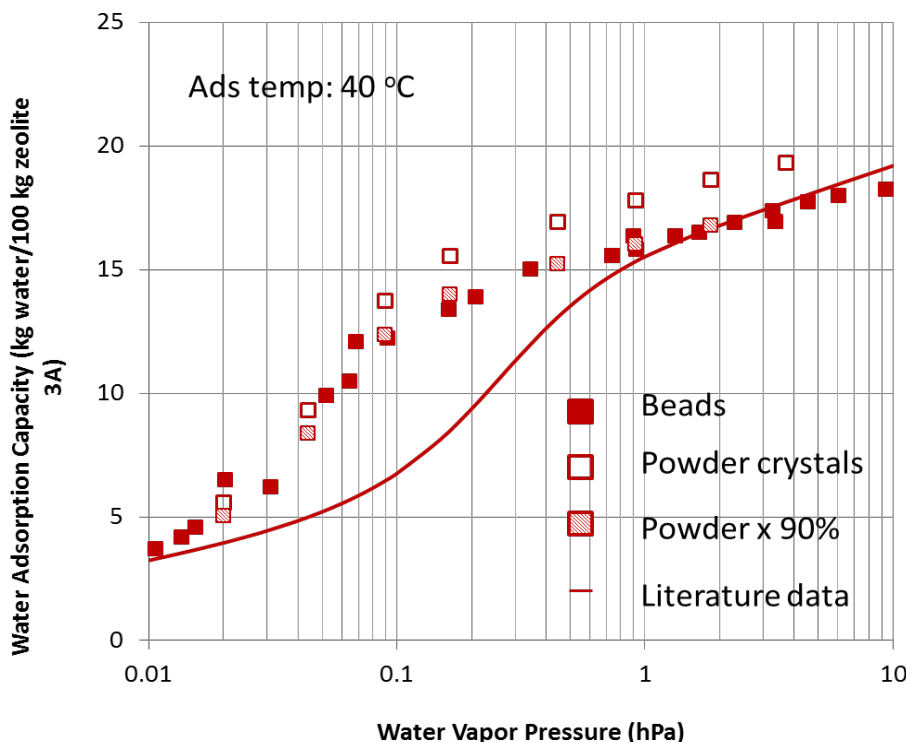


**Figure 7. Adsorption isotherms for zeolite beads (with binder material) and powder crystals and a comparison with literature data.**

In order to study effects of the cation composition on the isotherms, experiments of water adsorption on zeolite sorbents with different molar ratio of  $Na^+$  and  $K^+$  were conducted. The UOP MS 3A crystals contained 50 %  $K^+$  and 50 %  $Na^+$ , and UOP MS 4A crystals contained 100 %  $Na^+$  were received from the same supplier. A cation exchange experiment with the MS 3A crystals was performed to make the crystals with 100%  $K^+$ . The cation composition in these sorbents was determined by ICP-OES.

Isotherms for water adsorption on these sorbents were plotted in **Figure 8**, and the isotherms for MS 3A beads and literature data were plotted as well. For easier comparison, the isotherms of 90% of the adsorption capacity of the crystals were plotted, considering that the beads contain 10% binder material. The data demonstrates the effect of cation composition on the adsorption capacity of the sorbents. However, as shown in the plot, the differences between the isotherms due to the differences of  $\text{Na}^+$  and  $\text{K}^+$  molar ratio in the sorbents cannot explain the differences between the current experimental data and the literature data, which suggests that there are other reasons that cause the differences. The water adsorption experiment with GD MS 3A in our water adsorption experimental system is in progress to further investigate the cause of the discrepancy between the experimental results and published data.

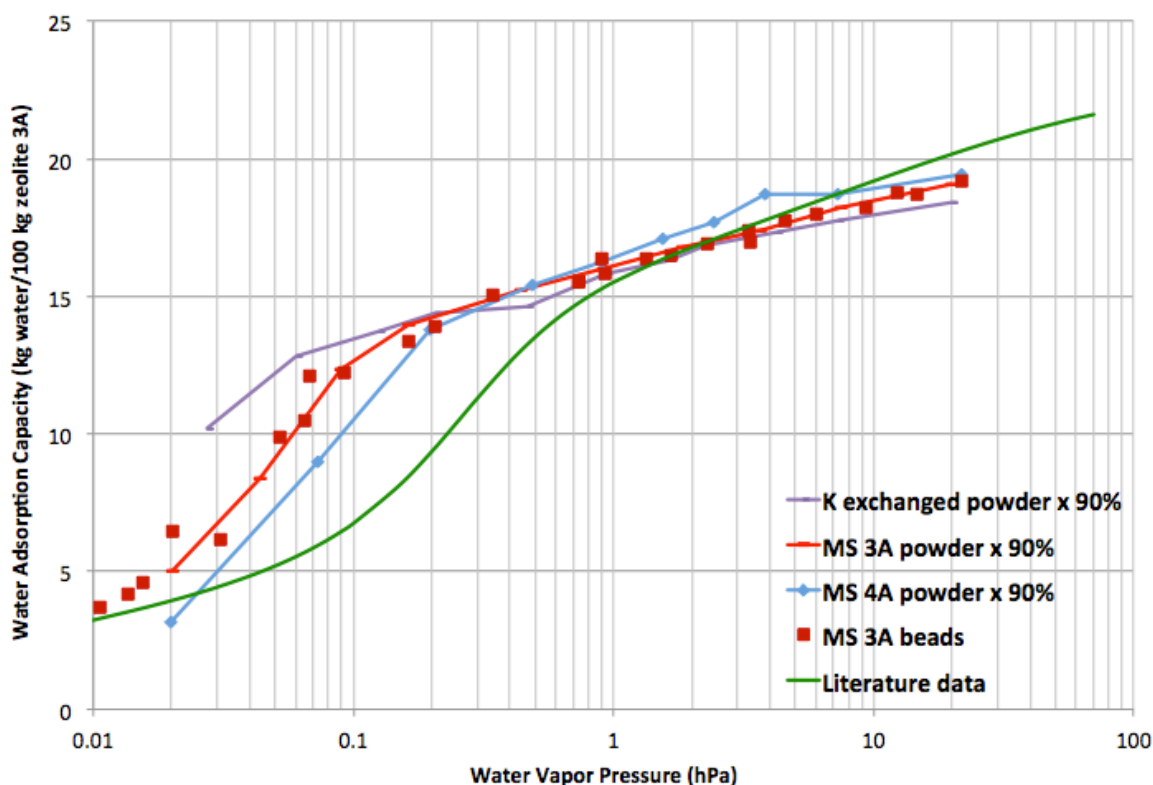


**Figure 8.** Isotherms of water adsorption on different zeolite sorbents at 40 °C.

### 1.3.5 Adsorption kinetics of water adsorption on MS 3A

#### 1.3.5.1 Water uptake curves and kinetic models

Water uptake curves were obtained at adsorption temperature of 25, 40, 60 and 80 °C and at water dew points from -68.9 °C to 17.0 °C. Results plotted in **Figure 9** show that as the water dew point decreased, the equilibrium water uptake capacity decreased and the time required to reach equilibrium significantly increased. For example, at 25 °C, it took less than one hour to reach adsorption equilibrium at a dew point of 10.1 °C. At the same adsorption temperature,

however, it took more than 500 hours to reach equilibrium when the dew point reduced to -68.9 °C.

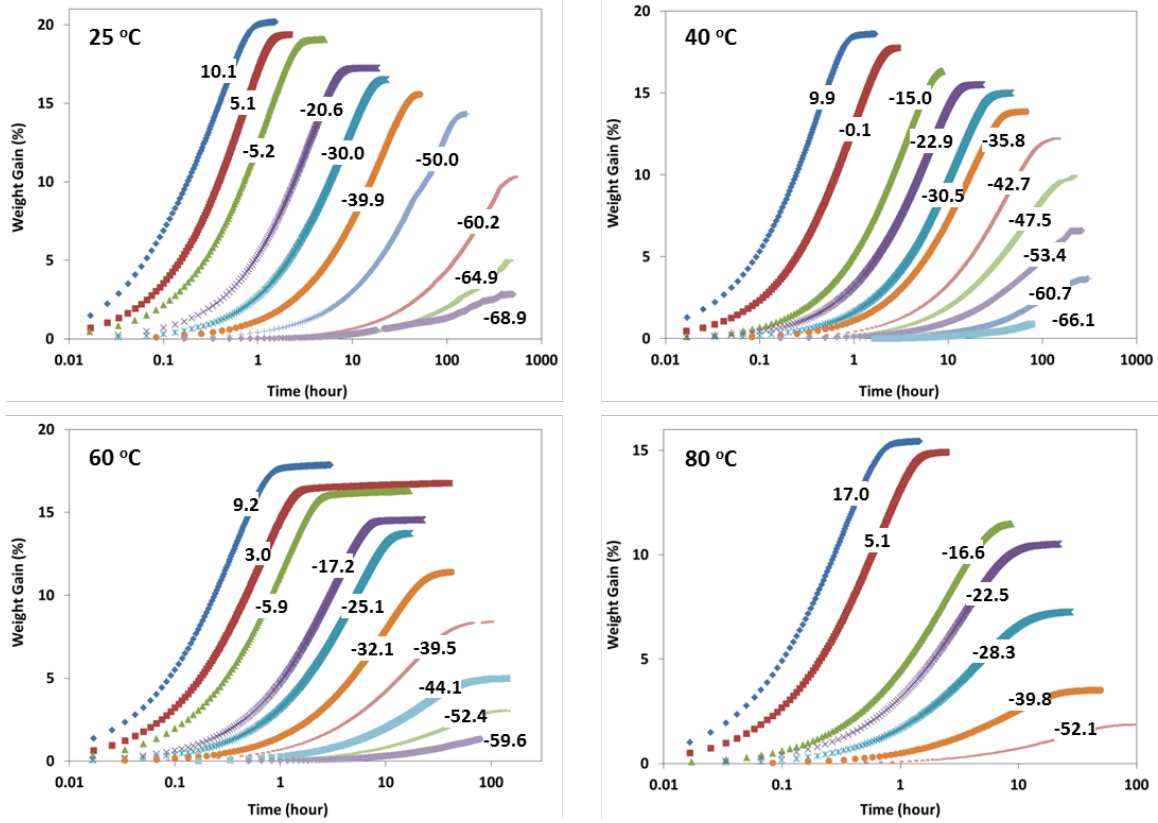


**Figure 9. Water adsorption uptake curves at 24, 40, 60 and 80 °C.**

Several adsorption kinetic models, as listed in **Table 3**, were examined to fit water adsorption uptake curves. They are the linear-driving-force (LDF) model, the shrinking-core (SC) model, the Langmuir kinetic model, the  $x^{\text{th}}$ -order model, the Elovich model and the Weber Morris model.<sup>11-17</sup> The last two models, the Elovich model and the Weber Morris model, were found unable to fit the experimental data, and the  $x^{\text{th}}$ -order model is essentially an empirical model that is connected with the LDF model. Therefore, the first three models, the LDF, SC and Langmuir models, were evaluated.<sup>18</sup> The three models are briefly described below.

### LDF Model

The LDF model, originally proposed by Gleuckauf and Coates in 1947,<sup>11</sup> has been widely used in modeling adsorption kinetics due to its analytical simplicity. According to this model, the average sorbate uptake rate is given by the product of the amount required to reach equilibrium and the so-called LDF mass transfer coefficient, as given by Eq. (2):

$$\frac{d\bar{q}}{dt} = k_{LDF} (q_e - \bar{q}) \quad (2)$$

**Table 3. Adsorption kinetic models.**

Name	Formula	Linear Plot	Slope	Intercept
Linear-driving-force model	$\frac{d\bar{q}}{dt} = k_{LDF} (q_e - \bar{q})$	$\ln\left(\frac{q_e - \bar{q}}{q_e}\right)$ vs $t$	$-k_{LDF}$	0
Shrinking-core model	$t = \frac{\bar{q}}{q_e} \tau_1 + \left(1 + 2\left(1 - \frac{\bar{q}}{q_e}\right) - 3\left(1 - \frac{\bar{q}}{q_e}\right)^{2/3}\right) \tau_2$	$\frac{\bar{q}}{q_e}$ vs $t$	$\frac{1}{\tau_1}$	0
		$\left(1 + 2\left(1 - \frac{\bar{q}}{q_e}\right) - 3\left(1 - \frac{\bar{q}}{q_e}\right)^{2/3}\right)$ vs $\left(t - \frac{\bar{q}}{q_e} \tau_1\right)$	$\frac{1}{\tau_2}$	0
Langmuir kinetic model	$\frac{d\bar{q}}{dt} = k_a C_b (q_m - \bar{q}) - k_d \bar{q}$	$\frac{d\bar{q}}{dt}$ vs $\bar{q}$	$-(k_a C_b + k_d)$	$k_a C_b q_m$
X <sup>th</sup> -order kinetic model	$\frac{d\bar{q}}{dt} = k_X (q_e - \bar{q})^X$	$\ln\left(\frac{d\bar{q}}{dt}\right)$ vs $\ln(q_e - \bar{q})$	$X$	$\ln(k_X)$
Elovich model	$\frac{d\bar{q}}{dt} = A e^{-B\bar{q}}$	$\ln\left(\frac{d\bar{q}}{dt}\right)$ vs $\bar{q}$	$-B$	$\ln A$
Weber-Morris model	$\bar{q} = k_{WM} t^{1/2}$	$\bar{q}$ vs $t^{1/2}$	$k_{WM}$	0

where  $\bar{q}$  and  $q_e$  are the transient average sorbate concentration in sorbents and the equilibrium sorbate concentration in sorbents, respectively, and  $k_{LDF}$  is the LDF mass transfer coefficient.

Integrating Eq. (2) results in Eq. (3), and  $k_{LDF}$  can be obtained from the  $\ln\left(\frac{q_e - \bar{q}}{q_e}\right)$  vs  $t$  plot.

$$\ln\left(\frac{q_e - \bar{q}}{q_e}\right) = -k_{LDF} t \quad (3)$$

Assuming a linear isotherm, it can be shown that the LDF mass transfer resistance has the following expression:<sup>11</sup>

$$\frac{1}{k_{LDF}} = \frac{R_p}{3k_f} \frac{q_e \rho_p}{C_b} + \frac{R_p^2}{15\varepsilon_p D_p} \frac{q_e \rho_p}{C_b} + \frac{R_c^2}{15D_c} \quad (4)$$

where  $C_b$  is the bulk gas-phase concentration,  $D_c$  is the micropore diffusivity,  $D_p$  is the macropore diffusivity,  $k_f$  is the film mass transfer coefficient,  $R_c$  is the radius of micropore,  $R_p$  is the radius of pellet,  $\varepsilon_p$  is the porosity of pellet, and  $\rho_p$  is the density of pellet. The three terms in the right-hand side of Eq. (4), from left to right, are external film resistance, macropore resistance and micropore resistance, respectively.  $C_b$  can be calculated from water vapor pressure assuming ideal gas behavior.

### The shrinking-core model

The SC model is also frequently used in modeling adsorption kinetics. This model simplifies the adsorption process to three sequential steps:<sup>12, 13</sup>

- 1) Diffusion through external gas film.
- 2) Diffusion through saturated shell.

3) Adsorption at the surface of the sorbate-free core.

Assuming that the adsorption step occurs sufficiently more rapidly than the two diffusion steps, the sorbate uptake curve can be expressed implicitly by the  $t = f(\bar{q})$  function as

$$t = \frac{\bar{q}}{q_e} \tau_1 + \left( 1 + 2\left(1 - \frac{\bar{q}}{q_e}\right) - 3\left(1 - \frac{\bar{q}}{q_e}\right)^{2/3} \right) \tau_2 \quad (5)$$

The two parameters  $\tau_1$  and  $\tau_2$  are the characteristic diffusion times for diffusion through external gas film and diffusion through saturated shell, respectively. They are given by<sup>13</sup>

$$\tau_1 = \frac{R_p}{3\varepsilon_p k_f} \frac{q_e \rho_p}{C_b} \quad (6)$$

$$\tau_2 = \frac{R_p^2}{6\varepsilon_p D_p} \frac{q_e \rho_p}{C_b} \quad (7)$$

This model has been successfully used for the analysis of water uptake curves at or near ambient temperature in molecular sieve adsorbents.<sup>12</sup>

Assuming that the external gas film diffusion dominates in the very initial stage (up to 15% weight gain) of the overall adsorption process,  $\tau_1$  can be determined from the  $\bar{q}/q_e$  vs  $t$  plot.

$\tau_2$  can then be determined from the  $\left(1 + 2\left(1 - \frac{\bar{q}}{q_e}\right) - 3\left(1 - \frac{\bar{q}}{q_e}\right)^{2/3}\right)$  vs  $\left(t - \frac{\bar{q}}{q_e} \tau_1\right)$  plot. **Figure 10**

illustrates the determination of  $\tau_1$  and  $\tau_2$ .

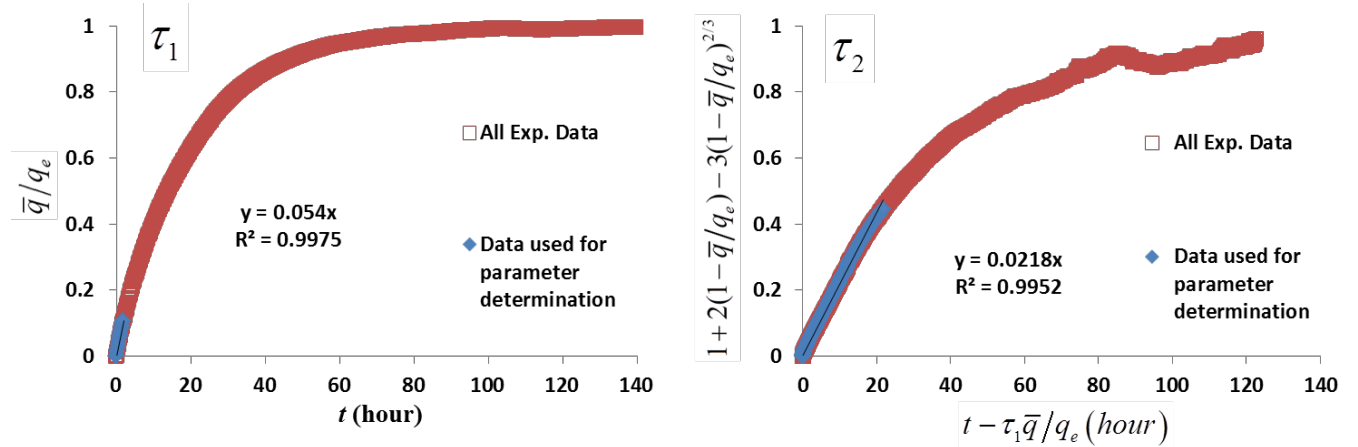


**Figure 10. Determination of  $\tau_1$  and  $\tau_2$  in the shrinking-core model. Adsorption temperature: 60 °C; dew point: -44.1 °C**

### The Langmuir kinetic model

According to the Langmuir kinetic model, the adsorption process is actually a dynamic adsorption and desorption process, and the rate of sorbate uptake is given by the difference between the rate of adsorption and the rate of desorption, as given by Eq (8):<sup>14</sup>

$$\frac{d\bar{q}}{dt} = k_a C_b (q_m - \bar{q}) - k_d \bar{q} \quad (8)$$

Here,  $k_a$  and  $k_d$  are temperature-dependent adsorption and desorption constants, respectively, and  $q_m$  is the maximum sorbate concentration in sorbents. In this work,  $q_m$  equals to 21 wt% (dry sorbents).

Although the Langmuir model was developed out of the surface reaction mechanism<sup>15</sup> and may not be applicable to water adsorption on zeolites which is controlled by mass diffusion,<sup>15</sup> this model is considered for kinetic data analysis because the Langmuir isotherm model has been widely used for modeling isotherms of gas adsorption on zeolites. The current analysis and discussion will provide a new insight into the application of this model in gas-solid adsorption systems.

### 1.3.5.2 Effect of superficial gas velocity

Superficial gas velocity influences adsorption kinetics by changing external gas film resistance. Test adsorption experiments were conducted to demonstrate this effect of superficial gas velocity on water adsorption kinetics and to determine an optimal superficial gas velocity. Water uptake curves were obtained at two difference adsorption temperatures (25 and 40 °C) and three different dew points (5, 10 and 11 °C) and at varying superficial gas velocities. The superficial gas velocity was simply defined by the gas flow rate divided by the cross section area of the sample tube. The gas flow rate varied from 0.05 to 1.4 L/min, and the corresponding superficial gas velocity varied from 0.001 to 0.033 m/s.

Water uptake curves obtained from the test runs were fitted by the LDF model, and the LDF mass transfer coefficients were determined for different adsorption conditions. The LDF mass transfer resistance, which is the reciprocal of the LDF mass transfer coefficient, was plotted in **Figure 11** as a function of superficial gas velocity. It was found that the LDF mass transfer resistance generally decreased as the superficial gas velocity increased to a transitional point, beyond which the LDF mass transfer resistance slightly increased. This transitional superficial gas velocity varied from 0.014 m/s (0.6 L/min) to 0.028 m/s (1.2 L/min) depending on adsorption temperature and water dew point, as shown in **Figure 11**. The results also suggested that the dew point played a more important role than the adsorption temperature did, and a higher dew point led to lower mass transfer resistance.

One single superficial gas velocity was applied throughout the other experiments, which was 0.024 m/s (1 L/min).

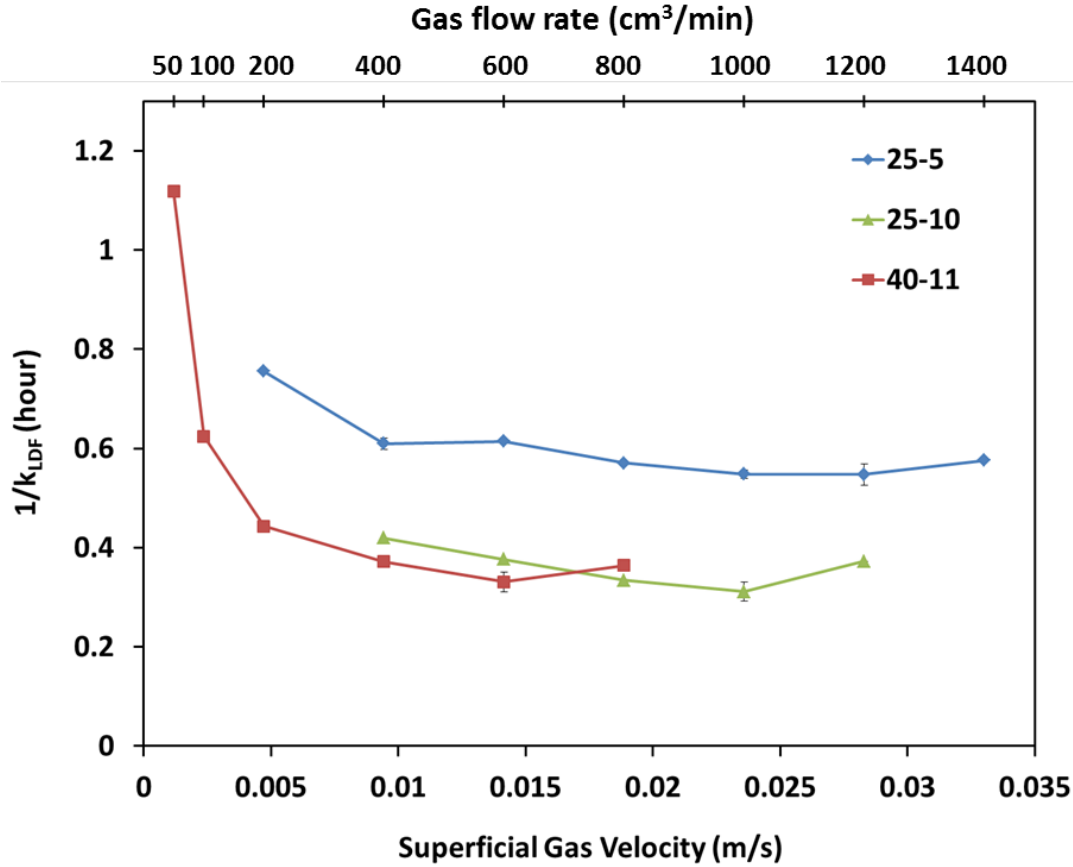


Figure 11. Effect of superficial gas velocity on the LDF mass transfer resistance. Adsorption temperature: 25 and 40 °C; dew point: 5, 10 and 11 °C.

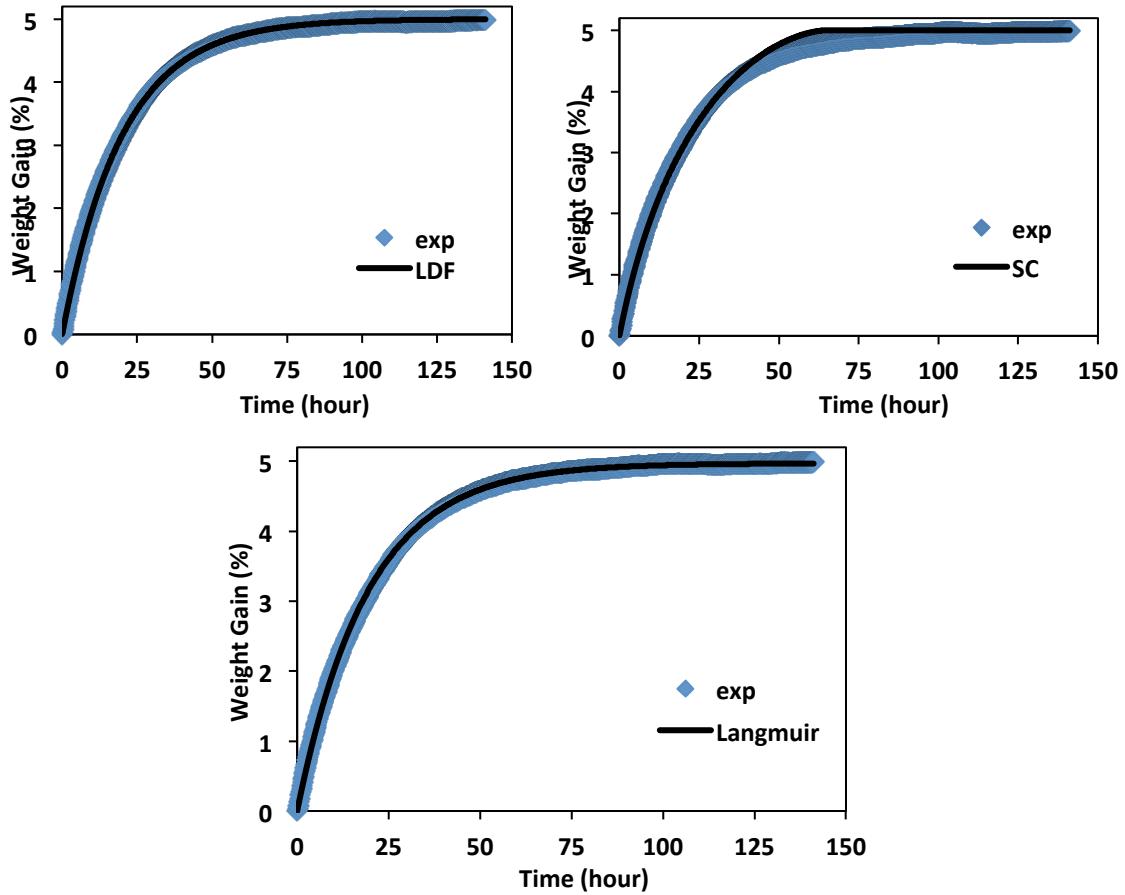
### 1.3.5.3 Comparison of kinetic models

Figure 12 shows an example of curve-fitting of water uptake curves by the LDF model, the SC model and the Langmuir kinetic model, which suggests that all three models were able to fit the data very well. The curve-fitting error, average absolute relative deviation (AARD), is estimated by the following Eq. (9).

$$err(\%) = \sum_{i=1}^n \left| \frac{y_i^{\text{exp}} - y_i^{\text{mol}}}{y_i^{\text{exp}}} \right| \times 100 \quad (9)$$

where the subscript  $i$  indicates the  $i^{\text{th}}$  data point,  $n$  is the total data points, and the superscripts  $exp$  and  $mol$  indicate experimental data and model prediction, respectively. Table 4 shows that the average curve-fitting errors for all three models for all conditions were 3.0% or less, indicating very good curve-fitting.





**Figure 12.** Curve-fitting of a water uptake curve by the linear-driving-force model, the shrinking-core model and the Langmuir kinetic model. Adsorption temperature: 60 °C; dew point: -44.1 °C.

**Table 4.** Average AARD of curve fittings.

Ads. Temp. (°C)	LDF (%)	SC (%)	Langmuir (%)
25	3.0	2.0	2.8
40	2.8	1.6	2.3
60	1.9	2.0	1.6
80	1.3	1.8	1.1

### The linear-driving-force model

Water uptake curves were fitted by the LDF model, and  $k_{LDF}$  values were determined. The overall mass transfer resistances ( $1/k_{LDF}$ ) were then determined in the order of magnitude of  $10^{-1}$  to  $10^2$  h. According to Eq. (4), the overall mass transfer resistance is a combination of the external film resistance, the macropore resistance and the micropore resistance. The micropore diffusivity ( $D_c$ ) in zeolite is usually in the order of  $10^{-8}$  cm<sup>2</sup>/s.<sup>12</sup> The corresponding micropore resistance is in the order of magnitude of  $10^{-4}$ - $10^{-5}$  h<sup>-1</sup>, which is much smaller than the overall mass transfer resistance, and thus can be neglected. Accordingly, Eq. (4) can be simplified to:

$$\frac{1}{k_{LDF}} = \frac{R_p}{3k_f} \frac{q_e \rho_p}{C_b} + \frac{R_p^2}{15\epsilon_p D_p} \frac{q_e \rho_p}{C_b} \quad (10)$$

The film mass transfer coefficient ( $k_f$ ) can be estimated by the Ranz and Marshall correlation:<sup>19</sup>

$$Sh = 2 + 0.6Sc^{1/3} Re^{0.5} \quad (11)$$

where  $Sh$ ,  $Sc$  and  $Re$  are the dimensionless Sherwood number, Schmidt number and Reynolds number. It should be pointed out that Eq. (11) is for mass transfer to unobstructed spheres and the presence of a support screen may affect the  $k_f$  value. However, this issue is beyond the scope of this discussion.

The water molecular diffusivity required for this calculation can be estimated by the Fuller et al. correlation.<sup>20</sup>

$$D_{AB} = \frac{0.00143T^{1.75}}{PM_{AB}^{1/2} \left[ \left( \sum \nu \right)_A^{1/3} + \left( \sum \nu \right)_B^{1/3} \right]^2} \quad (12)$$

Here the subscripts “A” and “B” indicate water and air, respectively,  $P$  is the pressure in bar,  $M_{AB}$  is the average molecular weight defined by  $M_{AB} = \frac{2}{1/M_A + 1/M_B}$ , and  $\nu$  is the atomic diffusion

volume. For the current system,  $P=1$  bar,  $M_{AB} = 22.21$  g/mol,  $(\sum \nu)_A = 13.1$  and  $(\sum \nu)_B = 19.7$

.<sup>21</sup> Density and viscosity of air needed for estimating the external mass transfer coefficient were estimated by REFPROP<sup>22</sup> and are given in **Table 5**. Also given in **Table 5** are calculated water molecular diffusivity, the external mass transfer coefficient and the macropore diffusivity. Results indicate that both molecular diffusivity and the external mass transfer coefficient increased as temperature increased. The macropore diffusivity of water in molecular sieve 3A generally decreased as temperature increased except from 40 to 60 °C where the macropore diffusivity slightly increased, which could be explained by experimental uncertainties.

**Table 5. Properties and model parameters for the LDF Model (P= 0.1 MPa).**

T (°C)	Density <sup>24</sup> (kg/m <sup>3</sup> )	Viscosity <sup>24</sup> (10 <sup>-6</sup> m <sup>2</sup> /s)	$D_{AB}$ (cm <sup>2</sup> /s)	$k_f$ (m/s)	$D_p$ (cm <sup>2</sup> /s)
25	1.1688	18.448	0.254	0.0318	0.295
40	1.1127	19.165	0.276	0.0342	0.140
60	1.0458	20.099	0.308	0.0375	0.158
80	0.9865	21.009	0.341	0.0409	0.124

When  $k_f$  and  $D_p$  are determined,  $k_{LDF}$  can be calculated by Eq. (10). Consequently, the water uptake curves can be predicted by Eq (3) using the calculated  $k_{LDF}$  values. **Figure 13** shows that using the predicted  $k_{LDF}$ , the average errors are below 9 %, somewhat higher than those obtained with the curve-fitted  $k_{LDF}$ . This result suggests that the LDF model is capable of predicting water adsorption kinetics.

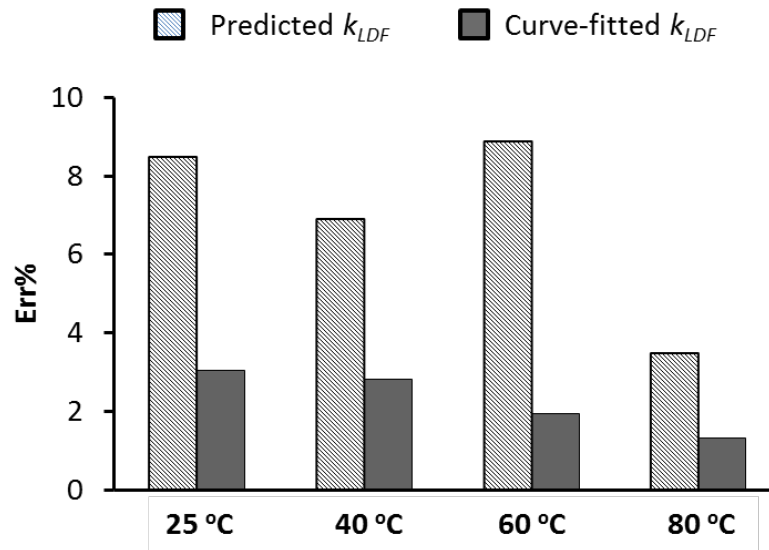


**Figure 13.** Average curve-fitting errors of the LDF model using predicted and curve-fitted  $k_{LDF}$  values.

Finally, both the external film resistance and the macropore resistance present in Eq. (10) can be estimated. **Figure 14** indicates that the film resistance contributes 25-50% of the overall mass transfer resistance during the course of water adsorption on zeolite 3A and the percentage of contribution generally decreased as adsorption temperature increased. Therefore, it can be concluded that water adsorption on zeolite 3A under current experimental conditions was controlled by both external film resistance and macropore resistance.

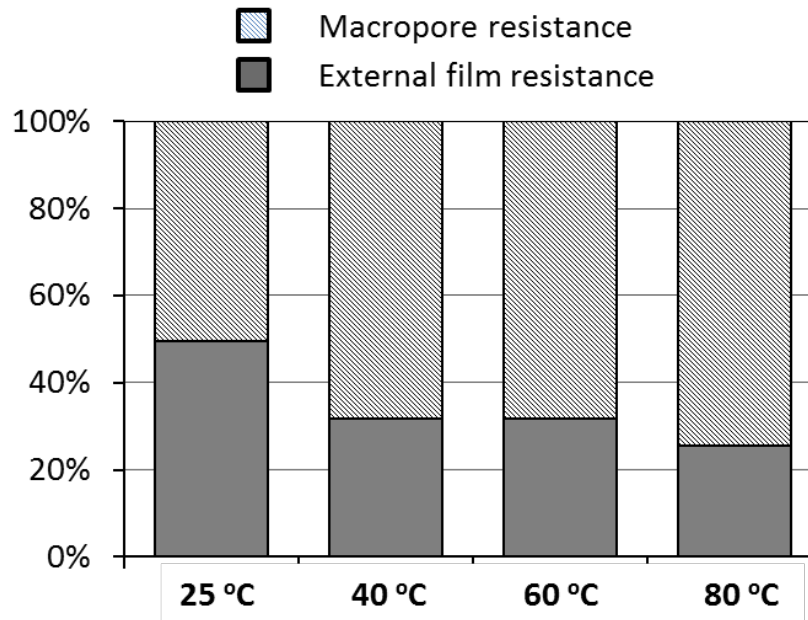


**Figure 14.** Distribution of mass transfer resistances.

It should be pointed out that the above analysis is done assuming isothermal adsorption, i.e. the water uptake is entirely controlled by mass transfer. The isothermal LDF model is a special case of the general non-isothermal LDF model,<sup>23</sup> which accounts for both heat and mass transfer resistances. As shown previously,<sup>23</sup> for isothermal adsorption, the solution of the general non-isothermal LDF equation reduces to Eq. (3) and a plot of  $\ln\left(\frac{q_e - \bar{q}}{q_e}\right)$  against  $t$  is

linear with slope  $-k_{LDF}$  and intercept 0 at  $t = 0$ . Indeed, the  $\ln\left(\frac{q_e - \bar{q}}{q_e}\right) \sim t$  plots of water uptake

curves obtained showed very good linearity. Also, water adsorption occurred very slowly under current experimental conditions and took hours to hundreds of hours to reach equilibrium, indicating that the adsorbate uptake is actually controlled by mass transfer rather than external heat transfer or both. In addition, **Figure 12**, as an example, shows nearly perfect curve-fitting of experimental water uptake data by the isothermal LDF model. Therefore, isothermal adsorption is a valid assumption for current experimental conditions. For very rapid adsorption where adsorbate uptake may be controlled by both heat and mass transfer, the non-isothermal LDF model<sup>25</sup> should be applied to determine kinetic parameters for both the heat- and mass-transfer equations.

### The shrinking-core model

As shown in **Table 4**, the average curve-fitting error ranged between 1.6% to 2.0% for adsorption temperatures from 25 to 80 °C with an average value somewhat lower than that of the LDF model (1.85% vs 2.25%). This result suggests that the SC model has a very good capability of describing the kinetics of water adsorption on molecular sieve 3A and it worked slightly better than the LDF model for the current application. Plots of  $\tau_1$  and  $\tau_1 + \tau_2$  versus water vapor pressure in the log-log scale shown in **Figure 15** indicate that adsorption time (time to reach adsorption equilibrium) increased significantly as water vapor pressure is reduced.

According to Eqs (6) and (7),  $k_f$  and  $D_p$  can be obtained from the slopes of the linear plots of  $\tau_1$  vs  $\frac{q_e \rho_p}{C_b}$  and  $\tau_2$  vs  $\frac{q_e \rho_p}{C_b}$ , respectively. **Figure 16** illustrates a comparison of  $k_f$  and  $D_p$

obtained for the LDF and SC models. The  $k_f$  value obtained with the SC model decreased significantly when the adsorption temperature increased from 25 °C to 40 °C, and it remained nearly constant when the temperature further increased up to 80 °C. At 25 °C, the  $k_f$  value was nearly double that obtained for the LDF model by the Ranz and Marshall empirical correlation, while at 40-80 °C, the  $k_f$  values for both models agreed very well. The  $D_p$  values obtained with the SC model were comparable with but smaller than those obtained with the LDF model. Also, it was found that considering experimental uncertainties,  $D_p$  generally decreases as temperature increases. The above analysis further confirms that water adsorption on molecular sieve 3A under current experimental conditions was controlled by both external film resistance and macropore resistance.

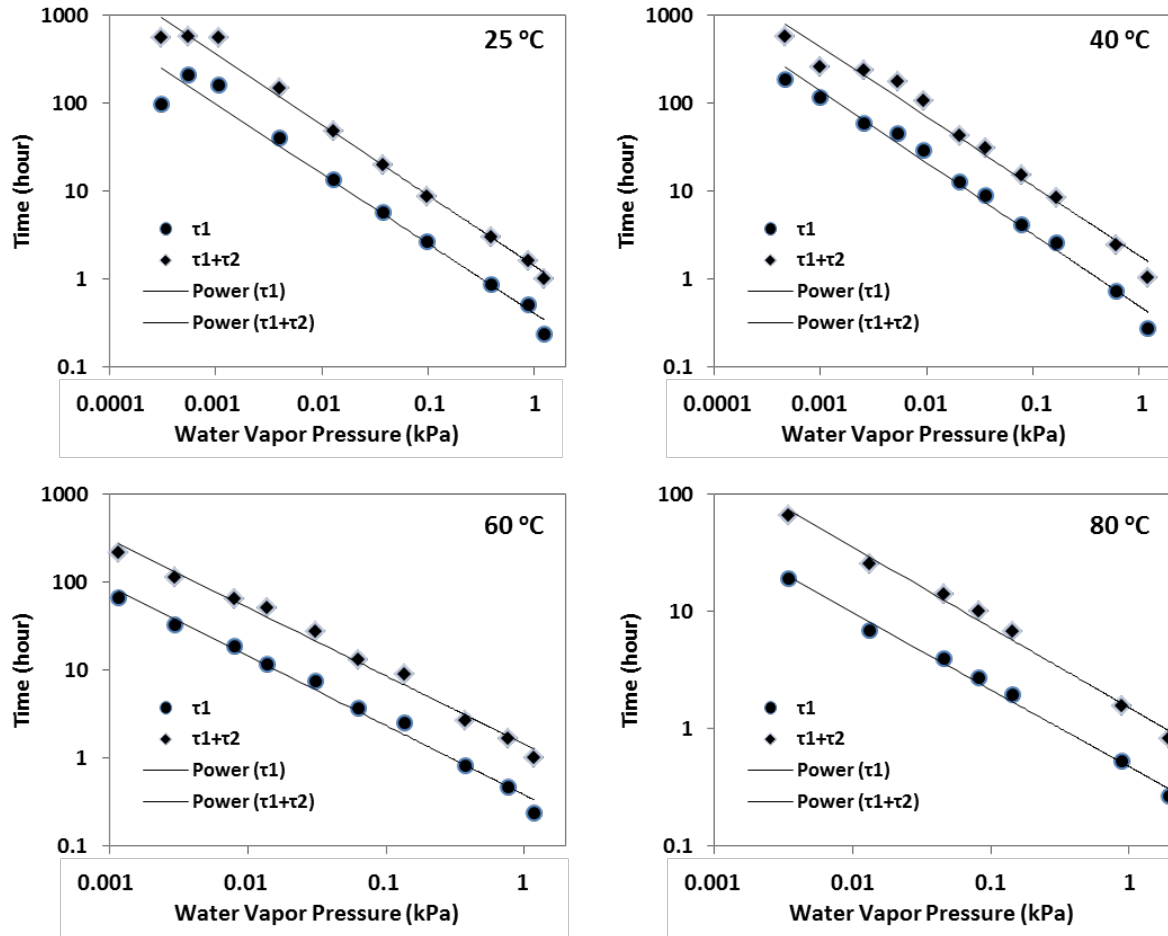


Figure 15. Plots of adsorption time versus water vapor pressure.

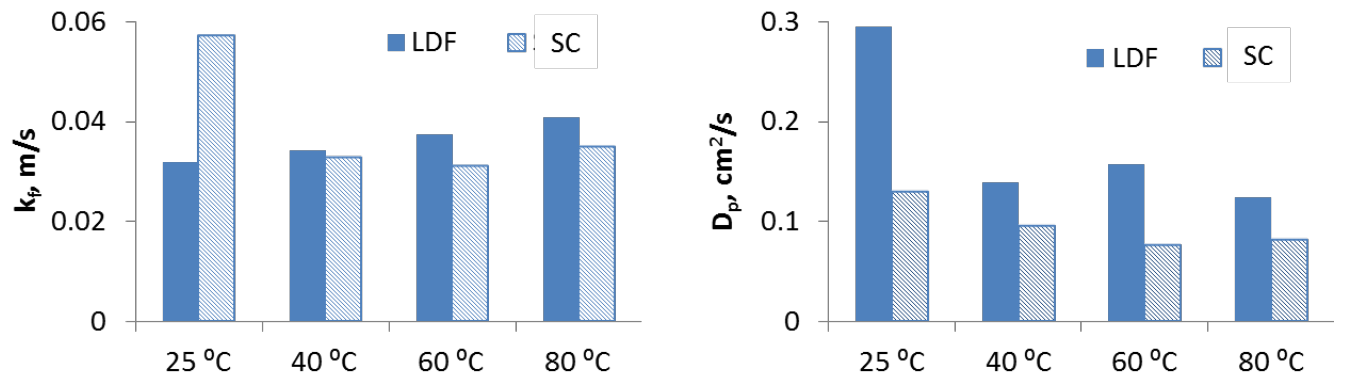


Figure 16. Comparison of external mass transfer coefficient and macropore diffusion coefficient obtained for the LDF and SC models.

### The Langmuir kinetic model

From the linear plots of  $\frac{d\bar{q}}{dt}$  vs  $\bar{q}$ , kinetic parameters,  $k_a$  and  $k_d$ , were determined. The curve-fitting errors of less than 3.0% (**Table 4**) indicate that the Langmuir kinetic model fit individual experimental water uptake curves very well.

Let  $\theta = q_e/q_m$  and  $\alpha = k_a/k_d$ , at equilibrium, when  $\frac{d\bar{q}}{dt} = 0$ , Eq (8) becomes the well-known Langmuir adsorption isotherm:

$$\theta = \frac{\alpha C_b}{1 + \alpha C_b} \quad (13)$$

Here,  $\theta$  is the fractional coverage of the surface, and  $\alpha$  is the Langmuir adsorption constant. **Figure 17** shows that the constant  $\alpha$  decreased with an increase in adsorption temperature and with an increase in water vapor pressure. This result can be explained by the Langmuir adsorption theory.<sup>19,24</sup> According to the Langmuir adsorption theory, the constant  $\alpha$  can be expressed by:<sup>24</sup>

$$\alpha = \beta (2\pi MRT)^{-1/2} \exp(Q/RT) \quad (14)$$

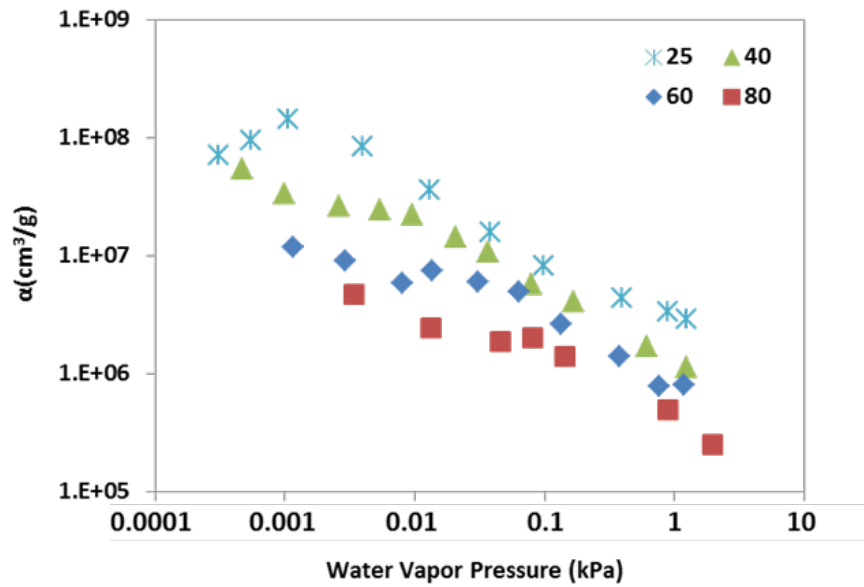


**Figure 17. Effects of adsorption temperature and water vapor pressure on the Langmuir adsorption constant.**

Here,  $\beta$  is a constant,  $M$  is the molecular weight,  $Q$  is the heat of adsorption, and  $R$  is the ideal gas constant. Since adsorption is an exothermic process and thus the heat of adsorption is positive,<sup>24</sup> the constant  $\alpha$  decreases with an increase in temperature, according to Eq. (14). Furthermore, previous studies showed that heats of adsorption of water vapor on zeolites generally decreased with an increase in the quantity adsorbed.<sup>25,26</sup> That is to say, as water vapor pressure increases, the quantity of water adsorbed on molecular sieve 3A increases and the heat of adsorption decreases, and therefore the adsorption constant  $\alpha$  decreases. This result implicitly verifies that the Langmuir isotherm model is unable to represent isotherms of water adsorption

on molecular sieve 3A if  $\alpha$  remains constant over the entire water vapor pressure range, which is in agreement with a previous study.<sup>27</sup> This result also indicates that there may exist a significant surface heterogeneity. Therefore, adsorption isotherm equations which take into consideration the surface heterogeneity effects should be used for modeling isotherms for water adsorption on molecular sieve 3A.

In summary, it was found from the curve-fitting with the linear-driving-force model and the shrinking-core model that water adsorption on molecular sieve 3A under current experimental conditions was controlled by both external film resistance and macropore resistance. The external film resistance contributed 25-50% of the total mass transfer resistance depending on adsorption temperature. Results from curve-fitting with the Langmuir kinetic model showed that the Langmuir adsorption constant decreased with an increase in adsorption temperature and with an increase in water vapor pressure, which can be explained by the Langmuir adsorption theory. This result suggests that there may exist a significant surface heterogeneity and implicitly verifies that the Langmuir isotherm model is unable to describe isotherms of water adsorption on MS 3A if  $\alpha$  remains constant over the entire water vapor pressure range.

### 1.3.6 Adsorption cycle test

A water adsorption/desorption cycle test was performed to obtain meaningful data to determine the regenerability of MS 3A and for model verification. The experimental condition for the cycle test is summarized in **Table 6**. The adsorption took place at 25 °C at the dew point of -7 °C. After the sorbents were saturated with water, the system was purged with dry air at 1L/min for 24 hr. The cycle test was continued for ten cycles. **Figure 18** shows that the water uptake reached nearly the same end points for both adsorption ( $18.61 \pm 0.05$  %) and desorption ( $12.50 \pm 0.07$  %). **Figure 19** shows the excellent overlapping of the water uptake curves for both adsorption and desorption cycles except the first adsorption cycle. This result demonstrates the excellent stability and reproducibility of the experimental system. Of note, the measured kinetics of adsorption were significantly faster than for desorption; this is addressed in section 2.6.2.

**Table 6. Experimental condition for the water adsorption cycle test.**

Sorbents	UOP type zeolite 3A, 8 mesh
Adsorption	Temperature: 25 °C Dew point: -7 °C Flow rate: 0.154 L/min
Desorption	Temperature: 25 °C Dry air flow rate: 1L/min Duration: 24 hr

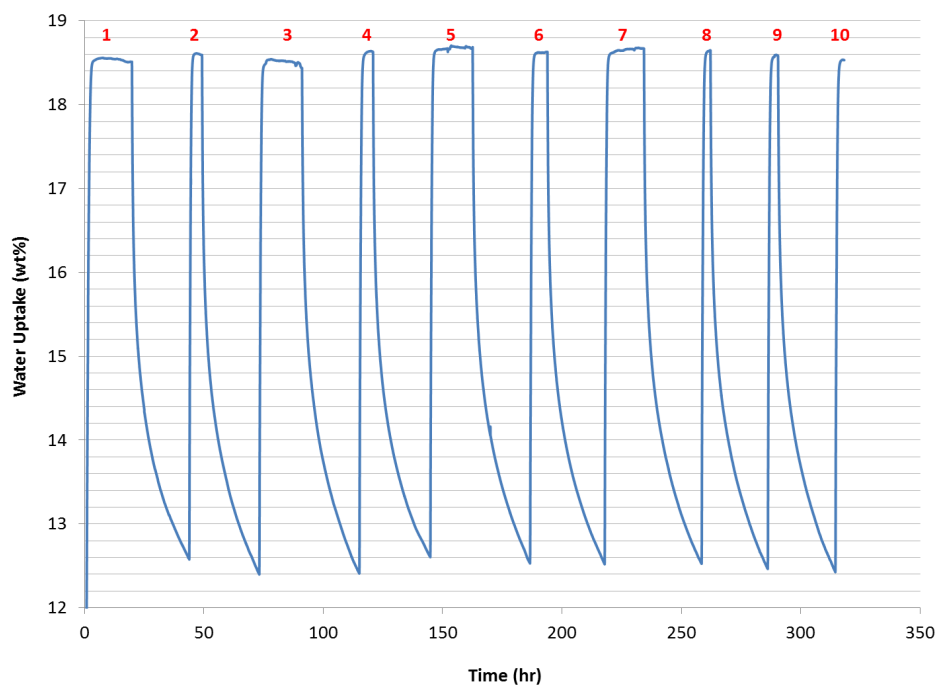


**Figure 18. Adsorption cycle test shows excellent regenerability of MS 3A.**

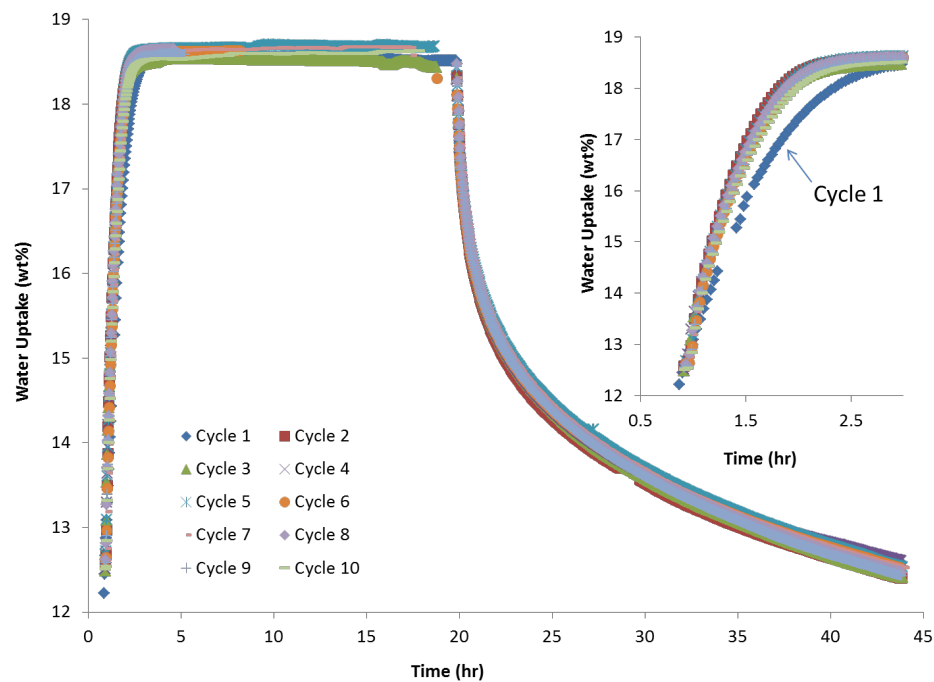


**Figure 19. Overlapping of water uptake curves.**



### 1.3.7 Water adsorption-desorption column tests

Deep bed tests were performed to obtain adsorption-desorption data of water on MS 3A using a column to validate the OSPREY model. The tests were performed in a 9 cm column by 1.75 cm diameter at 40 °C at gas flow rate of 2 L/min at two inlet dew point conditions of 19 °C and -60 °C. The experimental results for the inlet dew point of 19 °C for adsorption and -60 °C for desorption is shown in Fig. 20. These results are useful for validation of bed models (see section 2.7).

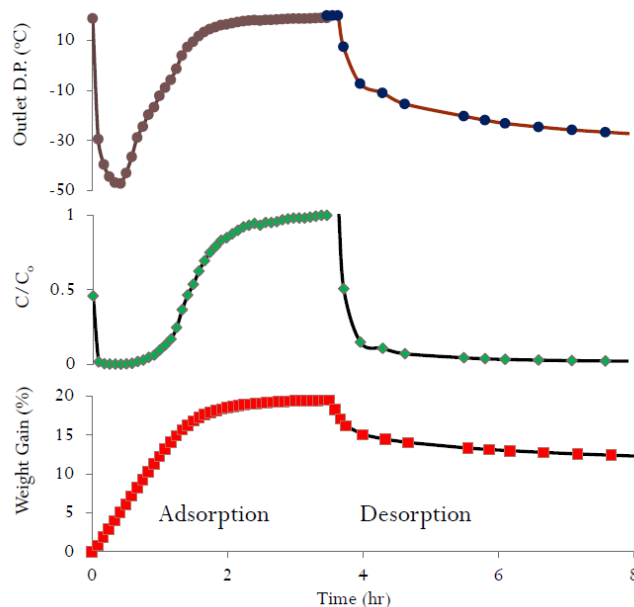


**Figure 20. Adsorption-desorption column studies in MS 3A column**

### 1.3.8 Water adsorption on AgZ

Data for water adsorption on AgZ were also obtained for the modeling of water/iodine co-adsorption on AgZ. The AgZ used in this test were received from ORNL (Ionex-type Ag 900 E16, lot #: 0911314-1). Preliminary tests of water adsorption on AgZ were performed at 40 and 60 °C with water dew points varying from -51.1 to 11.1 °C. **Figure 21** shows the isotherm obtained in this test. The water uptake capacity of AgZ increases with the water vapor pressure but decreases with adsorption temperature. Data will be utilized in the development of multicomponent isotherms (see section 2.5.3).

The AgZ used in this experiment was unreduced AgZ, because the experimental system for hydrogen reduction was under construction at that time. Future work will focus on the study of hydrogen-reduced AgZ which has higher adsorption capacity than the unreduced sorbent and is of interest to DOE.

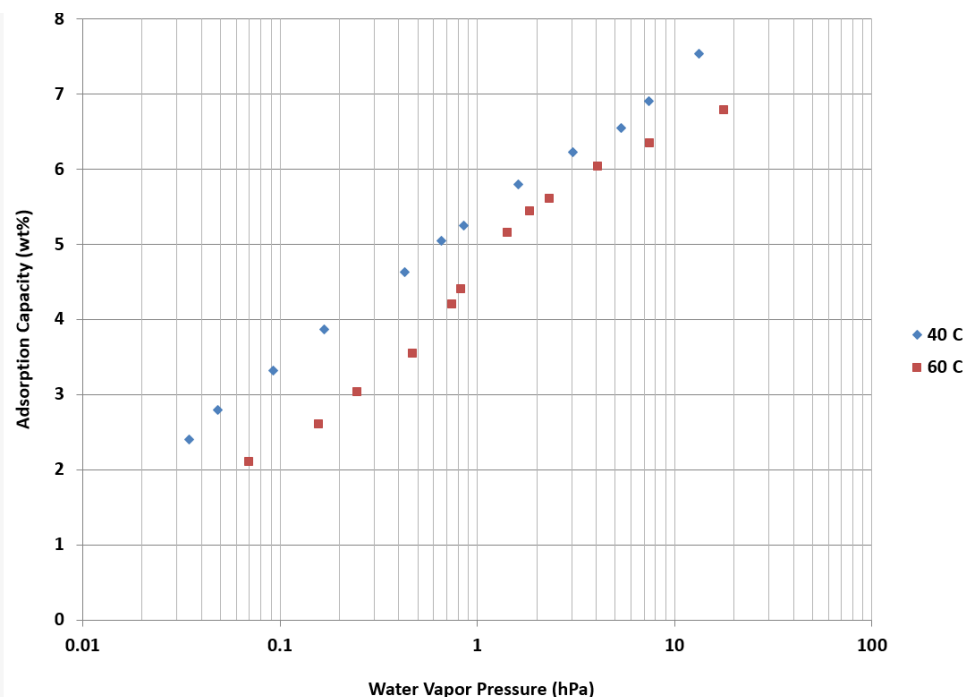


**Figure 21. Adsorption isotherm for water adsorption on AgZ at 40 and 60°C.**

## 1.4 Iodine adsorption on solid sorbents

### 1.4.1 Introduction

Having a very long half-life of  $15.7 \times 10^6$  years, iodine-129 is one of the major concerns in used fuel reprocessing off-gas treatment. Extensive work has been conducted related to removal of iodine from spent fuel reprocessing off-gases using a variety of solid sorbents including activated carbon, macroreticular resins, silver impregnated alumina, silver impregnated silica gel, silver exchanged faujasite and silver exchanged mordenite.<sup>22-29</sup> New sorbents, including nano composite materials,<sup>26</sup> functionalized silica aero-gels and chalco-gels,<sup>27, 28</sup> and metal oxide frameworks (MOFs),<sup>29</sup> are currently being developed and tested and preliminary results show very high iodine adsorption capacities. Despite the quality research in this field over the past four decades, the state-of-the-art of iodine removal is silver-exchanged mordenite due to its regenerability, high resistance to NO<sub>x</sub>, high decontamination factors ( $10^2$  -  $10^5$ ), and moderate sorption capacity ( $\sim 170$  mg I<sub>2</sub>/g sorbent).

In this work, preliminary studies of adsorption of iodine on MS 3A and silver exchanged mordenite (AgZ) were initiated to gather experimental adsorption equilibrium and kinetics data to support the development of modeling tools for radioactive off-gas capture from spent nuclear fuel reprocessing plants. Studies were first performed on iodine adsorption and iodine/water co-adsorption on MS 3A, since the experiment and modeling of the adsorption of water on MS 3A was completed. The experiments for iodine adsorption on AgZ are to be conducted on the current project.

Uptake curves and isotherms of iodine adsorption on MS 3A (water pre-saturated) were obtained with the continuous flow adsorption system. Batch experiments of iodine adsorption on MS 3A were also conducted to study the iodine adsorption on the sorbent at high iodine vapor pressure level.

### 1.4.2 Experiments setup

**Figure 22** shows a schematic diagram of the continuous-flow iodine adsorption experimental system, and **Figure 23** shows a photograph of the overall setup. The major systems of the adsorption unit are generation system and adsorption system. A dynacalibrator was used for generating the iodine and water vapor, and a microbalance system, which is similar to the system in the water adsorption unit in **Figure 3**, was used to measure the weight change of the sorbents during the adsorption process. A photograph of the generation system is shown in **Figure 24**.

The Dynacalibrator used in the adsorption unit was produced by VICI Metronics, Model 500. There are two chambers in the dynacalibrator, one for generating iodine vapor, the other one for water vapor. The rate of generation depends on the temperature of the dynacalibrator chamber where the diffusion tube is located. The theoretical rates of iodine vapor generation at 50-110 °C is provided by the supplier for the specific diffusion tube used in this work. Calibration of iodine gas concentration by the ICP-MS method in our laboratory was conducted to insure the accuracy, and iodine vapor generation rate for 30 and 40 °C were obtained by extrapolation.

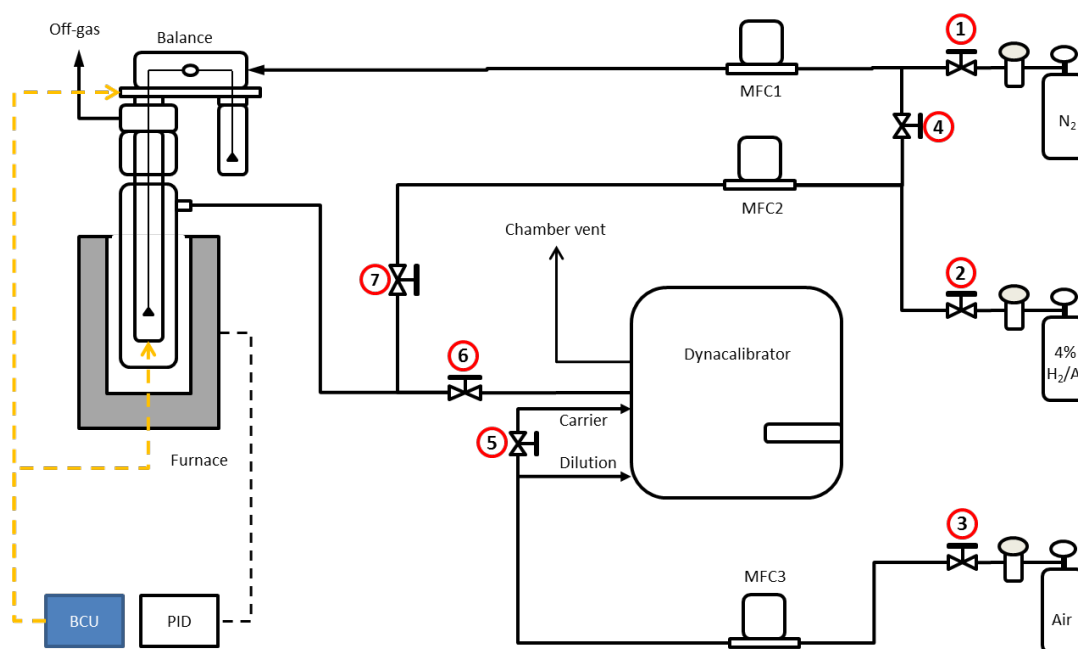


**Figure 22. Schematic diagram of the experimental setup for iodine adsorption.**

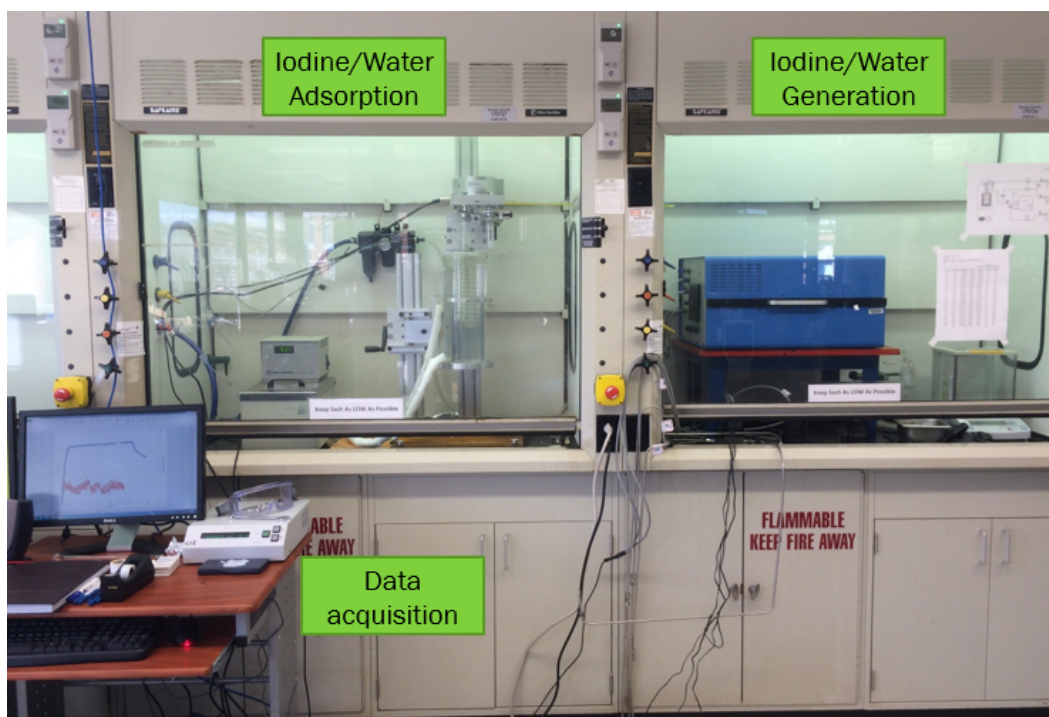


Figure 23. Iodine adsorption experimental setup.

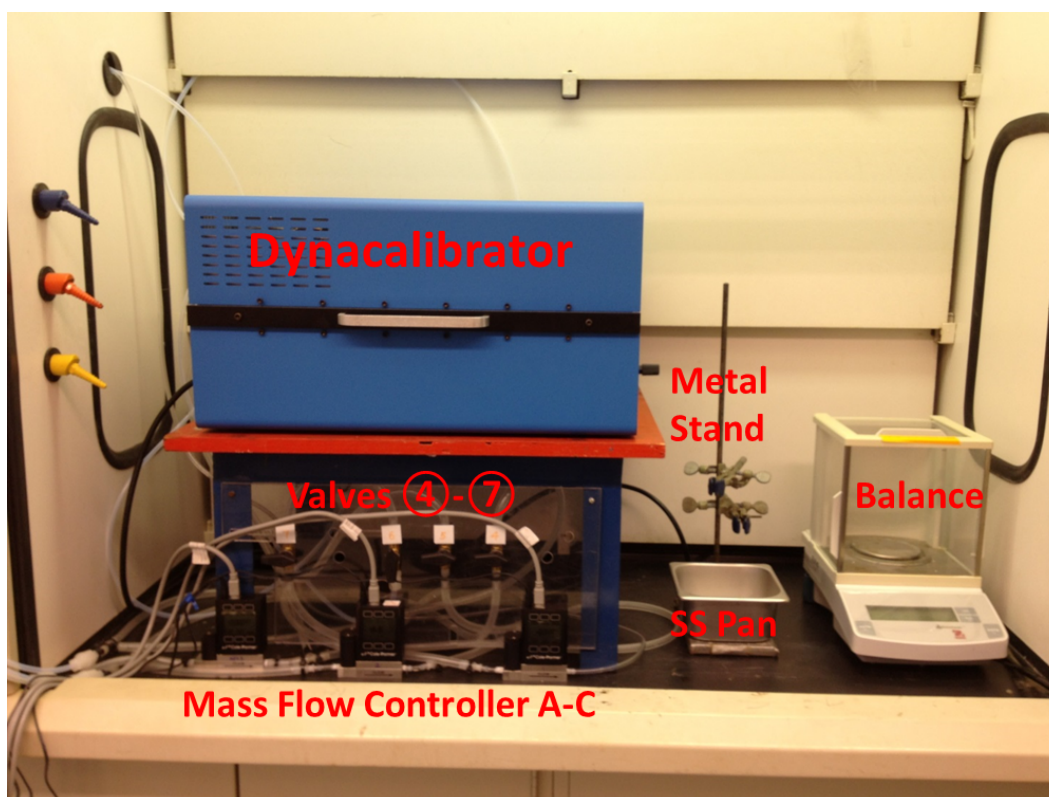


Figure 24. Dynacalibrator and iodine generation system.

### 1.4.3 Iodine adsorption on MS 3A - continuous flow experiment

Several continuous flow experiments of iodine adsorption on MS 3A (UOP type zeolite 3A, 8 mesh) were conducted at different dew points and iodine concentrations in the air flow. The MS 3A beads were first equilibrated with in the gas flow before iodine was introduced. This process takes about 200-500 hours, depended on the water dew point of the gas flow. After the sorbent was saturated and reached equilibrium, iodine vapor was added with a concentration range of 0.3 - 40 ppm (by volume).

Adsorption experiments of iodine on MS 3A in dry air were first conducted. The dew point of the dry air from the cylinder ranges from -70 to -65 °C, varying by cylinders. The MS 3A sorbent were first pre-equilibrated in the dry air for about 500 hours, at the temperature of 25°C, before iodine was introduced. The concentration of iodine was increased gradually from 1 ppm to 10 ppm. One of the uptake curves is shown in **Figure 25**. As shown on the plot, an increase of the weight gain of the sorbent was observed when a 1 ppm iodine gas flow was introduced, but further increase in the iodine concentration up to 10 ppm did not result in additional weight gain. Instead, a decrease was observed when the iodine concentration increased from 5.4 ppm to 10 ppm, and an increase was found when iodine was stopped at 1060 hours.

The abnormal behavior of the uptake was found to correlate with the change of ambient dew point. The strong influence was due to the permeation of the water in the ambient air into the Teflon tubing used in the adsorption unit. In addition, the plot also shows that the weight gain changed largely when changing the air cylinders during the experiment, at such low dew point level, because of the variation of the dew point of air in the cylinders. Despite effects of the ambient dew point and the air cylinders, a conclusion can be made from the experiments that the maximum capacity of iodine adsorption on MS 3A, at iodine concentration level up to 10 ppm, is not greater than 1%.

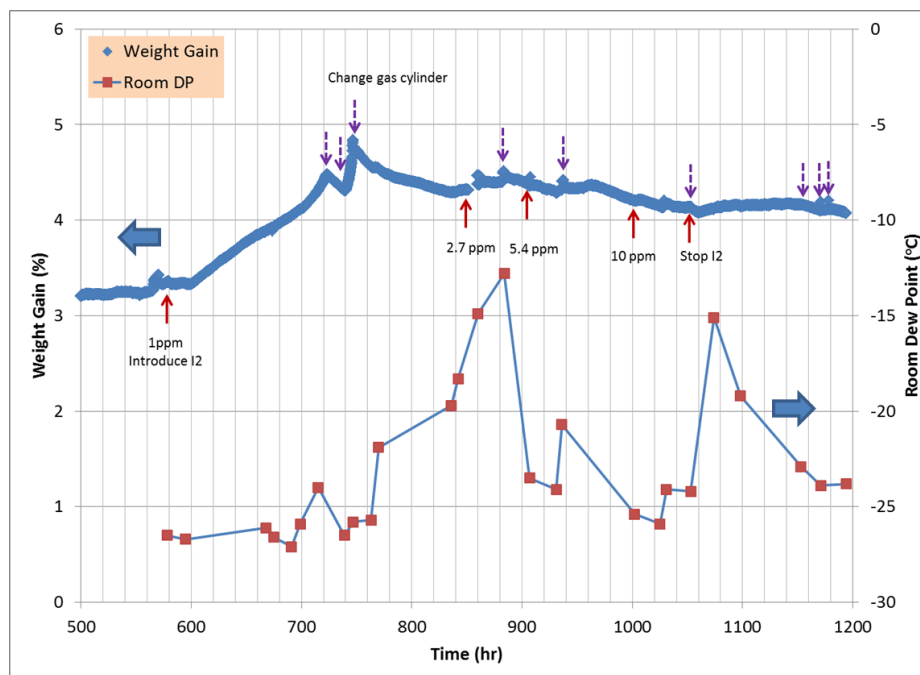


**Figure 25. Iodine loading on MS 3A pre-saturated by dry air (dew point -70 to -65 °C) at 25 °C. Gas flow rate: 0.5 L/min.**

Experiments were also done with MS 3A pre-saturated with water at dew point about  $-40^{\circ}\text{C}$ , over an adsorption temperature of  $30^{\circ}\text{C}$ , and the corresponding weigh gain due to water adsorption was 14.6 wt%. **Figure 26** shows the uptake curve. After 150 hours when the sorbent is saturated, iodine at 5.4 ppm level was then introduced into the adsorption system. The iodine gas concentration was increased gradually up to 36.8 ppm. The final weight gain was stabilized at about 15.2 wt %. The fluctuation in the curve is due to the change of ambient dew point. The red line on the plot demonstrates the trend of the uptake and the green line shows the room temperature which correlates to the change of the ambient dew point.

**Figure 27** shows the uptake of the iodine on the pre-saturated MS 3A at dew point  $-40^{\circ}\text{C}$ . The uptake increases with the increases of the iodine concentration in the air stream, and the weight gain due to iodine loading is less than 1 wt% at iodine concentration up to about 37 ppm. This figure indicates the capability of the apparatus and approach to collect data on adsorption of gases at low loadings in the presence of moisture.

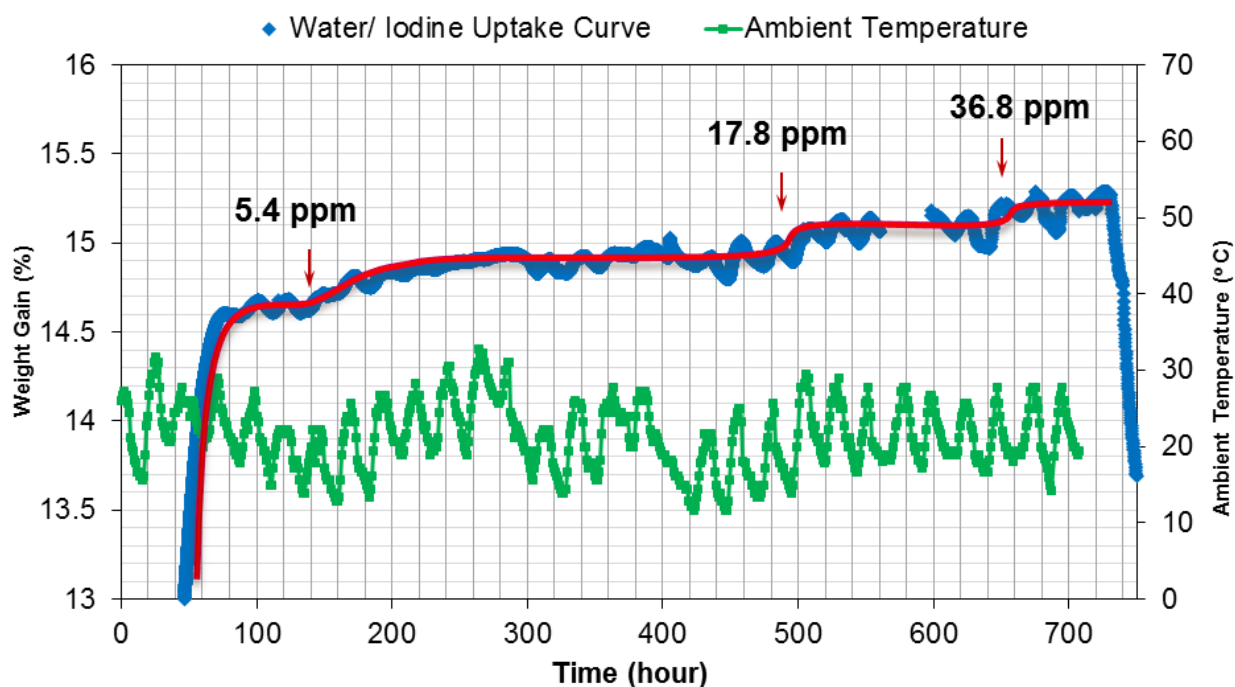


**Figure 26. Uptake curve for water/iodine adsorption on MS 3A at  $30^{\circ}\text{C}$ . The red line on the plot demonstrates the trend of the uptake and the green line shows the room temperature which correlates to the change of the ambient dew point.**

In order to eliminate the strong influence of the ambient air humidity on the equilibrium data, the tubing of the adsorption unit was upgraded for future work. The dynacalibrator was sent back to the supplier to upgrade the Teflon tubing to stainless steel tubing, and remaining tubing in the lab connecting feed gas cylinders to the dynacalibrator was also replaced with stainless steel tubing. The work was done at the end of FY 2014.



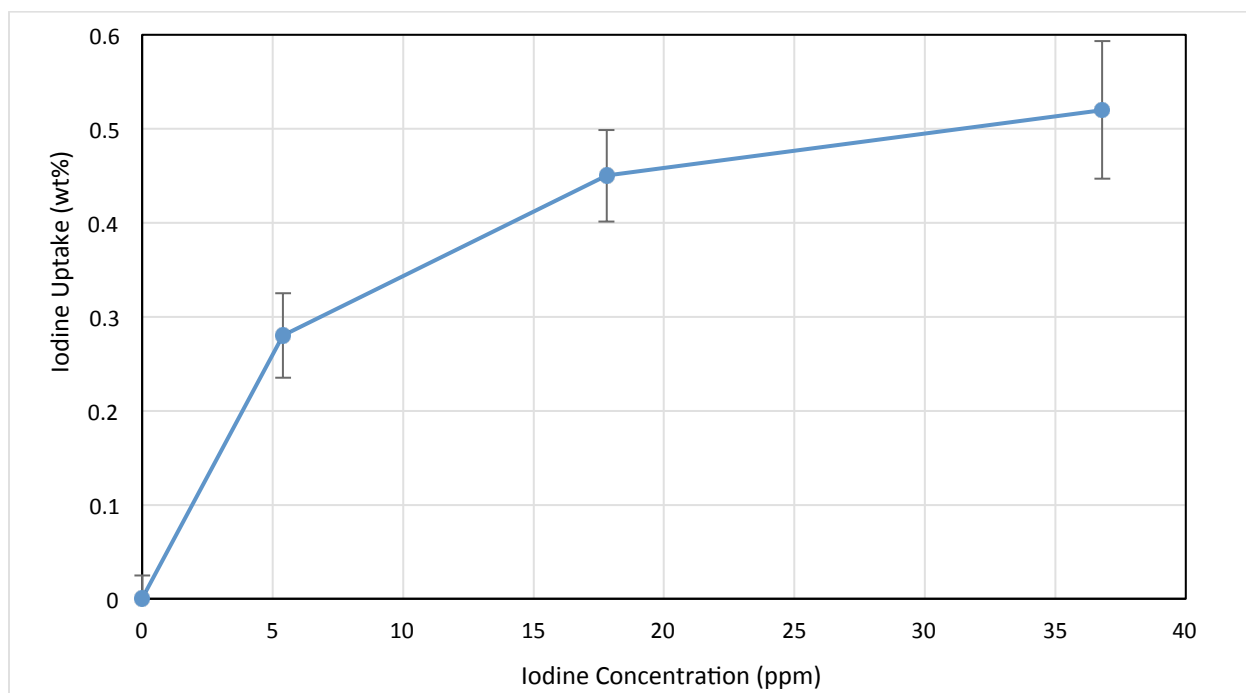


**Figure 27 Iodine adsorption on water pre-saturated MS 3A at 30 °C.**

## 1.5 Summary

Conclusions that can be drawn from this experimental work are:

- 1) Experimental systems have been established that enable the collection of microscopic kinetics and equilibria of single and multicomponent uptake of gaseous species on solid sorbents. The systems, which can operate for temperatures ranging from ambient to 250 °C and water dew points from -69 to 17°C, are useful for collecting data needed for modeling performance of new sorbents of interest to DOE.
- 2) GSTA model has the best prediction of water adsorption isotherms among the models studied, and there is a nearly perfect agreement between the experimental data and the model prediction.
- 3) Differences were found between the current experimental isotherms with UOP zeolite 3A sorbent and the literature isotherms with Grace Davison zeolite 3A sorbent. Experimental results indicate that binder material in sorbent beads does not absorb water and effects of  $\text{Na}^+$  and  $\text{K}^+$  composition in the sorbents on the water adsorption capacity of MS 3A cannot fully explain the differences between the isotherms. Sorbents characterization will be done in future work to determine the possible reasons.
- 4) Both LDF and SC models are capable of fitting the uptake curves, and the SC model performs slightly better. The adsorption kinetics is controlled by film resistance and macropore diffusion.
- 5) The result of adsorption cycle test of water adsorption and desorption on MS 3A particles suggested that MS 3A has excellent stability and regenerability.
- 6) MS 3A is found have an iodine uptake capacity of less than 1 wt%, at iodine concentration up to 37 ppm.

## **2. Modeling of adsorption processes for off-gas treatment**

### **2.1 Key personnel**

Sotira Yiacoumi (co-PI), Costas Tsouris (co-PI), Austin Ladshaw (Graduate Student), Georgia Institute of Technology (GIT)

### **2.2 Scope**

This project is focused on the development of modeling tools for off-gas capture from future nuclear-fuel recycling facilities. Target species include tritium, iodine, krypton, and carbon dioxide. The effort extends available models and algorithms developed for gas sorption, and the results can be used to provide recommendations on a path forward for the development of sorbents and sorption processes for off-gas treatment. Models will be developed for equilibria analyses, adsorption kinetics, and material transport in fixed-bed columns.

### **2.3 Modeling Approach**

Off-gas generated from reprocessing spent nuclear fuel contains a mixture of radioactive gases including I-129, Kr-85, H-3, and C-14. Over the past few decades, various separations processes have been developed for separating these gases. Adsorption data for gas mixtures of several species can be determined experimentally. However, as the number of species increases, the experiments required may become more complicated. Therefore, procedures capable of predicting the adsorption behavior of gas mixtures from individual isotherm data of pure components need to be developed. Calculation procedures involve solving simultaneously the differential equations for macroscopic and microscopic mass balance as a function of time and depth of the adsorption bed.

After determining the model parameters experimentally, one can set up the mass balance equations for the adsorbent bed. These equations involve interphase mass transfer, intraparticle diffusion, chemical reactions, and other mass transfer processes based on the structure of the adsorbent pellet and fixed-bed. A term to account for the aging of the adsorbent that has been observed experimentally could also be included in the model. In the case of chemical reactions, the local equilibrium assumption can be applied where appropriate. The model will include microscopic and macroscopic mass balances as a function of time and depth of the bed and the input data should include parameters such as the inlet gas composition, flow rate, temperature, bed depth, and adsorbent properties. Model output will include such basic information as outlet gas composition and pressure with time, the concentration profile in the column, and the temperature profile as a function of time.

Overall, the modeling venture is a collaborative effort between this project and Idaho National Laboratory (INL). Figure 30, with Table 7, below shows a schematic of the modeling library under development by GIT and INL referred to as the Fundamental Off-gas Collection of Kernels (FLOCK). Each kernel in the FLOCK can operate on its own or in conjunction with other kernels to make a more complete description of the chemistry and physics occurring during adsorption. Although many of these kernels are complete, there is still some coupling between kernels and further development required to complete the FLOCK.



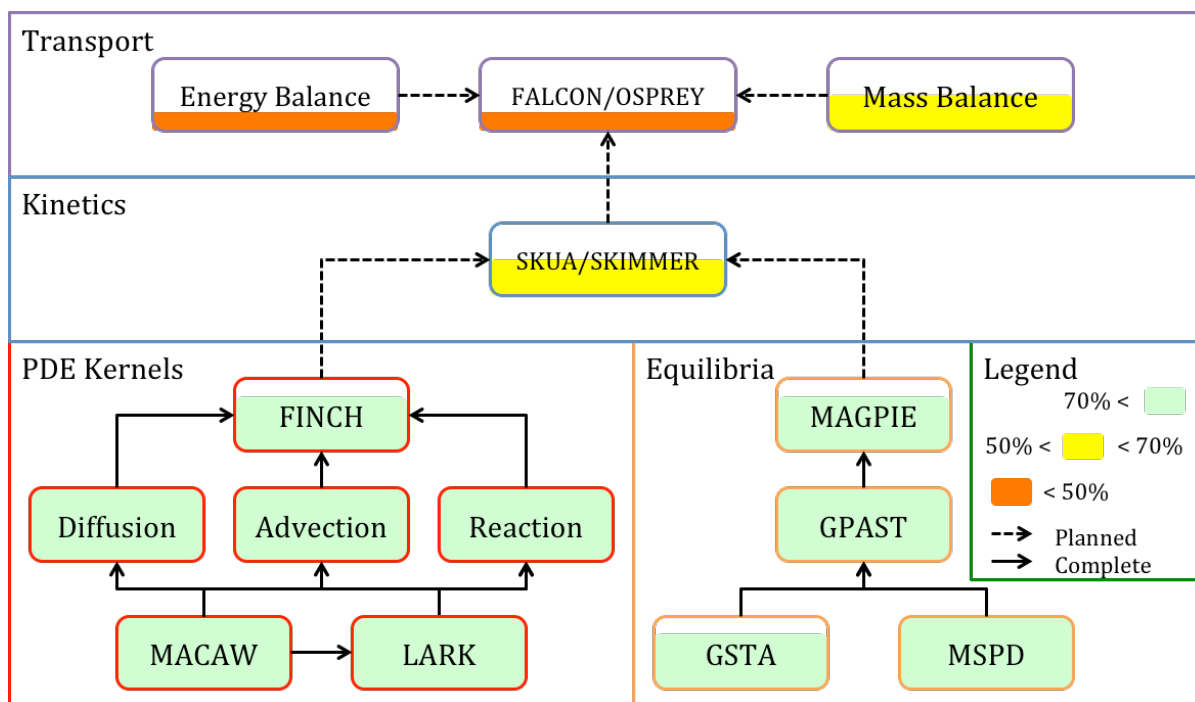


**Figure 28. Overview of modeling effort showing the state of development of each kernel and how they are connected.** Table 7 gives each acronym and a short description of the kernel.

**Table 7. Names and descriptions for all kernels in the FLOCK**

Acronym	Name	Description
MACAW	<u>M</u> atrix <u>C</u> alculation <u>W</u> orkshop	Basic C++ object to deal with real matrices
LARK	<u>L</u> inear <u>A</u> lgebra <u>R</u> esidual <u>K</u> ernels	Iterative solver library for linear and non-linear problems
FINCH	<u>F</u> lux-limiting <u>I</u> mplicit <u>N</u> on-oscillatory <u>C</u> onservative <u>H</u> igh-resolution scheme	Modeling framework for solving advection-diffusion-reaction problems in 1-D derived from conservation laws
GSTA	<u>G</u> eneralized <u>S</u> tatistical <u>T</u> hermodynamic <u>A</u> dsorption	Heterogeneous single-component isotherm model for gas-solid equilibria
MSPD	<u>M</u> odified <u>S</u> predding <u>P</u> ressure <u>D</u> ependent model	Surface activity model for predicting non-idealities of the adsorbed phase
GPAST	<u>G</u> eneralized <u>P</u> redictive <u>A</u> dsorbed <u>S</u> olution <u>T</u> heory	Purely predictive multi-component gas-solid adsorption equilibria from pure isotherms
MAGPIE	<u>M</u> ulti-component <u>A</u> dsorption: <u>G</u> eneralized <u>P</u> rocedure for <u>I</u> sothermal <u>E</u> quilibria	Culmination of GPAST with the MSPD activity model and GSTA isotherm model

SKIMMER	Sorption <u>K</u> inetic Model for <u>M</u> ass <u>transf</u> ER	Diffusion kinetic model for commercial adsorbent pellets involving pore and surface diffusion as well as external mass transfer
SKUA	Sorption <u>K</u> ernel for <u>U</u> ptake <u>r</u> Ates	Coupling of adsorption equilibria with diffusion kinetics and includes a variable surface diffusivity
OSPNEY*	Off-gas <u>S</u> eP <u>a</u> ration and <u>R</u> E <u>c</u> ove <u>r</u> Y	INL-developed mass transport model for adsorption in fixed beds
FALCON*	Fixed-bed Adsorption for <u>L</u> aws of <u>C</u> ON <u>s</u> ervation	GIT-developed mass transport model for adsorption in fixed beds

\*The difference between OSPNEY and FALCON is discussed in the modeling approach.

## 2.4 Partial Differential Equation Kernels

### 2.4.1. MACAW

When numerically solving partial differential equations (PDEs) we first need to discretize the continuous system into a series of sub-domains upon which we can base our solution methods to find solutions to unknown variables in space and time (Thomas, 1995). These discretizations convert the continuous problem into a discrete linear algebra problem that is solved using matrices. Therefore, we sought to develop a C++ object that could implicitly handle the data and operations associate with real matrices. MACAW provides that structure and interface that is used by the kernels above it and also includes some novel methods for directly solving linear systems.

### 2.4.2. LARK

As the systems of equations we seek to solve become more complex, or non-linear in nature, we need a more advanced and robust set of methods to solve those equations. Additionally, the systems of equations that are derived from PDEs are typically large, sparse systems of equations. Therefore, we also need a way of dealing with the sparsity of these systems efficiently. LARK provides us with a means to iteratively solve large, sparse linear and non-linear systems of equations, and is built on top of the matrix objects provided by MACAW.

The linear solvers developed in LARK are all members of a subset of methods known as Krylov subspace methods (Saad, 2003). These are some of the current state-of-the-art routines available for iteratively solving large, sparse systems. LARK currently contains four different Krylov solvers including implementations for: (i) Generalized Minimum Residuals (GMRES), (ii) Preconditioned Conjugate Gradients (PCG), (iii) Bi-Conjugate Gradients Stabilized (BiCGSTAB), and (iv) Conjugate Gradients Squared (CGS). The LARK user interfaces with these methods by providing a function that computes a matrix-vector product and may optionally provide a function to perform preconditioning.

Although the use of preconditioning is optional, the use of proper preconditioning can greatly enhance the efficiency of these methods (Saad, 2003). Figure 31 below shows the effect that preconditioning can have on the LARK routines. In each case, LARK was asked to solve 125 linear equations representing a standard Laplacian operator on a regular mesh in three-dimensions. Both PCG and GMRES methods gave essentially the same results for all test runs.

Additionally, when no preconditioning was used, both methods required roughly twice as many iterations to converge. These results demonstrate the validity of the methods implemented in LARK as well as the positive impact and efficiency gained by applying a preconditioner.

There are currently two supported non-linear solvers available in LARK: (i) a Picard method and (ii) a Preconditioned Jacobian-Free Newton-Krylov (PJFNK) method. The Picard method requires the user to provide a residual calculation for each non-linear equation and a relaxed solution estimate for each variable in the system. However, the PJFNK method only requires the user to provide a residual calculation. PJFNK then constructs a linear problem at each non-linear iteration, which is then solved by one of the Krylov methods mentioned above. As a consequence of this relationship between the linear and non-linear solvers, the user may also provide a preconditioner for the linear systems constructed by PJFNK (Knoll and Keyes, 2004).

In general, PJFNK is a more robust method than Picard for solving non-linear systems, but that robustness may come at the cost of a loss in efficiency due to an increase in complexity of the method. This effect is shown below in Figure 32, where solution methods are compared for solving a non-linear, time-dependent, 1-D PDE with three different techniques: (i) a Direct or Explicit method, (ii) a Picard iteration, and (iii) the PJFNK method. Since a 1-D PDE can be solved efficiently without using Krylov subspaces, these more advanced solution methods are actually slower to solve this type of problem due to the computational cost associated with their complexity. The Direct method is also less efficient in this case because it is forced to take very small time steps to maintain stability, whereas the stability of Picard and PJFNK are independent of the time step.

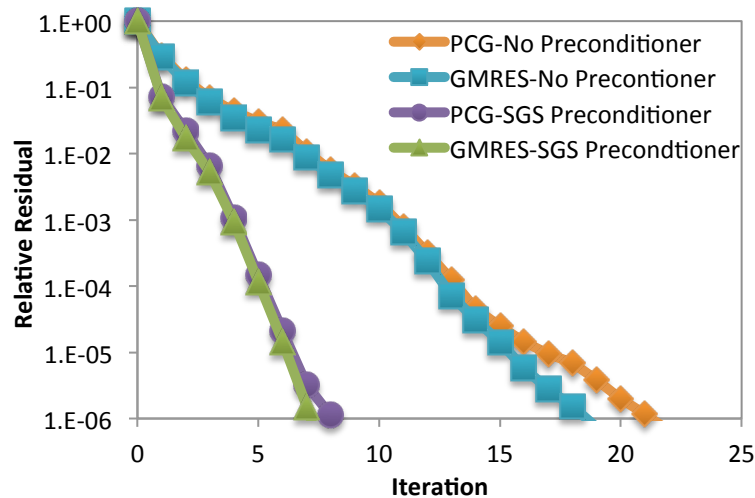


**Figure 29. Demonstration of the capabilities of LARK as well as the effect of good preconditioning for a linear system.** The preconditioner used in this example was a Symmetric Gauss-Seidel (SGS) preconditioner.

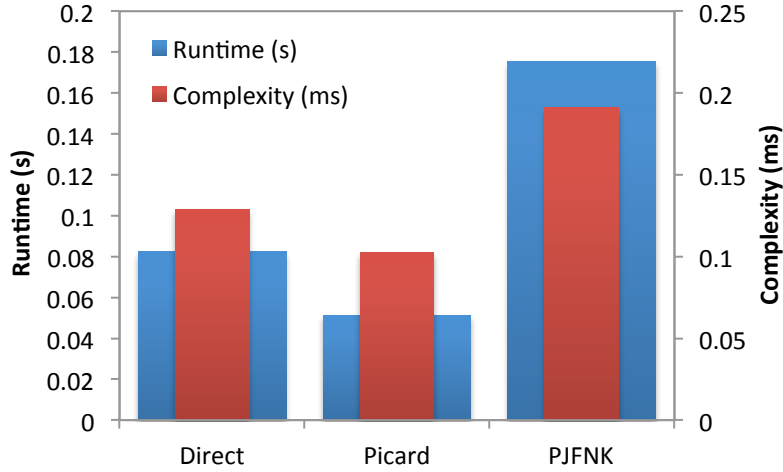


**Figure 30. Comparison of techniques to solve non-linear PDEs in one dimension.** The Picard method was most efficient since it combined the least amount of complexity with the fewest number of time steps. Complexity was measured as the average time needed to complete all iterations for all time steps taken.

### 2.4.3. FINCH

The primary idea behind FINCH is to provide a framework by which we can setup and solve generalized material balance equations. There are several terms that we wish to include in a general conservation law such as advection, diffusion, reaction, etc. Each of these terms needs to be flexible enough so that they can be allowed to vary in space and time. We also need to consider the types of domains over which we are looking to solve. Based on these considerations, we have formulated what we refer to as a Generalized 1-D Conservation Law Model shown below in Equation 1.

$$z^d R \frac{\partial u}{\partial t} + \frac{\partial}{\partial z} (z^d v u) = \frac{\partial}{\partial z} \left( z^d D \frac{\partial u}{\partial z} \right) - z^d k u - z^d S \quad (1)$$

In this form of the conservation law, our conserved quantity is denoted by the variable  $u$ . This can be any conserved quantity that we wish to observe and will depend on a number of space-time dependent parameters, which all have a different physical interpretation.  $R$  is a retardation coefficient,  $v$  is an advective velocity,  $D$  is for dispersion,  $k$  is a reaction coefficient and  $S$  can be some source/sink term or other forcing function.

The spatial quantity  $z$ , along with its exponent portion  $d$ , is used to change the geometry of the physical domain upon which we observe. We can show this by a simple inspection, if  $d=0$  in Equation 1, then the coordinate system is Cartesian. Likewise, if we specify  $d=2$ , then the form of the equation is now in spherical coordinates. Therefore, we can easily switch between Cartesian, polar, and spherical coordinates just by changing the value of a single argument from 0 to 1 to 2.

To numerically solve the PDE in Equation 1, we will use a conservative finite difference numerical technique called Monotonic Upstream-Centered Scheme for Conservation Laws (MUCSL) scheme. These discretization schemes were first introduced by Bram van Leer in 1979,

and have since been the leading approach for these types of problems. A particular MUCSL scheme of interest is the Kurganov and Tadmor (KT) scheme for its high accuracy and applicability for both linear and non-linear conservation laws (Kurganov and Tadmor, 2000).

The KT scheme uses the concept of *slope limiting*, or *flux limiting*, to reconstruct the edge fluxes at the boundaries of each cell in the discretized mesh (Figure 33 and Equation 2). By taking this approach, you can ensure that the quantity  $u$  is conserved across the entire domain, as overflow from one cell would then feed into the next cell. Additionally, to maintain a high resolution and accuracy, the KT scheme also includes a correction term for numerical dispersion, which seeks to *penalize* the discretization based on the local maximum wave speed (Equation 3). This allows the scheme to better handle shocks and discontinuities that may be present in the solution (Kurganov and Tadmor, 2000).

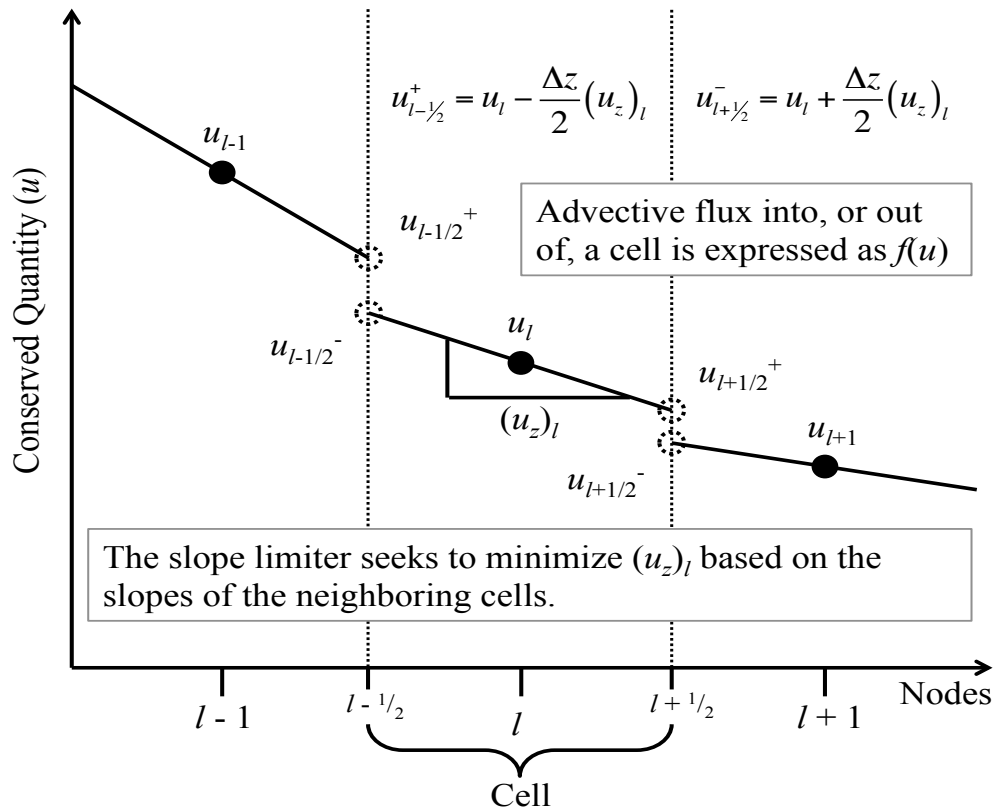


**Figure 31. Visualization of the process of flux reconstruction on a 1-D mesh.**

$$H_{l+1/2} = \frac{1}{2} \left[ f(u_{l+1/2}^+) + f(u_{l+1/2}^-) \right] \quad (2)$$

$$p_{l+1/2} = \frac{a_{l+1/2}}{2} \left[ u_{l+1/2}^+ - u_{l+1/2}^- \right] \quad (3)$$

In the above equations,  $H_{l+1/2}$  is the average advective flux leaving cell  $l$  from the right and  $p_{l+1/2}$  is the penalty term applied for the jump discontinuity at the right boundary of the cell. The magnitude of that penalty is based on the jump, as well as the local maximum wave speed

( $a_{l+1/2}$ ). Using the same procedure for the left side boundary of the cell, then applying a centered finite difference approximation to the advective term's derivative, will produce the overall advective flux discretization shown in Equation 4.

$$\frac{\partial}{\partial z} f(u)_i \equiv \frac{(H_{l+1/2} - p_{l+1/2}) - (H_{l-1/2} - p_{l-1/2})}{\Delta z} \quad (4)$$

According to Kurganov and Tadmor (2000), the maximum local wave speed is equivalent to the maximum spectral radius of the Jacobian of  $f(u)$  over all  $u$  within the discretized sub-domain (Equation 5). In general, this may be a very expensive term to estimate, especially if  $f(u)$  is complex. Therefore, we seek to provide within our discretization a simpler approach to approximating this local wave speed term.

$$a_{l+1/2} = \max_{u \in C(u_{l+1/2}^-, u_{l+1/2}^+)} \left\{ \rho \left( \frac{\partial f(u)}{\partial u} \right) \right\} \quad (5)$$

First, we will consider our particular conservation model from Equation 1. For our application, the advective term is always of the form  $f(u) = z^d v u$ . From this formulation, we can make a simple observation; if the parameter  $v$  is not a function of  $u$ , then the Jacobian of the function will be constant, with respect to  $u$ , and the maximum wave speed will always be of the form  $a = z^d v$ . This should work well for most of the problems we are interested in, but will it work for the non-linear case?

To explore this option, let us consider our parameter  $v$  to be any function that may or may not be a function of  $u$ . Therefore, for any given  $v$  or  $u$  in space-time, the entries of the Jacobian would be formed using the product rule of differentiation (Equation 6). Based on this analysis, it is immediately apparent that if  $v$  is not a function of  $u$ , then the maximum wave speed is exactly  $z^d v$ . However, if  $v$  is a function of  $u$ , then our approach to the penalty term ( $a$ ) is a truncated approximation of the real local wave speed.

$$\frac{\partial}{\partial u} f(u) = \frac{\partial}{\partial u} (z^d v u) = z^d v + z^d \frac{\partial v}{\partial u} u \quad (6)$$

It is important to note that, although our local wave speed approximation is weak for a non-linear conservation law, it does not affect the scheme's ability to conserve mass or reduce oscillations around shocks and jumps. Because this wave speed is used only as a penalty for numerical dispersion, at worst this will only make our scheme more dispersive than the original KT scheme. However, from problems in which the advective term is linear with respect to  $u$ , our scheme will be exactly the same as KT and more computationally efficient, as we would not need to estimate the spectral radius of the Jacobian of  $f(u)$ .

To validate this modeling approach used in FINCH, we will consider using our modeling framework to attempt to solve the Buckley-Leverett Equation (BLE) shown in Equation 7 below. This is a non-linear conservation law problem that is typically used to model fluid dynamics in two-phase flow through porous media. This is a similar type of problem to that which we are ultimately interested in solving and is therefore a good test case for the modeling framework.

$$\frac{\partial u}{\partial t} + \frac{\partial}{\partial z} \left( \frac{u^2}{u^2 + (1-u)^2} \right) = \frac{\partial}{\partial z} \left( 0.04u(1-u) \frac{\partial u}{\partial z} \right) \quad (7)$$

The Buckley-Leverett Equation involves both a non-linear advection term and a disappearing non-linear diffusion term. We can place this equation into our scheme by setting up the advection ( $v$ ) and diffusion ( $D$ ) parameters as shown in Equations 8 and 9. However, recall from the discussion on the estimation of the maximum local wave speed that our approximation of this parameter is weak for the non-linear advection case. Because of this weak approximation of that parameter, we expect our scheme to be more numerically dispersive for these types of problems compared to the original Kurganov and Tadmor (KT) scheme.

$$v = \frac{u}{u^2 + (1-u)^2} \quad (8)$$

$$D = 0.04u(1-u) \quad (9)$$

Figure 34 shows the numerical results of our scheme against the results of the KT (2000) scheme for the solution to the BLE problem. Overall, our scheme matches fairly well against the KT (2000) scheme, but does show more numerical dispersion around the sharp boundary as expected. However, because our scheme did not need to calculate the spectral radius of the Jacobian of the advective term, it is actually more computationally efficient than the KT (2000) scheme.

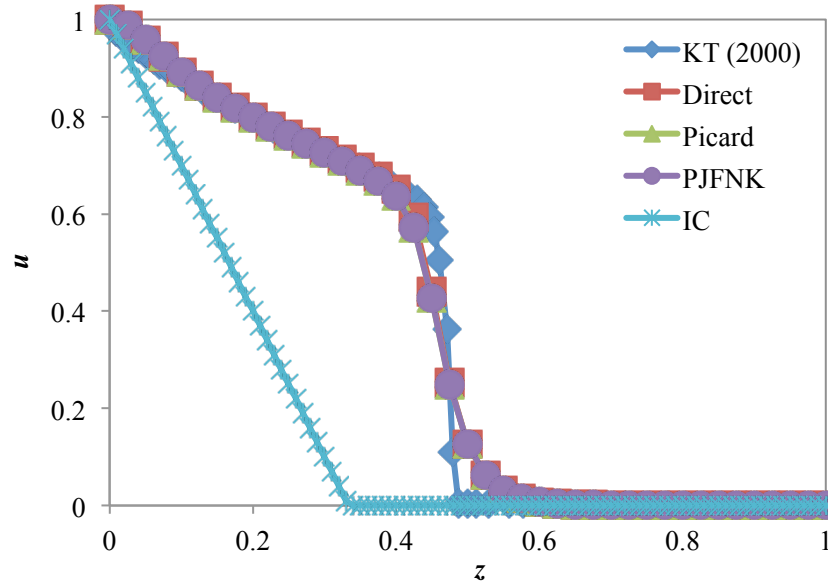


**Figure 32. BLE simulation results for each solution method against the solution reported in literature.** Our results are slightly more numerically dispersive, but that may be attributed to the weak approximation to the local wave speed. The simulation started from the initial conditions (IC) shown above at  $t = 0$  and ended at  $t = 0.2$ .

## 2.5 Equilibria Kernels

### 2.5.1 GSTA

The GSTA model presented by Llano-Restrepo and Mosquera (2009) was originally presented as an alternate form of Hill's statistical model. Their aim was to provide a physical significance and reinterpretation of the parameters of Hill's model in such a way that they could be correlated with temperature to obtain site-specific enthalpies and entropies. A summary of the GSTA model and its parameters are as follows:

$$q = \frac{q_{\max}}{m} \frac{\sum_{n=1}^m n K_n P^n}{1 + \sum_{n=1}^m K_n P^n} \quad (10)$$

$$K_n = K_n^o / (P^o)^n \quad (11)$$

$$\ln K_n^o = -\frac{\Delta H_n^o}{RT} + \frac{\Delta S_n^o}{R} \quad (12)$$

where  $m$  is the number of adsorption sites available to adsorbate molecules,  $K_n$  is the equilibrium constant relative to the adsorption of  $n$  molecules in a network of available adsorption sites,  $K_n^o$  is the dimensionless equilibrium constant,  $P^o$  is the standard state pressure (100 kPa),  $\Delta H_n^o$  is the standard enthalpy of adsorption of  $n$  molecules in a network of sites, and  $\Delta S_n^o$  is the standard entropy of adsorption of  $n$  molecules in a network of sites. The model contains at most  $2 + m$  parameters ( $q_{\max}$ ,  $m$ , and the  $K_n$ 's) that must be determined through correlations with equilibrium data, but if some information is known about the adsorbent, such as theoretical capacity and heterogeneity, then one could independently provide the  $q_{\max}$  and  $m$  parameters (Llano-Restrepo and Mosquera, 2009), thereby reducing the number of adjustable parameters to  $m$  (i.e., the number of equilibrium  $K_n$  parameters).

The form of the GSTA equation is indefinite and nonlinear and therefore requires the use of a non-linear regression technique to accommodate the optimization of the parameters within the model. There are a number of non-linear optimization routines available (e.g. Newton's method, steepest-decent, trust region, etc.), but for the specific purpose of data correlation, a least squares method would be most applicable (Madsen et. al, 2004). Specifically for the codes developed here, we utilize *lmfit*, a C library capable of quickly performing non-linear optimization using the Levenberg-Marquardt's (LM) algorithm (Wuttke, 2013).

The size of the solution vector for the GSTA equation represents the number of adjustable equilibrium parameters of the model. Note that the  $q_{\max}$  parameter is not considered to be adjustable as it represents the theoretical maximum adsorption capacity for a particular adsorbate-adsorbent system. Without any knowledge as to the heterogeneity of the adsorbent, the logical course of action is to search for all parameter solutions for every applicable size of the solution vector and compare each solution's Euclidean norms to determine which describes the data best. Computationally, this is very time consuming, but can be optimized by careful



elimination of unnecessary solution searches and setting up an objective function whose purpose is to minimize the size of the solution vector.

Minimizing the number of parameters in the GSTA model will simplify the calculations and reduce the possibility of over-fitting or over describing a data set with unnecessary parameters. This can be accomplished by creating an objective function that serves to penalize data correlations, which have a large number of parameters or a small number of data points. Such an objective function is as follows:

$$F_{obj} = \sqrt{\frac{\sum_i [(y_i - f(x_i, \mathbf{t})) / y_i]^2}{M - m - 1}} \quad (13)$$

The parameters of the objective function are as follows:  $y_i$  is the experimental y-axis value of the data set,  $f(x_i, \mathbf{t})$  is the function evaluated with the optimized parameter set  $\mathbf{t}$  at x-axis value  $x_i$ ,  $M$  is the total number of data points available, and  $m$  is the number of parameters in the  $\mathbf{t}$  vector. While the overall adequacy of the model to represent the data would be determined by the Euclidean norm, the most suitable solution with the least number of parameters would be determined by the objective function. Therefore, the objective function would serve as the final criterion in determining the number of parameters in the GSTA model.

The systematic procedure necessary to find the most suitable number of parameters is to start with the minimum number of parameters ( $m = 1$ ), find an applicable solution via non-linear least squares regression, then increment the number of parameters by one. At each stage, the values of the euclidean norm and objective function are observed and compared to the previous stage. This process is continued until the maximum number of parameters applicable to the system has been reached. Additionally, once we observe that the euclidean norm is no longer improving by adding more parameters, no further parameter solutions will be observed by any isotherm. Finally, the most suitable solution is determined by locating the smallest  $F_{obj}$  from all solutions found across all isothermal data.

Unlike linear least squares regression, a non-linear regression analysis must start with an initial guess being made to the solution vector ( $\mathbf{t}$ ). Then, gradient observations must be made through the use of Jacobian matrices ( $\mathbf{J} = \partial f / \partial \mathbf{t}$ ) in order to establish a magnitude and direction in which to shift the parameters of the model. This procedure is repeated until a reasonable solution is located, but due to the nature of nonlinear regression, the ability to obtain solutions can be dependent on the initial values given in the solution vector (Madsen, 2004). To combat this issue, a number of techniques are adopted to ensure that the initial guess vector is as close to the solution as possible and that guesses being made are not arbitrary or irrelevant in magnitude.

The first guess is realized when considering that the GSTA model is exactly equal to the Langmuir equation when the number of equilibrium parameters ( $m$ ) is equal to one. Under this condition, it is possible to linearize the equation and perform a standard linear regression to obtain the parameters. The optimized parameters from the linear regression are then used in the non-linear analysis as the initial guess for the parameter vector.

The previously optimized parameter is then used as a basis for making the initial guess for the two-parameter model. Using that information, the two unknown parameters are given an

initial value equal in magnitude to the previously found one parameter. Maintaining the relative magnitudes in all parameters will ensure that no parameter is seen as irrelevant in the current iteration and will therefore be treated as equally important in the overall model.

All subsequent guesses, for three parameters and beyond, are made as order-of-magnitude slope projections from two previously optimized parameters, and the new parameter in the vector is a slope project from the other parameters within the vector. For example, if the current iteration is meant to find a three parameter ( $m = 3$ ) solution, then the initial guess for the  $K_1$  parameter will be based off of the optimized  $K_1$  parameters from the two and one parameter solutions, the  $K_2$  parameter will also be based off of that slope, and the  $K_3$  parameter will be based off of the slope between the  $K_1$  and  $K_2$  parameters that apply for the current iteration.

The optimization code for the GSTA model contains a variety of different subroutines to determine the overall wellness of the model compared to the data. Such routines include, but are not limited to: (1) educated initial value guessing for the starting point of the non-linear regression analysis, (2) smoothness evaluation of the solution vector after optimization, and (3) an orthogonal linear regression of all the optimized parameters across temperature to obtain a set of temperature independent parameters that can be used to make model predictions for the adsorption behavior at other temperatures. The culmination of all of these routines, and others, allows the code to fully analyze entire sets of data all at once.

Results of the GSTA code analysis with the Grace Davison (2002) adsorption data can be viewed below in Figure 35, which shows the best results determined by the GSTA code for the adsorption isotherms of water vapor on the Grace Davison zeolite. Our code had determined that the least number of equilibrium parameters needed to describe this set of data was six. A physical interpretation of this result would be that the adsorbent crystal contains six different adsorption sites, each with its own energy signature. As a result, the GSTA model may reveal information regarding the heterogeneity of the adsorption system if that information is unknown. On the other hand, if we are certain about the number of energetically different sites there are in an adsorbent, then we can provide this information accordingly and get a different analytical result from the code.

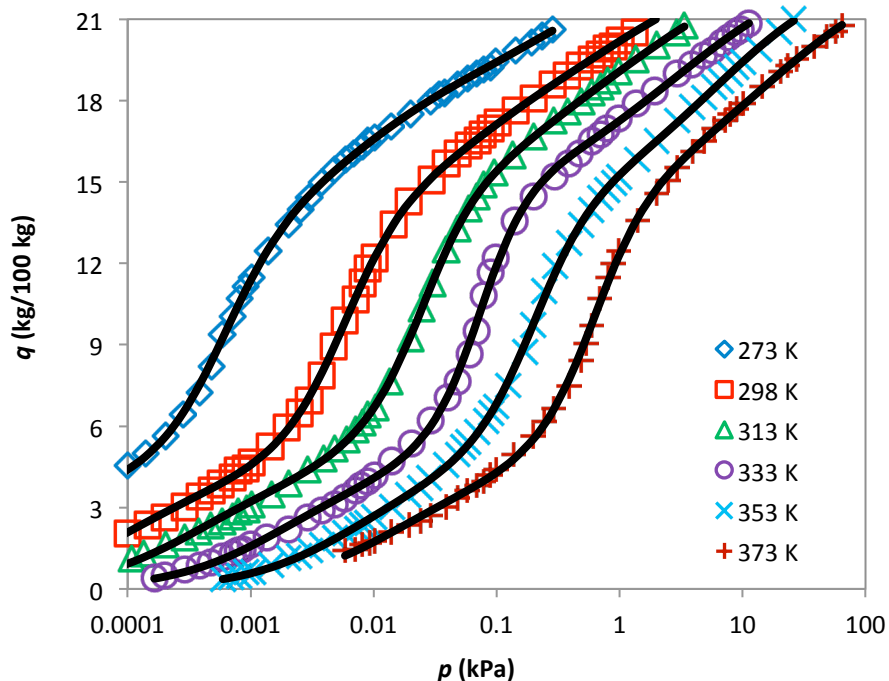


**Figure 33. GSTA analysis results for the Grace Davison (2002) water vapor adsorption curves.** Solid lines show the results of the optimization routine against the data.

In addition to analyzing the Grace Davison (2002) isotherms, we also used the GSTA optimization code to provide results for the water vapor adsorption data collected at Syracuse University under this project. The adsorbent used at Syracuse is of a slightly different material makeup and therefore the adsorption behavior recorded was different from the Grace Davison curves. Those differences are picked up by the GSTA code and can be seen in the results in Figure 36. For this set of data, the code determined that the best number of parameters to describe the system was four equilibrium parameters as opposed to the six parameters found for the Grace Davison data. A physical interpretation of these results may be that the Grace Davison adsorbent is more energetically heterogeneous than the Syracuse adsorbent. However, a more in depth analysis is needed for an exact determination of why there is a physical difference between the Grace Davison adsorbent and the Syracuse adsorbent.

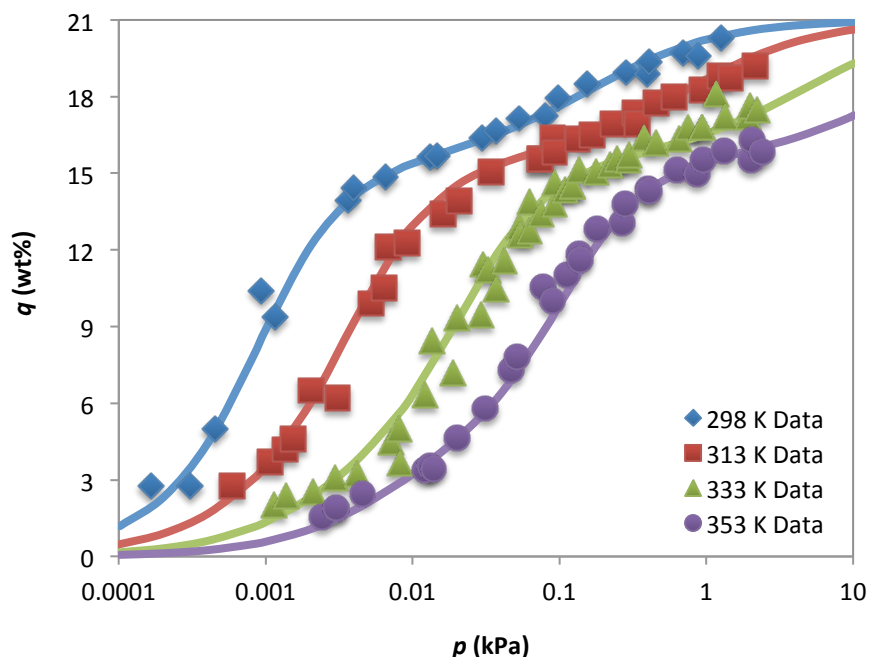


**Figure 34. GSTA analysis results for the Syracuse water vapor adsorption curves.** Solid lines represent the model using the optimal temperature independent parameters found from the GSTA optimization routine shown in Table 8.

**Table 8. Optimized parameter results for the GSTA analysis on the Syracuse University adsorption data. The maximum adsorption capacity ( $q_{\max}$ ) was assumed 21% by weight, which is the theoretical maximum.**

$n$ (site)	$\Delta H_n^\circ$ (kJ/mol)	$\Delta S_n^\circ$ (J/K/mol)
1	-46.60	-53.70
2	-125.02	-221.07
3	-193.62	-356.73
4	-272.23	-567.46

The GSTA code was also used to analyze data published by researchers from Pacific Northwest National Laboratory (PNNL) for isotherms of Kr and Xe on Metal Organic Frameworks (MOFs). Some of their collected isotherm data have been published in the Journal of the American Chemical Society (JACS) for a zinc and copper type FMOF (Fernandez et al., 2012). The parameter values of that optimization are shown below in Table 9 for both Kr and Xe adsorption on FMOFZn, a partially fluorinated zinc MOF. Those parameters were then used to plot the GSTA isotherm model against the actual data, shown in Figure 36.

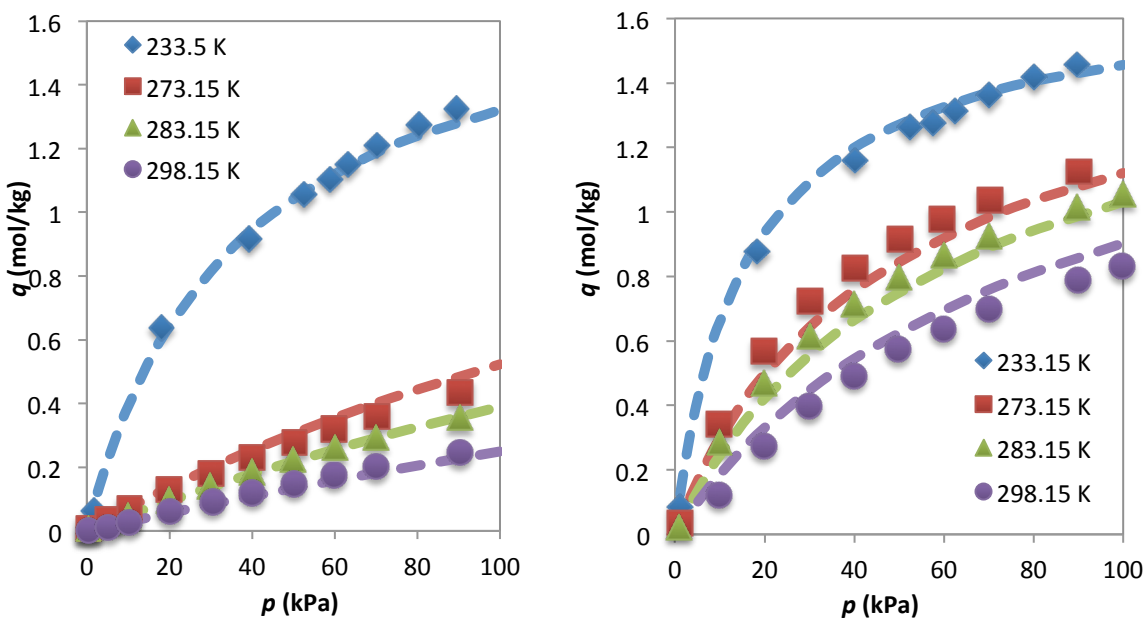


**Figure 35.** Equilibrium isotherms of krypton and xenon on FMOFZn plotted against the results of the GSTA isotherm model using the optimized equilibrium parameters from Table 3. The figure on the left shows the krypton isotherms and the figure on the right shows the xenon isotherms.

**Table 9.** Temperature independent GSTA parameters found for Kr and Xe on FMOFZn

Species	$q_{\max}$ (mol/kg)	$n$ (site)	$\Delta H_n^\circ$ (kJ/mol)	$\Delta S_n^\circ$ (J/K/mol)
<i>Krypton</i>	1.80	1	-25.32	-100.10
<i>Xenon</i>	1.71	1	-15.10	-43.10
		2	-30.11	-99.10

Although the GSTA isotherm model worked well to describe the equilibrium behavior of Kr and Xe on FMOFZn, it ended up performing poorly for the case of Kr and Xe on FMOFCu. This is due to an apparent inversion in the adsorption behavior of both systems around some critical temperature between 0 and -20 °C. According to Fernandez et al. (2012), this inversion in adsorption behavior is caused by a change in the physical structure of the adsorbent at low temperatures, which blocks spaces in the FMOF that were once accessible to Xe molecules, i.e., molecular sieving. Figure 38 below shows the relationship between the optimized equilibrium GSTA parameters and temperature for both Kr and Xe on FMOFCu. Theoretically, this relationship should be linear, but the data show strong non-linearity, making it impossible to model with the temperature-independent GSTA parameters. However, it may still be possible to use the GSTA isotherm to model the system if the model is split around the critical temperature.

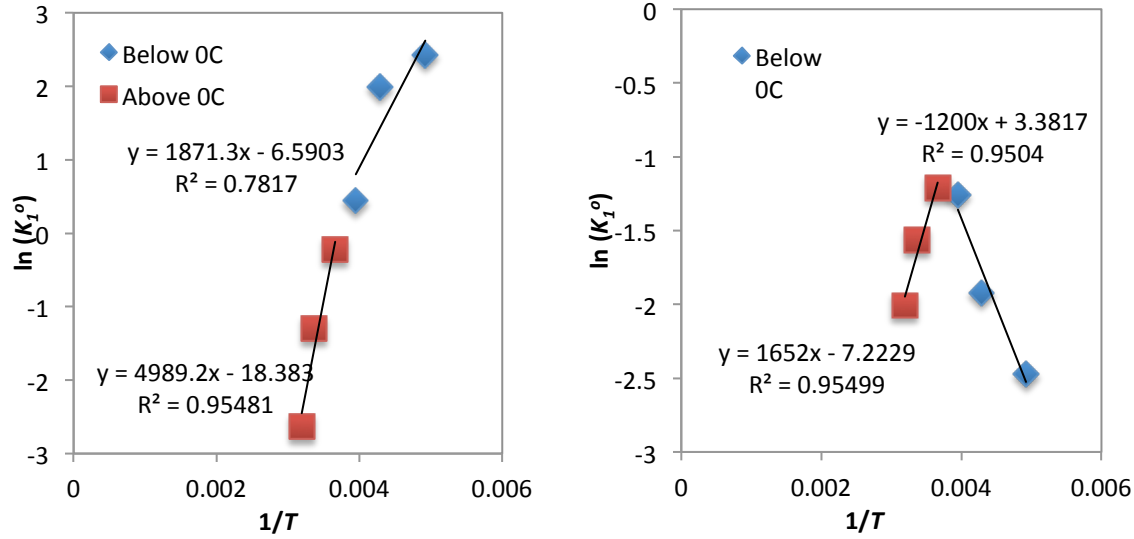


**Figure 36. Optimized equilibrium parameters plotted against the temperatures for which they apply.** The relationship shown should be linear according to the van't Hoff expression (Equation 12). However, the data show a non-linear temperature relationship split over a critical temperature. The figure on the left is for Kr on FMOFCu and the figure on the right is for Xe on FMOFCu.

## 2.5.2 MSPD

In order to expand the GSTA isotherm model into multi-component models, it is often necessary to account for the activity of each species in the adsorbed phase. Without doing so, we would be forced to assume that the adsorbed phase behaves as an ideal solution. That assumption would create a major limitation in the model and could lead to large errors or differences between the predicted and measured adsorption capacities. To correct this issue, we developed a modified version of the Spreading Pressure Dependent (SPD) activity model originally presented by Talu and Zwiebel (1986). This modified version of the model retains the same physical significance of the original model, but allows us to more easily incorporate it into predictive multi-component models.

Equations 14 through 19 outline the portions of the MSPD model that remained unchanged from the original SPD model, while equations 20 through 23 represent the portions of SPD that were changed to form the MSPD model. The parameters of the equations below are described as follows:  $s_i$  is the areal shape factor of the  $i^{\text{th}}$  molecule,  $x_i$  is the adsorbed mole fraction of the  $i^{\text{th}}$  component,  $e_{ii}$  and  $e_{ij}$  are the single-component lateral interaction energies,  $Q_i^{st}$  and  $Q_{i,o}^{st}$  are the isosteric heats of adsorption at current loading and zero loading respectively,  $e_{ij}$  and  $e_{ji}$  are the binary lateral interaction energies, and  $\eta_{ij}$  and  $\eta_{ji}$  are the adjustable binary interaction parameters.

$$\ln \gamma_i = s_i \left[ 1 - \ln \left( \sum_{j=1}^N \theta_j \tau_{ji} \right) - \frac{\sum_{j=1}^N \theta_j \tau_{ij}}{\sum_{k=1}^N \theta_k \tau_{kj}} \right] \quad (14)$$

$$\theta_i = \frac{s_i x_i}{\sum_{j=1}^N s_j x_j} \quad (15)$$

$$\tau_{ij} = \exp\left[-\frac{z(e_{ij} - e_{jj})}{2RT}\right] \quad (16)$$

$$\tau_{ji} = \exp\left[-\frac{z(e_{ji} - e_{ii})}{2RT}\right] \quad (17)$$

$$e_{ii} = \frac{2(Q_i^{st} - Q_{i,o}^{st})}{zS_i} \quad (18)$$

$$e_{jj} = \frac{2(Q_j^{st} - Q_{j,o}^{st})}{zS_j} \quad (19)$$

Equations 20 through 23 were altered to reflect two changes being made to the original SPD model: (1) we are using a shifted geometric mean to estimate the binary lateral interaction energies as opposed to the standard geometric mean and (2) the adjustable binary parameters were altered to account for the relative mole fractions of each adsorbed component. In the original SPD model, the binary lateral interactions were determined as follows:  $e_{ij} = e_{ji} = \sqrt{e_{ii}e_{jj}}(1 - \beta_{ij})$ .

$$e_{ji} = \sqrt{(|\mu_{ii}| + e_{ii})(|\mu_{jj}| + e_{jj})} - \alpha_{ji} \sqrt{|\mu_{ii}| |\mu_{jj}|} \quad (20)$$

$$e_{ij} = \sqrt{(|\mu_{ii}| + e_{ii})(|\mu_{jj}| + e_{jj})} - \alpha_{ij} \sqrt{|\mu_{ii}| |\mu_{jj}|} \quad (21)$$

$$\alpha_{ji} = (\eta_{ij} - \eta_{ji}) \left( \frac{x_j}{x_i + x_j} \right) + \eta_{ji} \quad (22)$$

$$\alpha_{ij} = (\eta_{ji} - \eta_{ij}) \left( \frac{x_i}{x_i + x_j} \right) + \eta_{ij} \quad (23)$$

Lateral interactions were represented as a shifted geometric mean as opposed to the standard geometric mean, so that the geometric average of a collection of numbers, both negative and positive in sign, can be calculated correctly. The shifting is accomplished by the parameters  $\mu_{ii}$  and  $\mu_{jj}$ , which represent the maximum change in  $e_{ii}$  and  $e_{jj}$  respectively. These shift factors ensure that the value of the product underneath the square root is always positive. The shift is then corrected for by subtracting the total distance that the shift was made by. This is a common technique used to determine geometric means in economics and finance when determining the average return-on-investment of a particular set of investments (Markowitz, 2012).

The second change made was to allow for the adjustable binary parameters,  $\alpha_{ij}$  and  $\alpha_{ji}$ , to vary with the relative amounts of the adsorbed mole fractions. This change was made observationally after it was realized that the lateral interactions between the different molecules would vary when the mole fractions varied. Additionally, in order to maintain the same basic form of the original SPD model, the new adjustable parameters were formulated in a manner

such that for any relative adsorbed mole fractions,  $\alpha_{ij}$  is always equal to  $\alpha_{ji}$ . This is consistent with the original SPD model in which  $\beta_{ij} = \beta_{ji}$ .

### 2.5.3 GPAST

One of the major hurdles in modeling adsorption in real systems is how to incorporate the effect of multiple components or mixed gases in a single source stream. There are many different processes that may affect the sorption behavior of each species including co-adsorption, inhibition, intermolecular interactions, and competition for the limited sorption sites. As the number of components in the system increases, so does the complexity of developing any experiments to measure and determine the fractional contribution of each species to the total sorption. Therefore, it is paramount that some theories and procedures be used in order to predict the behavior of a multi-component system from available pure component data (Tien, 1994).

In 1965, Myers and Prausnitz developed a fundamental theory for adsorption of gas mixtures known as Adsorbed Solution Theory (AST). It is represented by a series of six equations, which relates the adsorption of the pure components back to the Gibb's adsorption isotherm, the spreading pressure ( $\pi$ ), and the mole fractions of each component in the adsorbed phase ( $x_i$ ). The assumptions being employed in this theory are as follows: (1) the adsorbate in the adsorbed phase is ideal such that Raoult's Law applies and (2) the temperature, spreading pressure, and chemical potential of any adsorbate in any of the two phases are the same.

Equations 24 through 29 below show the six equations from AST. Note that subscript  $i$  denotes the  $i^{th}$  component in the mixture, superscript  $o$  denotes the pure component pressure ( $p$ ) or sorption capacity ( $q$ ) at equilibrium,  $\Pi$  is a lumped parameter that includes spreading pressure ( $\pi$ ) and specific surface area ( $A$ ) of the adsorbent,  $P_T$  is the total pressure of the gas mixture,  $y_i$  is the mole fraction of component  $i$  in the gas phase,  $N$  is the number of components in the mixture, and  $\gamma_i$  is the adsorbed phase activity coefficient for the  $i^{th}$  component. For the case of an ideal solution, the activity of all components is equal to one and the gradient term in Equation 26 is zero.

$$\Pi = \frac{\pi A}{RT} = \int_0^{p_i^o} \frac{q_i^o}{p_i^o} dp_i^o \quad (24)$$

$$P_T y_i = p_i^o x_i \gamma_i \quad (25)$$

$$q_T = \left[ \sum_{i=1}^N \frac{x_i}{q_i^o} + \sum_{i=1}^N x_i \left( \frac{\partial \ln \gamma_i}{\partial \Pi} \right)_{T,x} \right]^{-1} \quad (26)$$

$$\sum_{i=1}^N x_i = 1 \quad (27)$$

$$q_i = q_T x_i \quad (28)$$

$$q_i^o = f(p_i^o) \quad (29)$$

In 1998, Sakuth et al. had proposed an extension of AST, called Predictive Real Adsorbed Solution Theory (PRAST), that intended to estimate the binary interaction parameters



of an activity model by looking at the limiting behavior of each component's pure isotherm and using that information to calculate the infinite dilution activities. As a result, each of the pure-component isotherms must obey Henry's Law at low pressure (Equation 30), which is a thermodynamic expectation for gas adsorption (Talu and Myers, 1988). The infinite dilution activities for each component can then be evaluated from Equation 31 and combined with the activity model to set up a system of equations in which the adjustable parameters of the model can be explicitly solved for.

$$\lim_{p_i^o \rightarrow 0} \frac{q_i^o}{p_i^o} = He_i \quad (30)$$

$$\gamma_i^\infty(\pi_j) = \frac{q_j^o(\pi_j)}{He_i p_i^o(\pi_j)} \quad (31)$$

The principal idea governing our Generalized Predictive Adsorbed Solution Theory (GPAST) is to predict the parameters of the activity model, using each unique binary pair of species within the overall system. By looking at each species pair-wise, as opposed to altogether, the PRAST estimate of the infinite dilution activity (Equation 31) can be used directly and applied serially to each unique pair. This is now possible because, for a given binary pair, the adsorbed mole fraction of species  $j$  will approach unity ( $x_j = 1$ ) as the adsorbed mole fraction of species  $i$  approaches zero ( $x_i = 0$ ).

To visualize this concept, consider a system that has three adsorbable species: A, B, and C. In this system, there are three unique binary pairs whose infinite dilution activities must be determined: A+B, A+C, and B+C. Note that the reverse of these pairings (i.e., B+A, C+A, and C+B) is not considered because they are not unique. The infinite dilution activities are determined by Equation 31 for each species in a pair, such that each pair results in two infinite dilution activities:  $\gamma_A^\infty(\pi_B)$  &  $\gamma_B^\infty(\pi_A)$ ,  $\gamma_A^\infty(\pi_C)$  &  $\gamma_C^\infty(\pi_A)$ , and  $\gamma_B^\infty(\pi_C)$  &  $\gamma_C^\infty(\pi_B)$ . When this idea is extended to an  $N$ -component system, the number of unique pairs to that system becomes  $N(N-1)/2$  and the number of infinite dilution activities to determine is  $N(N-1)$ .

From here, GPAST becomes a combinatorial and serial application of the PRAST system. Recall that in the PRAST method (Sakuth et al., 1998), a system of equations involving the activity model and the calculated infinite dilution activities is set up in order to solve for the parameters of the activity model for that binary system. This same procedure is used in GPAST, but is applied sequentially over each binary set within the overall system, such that all of the activity model parameters for each pair of species can be determined.

To demonstrate this concept, consider Equations 14 and 15 to be the activity model chosen to describe the non-ideal behavior at the surface of the adsorbent. To simplify this example, it will be assumed that the molecular shape factors ( $s_i$ ) can be independently determined based on the adsorbing molecule size characteristics and that the only model parameters to be determined are the Boltzmann weighting factors:  $\tau_{ij}$  and  $\tau_{ji}$ . Then, continuing from the previous ternary example, a system of equations for each binary pair can be formulated as shown below in Equations 32-37.

$$\lim_{\substack{x_A \rightarrow 0 \\ x_B \rightarrow 1}} (\ln \gamma_A) = \ln \gamma_A^\infty(\pi_B) = s_A (1 - \ln \tau_{BA} - \tau_{AB}) \quad (32)$$

$$\lim_{\substack{x_B \rightarrow 0 \\ x_A \rightarrow 1}} (\ln \gamma_B) = \ln \gamma_B^\infty(\pi_A) = s_B (1 - \ln \tau_{AB} - \tau_{BA}) \quad (33)$$

$$\lim_{\substack{x_A \rightarrow 0 \\ x_C \rightarrow 1}} (\ln \gamma_A) = \ln \gamma_A^\infty(\pi_C) = s_A (1 - \ln \tau_{CA} - \tau_{AC}) \quad (34)$$

$$\lim_{\substack{x_C \rightarrow 0 \\ x_A \rightarrow 1}} (\ln \gamma_C) = \ln \gamma_C^\infty(\pi_A) = s_C (1 - \ln \tau_{AC} - \tau_{CA}) \quad (35)$$

$$\lim_{\substack{x_B \rightarrow 0 \\ x_C \rightarrow 1}} (\ln \gamma_B) = \ln \gamma_B^\infty(\pi_C) = s_B (1 - \ln \tau_{CB} - \tau_{BC}) \quad (36)$$

$$\lim_{\substack{x_C \rightarrow 0 \\ x_B \rightarrow 1}} (\ln \gamma_C) = \ln \gamma_C^\infty(\pi_B) = s_C (1 - \ln \tau_{BC} - \tau_{CB}) \quad (37)$$

Since the infinite dilution activities have already been calculated by Equation 31, and the shape factors are independently determined, these equations represent a uniquely solvable, non-linear system of six equations and six unknowns. Each  $\tau_{ji}$  determined from these equations is then used back in the original activity model to represent the non-ideality that occurs at the surface for the ternary system. From this point on, the standard AST system of equations (Equations 24-29) can be used to predict the adsorbed amounts in the system under various conditions of temperature and pressure, using the activity model with the parameters ( $\tau_{ji}$ ) calculated from GPAST.

## 2.5.4 MAGPIE

The MAGPIE kernel is the culmination of all previously discussed equilibria kernels for both single- and multi-component gas-solid adsorption systems. As such, it can be used as both an analytical tool and a predictive model. Included within MAGPIE is the GSTA optimization routine that was developed for the purpose of obtaining the equilibrium parameters from the GSTA model (Llano-Restrepo and Mosquera, 2009). We can then take those optimum parameters and use them in the prediction of the adsorption in a mixed gas system.

The multi-component analysis is performed once all the parameters of the GSTA isotherm have been determined for each adsorbing species in the multi-component system. Those parameters are fed into MAGPIE as inputs for the Generalized Predictive Adsorbed Solution Theory (GPAST) and the Modified Spreading Pressure Dependent (MSPD) activity model. MAGPIE then combines GPAST with the GSTA and MSPD models to perform a prediction on the multi-component system.

To verify the MAGPIE predictions, we collected a series of literature data for single- and multi-component systems at both low (Talu and Zwiebel, 1986) and high pressures (Ritter and Yang, 1987). Figures 39 and 40 show the results of MAGPIE using those entire data sets which are composed of binary, ternary, quaternary, and quinary mixtures of CO<sub>2</sub>, H<sub>2</sub>S, and C<sub>3</sub>H<sub>8</sub> on H-mordenite for the Talu and Zwiebel data and CO<sub>2</sub>, CO, CH<sub>4</sub>, H<sub>2</sub>, and H<sub>2</sub>S on activated carbon at elevated pressures (above 1 atm) for the Ritter and Yang data. Table 10 shows the error

distribution comparisons between MAGPIE and the Ideal Adsorbed Solution Theory (IAST). This demonstrates that MAGPIE performs better than IAST since it has reduced the errors by up to 48%.

**Table 10. Summary of the statistical analysis of the error distributions**

	MAGPIE	IAST	Improvement (%)
<b>Absolute Error of Mole Fractions</b>			
<i>Average</i>	0.001	0.001	0.00
<i>Standard Deviation</i>	0.062	0.097	-36.14
<b>Relative Error of Adsorbed Totals</b>			
<i>Average</i>	-0.048	-0.092	-48.43
<i>Standard Deviation</i>	0.114	0.139	-17.72

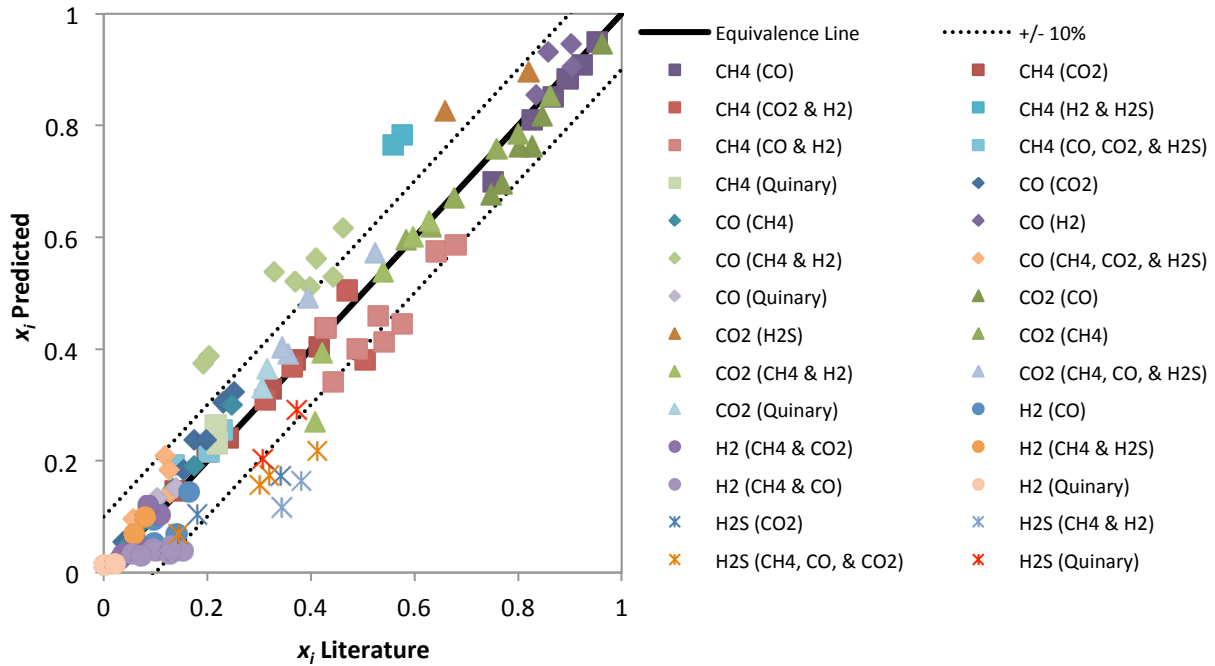


**Figure 37. Results of GPAST with the mSPD activity model compared against the experimentally determined adsorbed mole fractions of each component.** This figure represents the entire data set provided by Ritter and Yang (1987) in literature. All data were collected under isothermal conditions and elevated pressures ( $> 1$  atm).

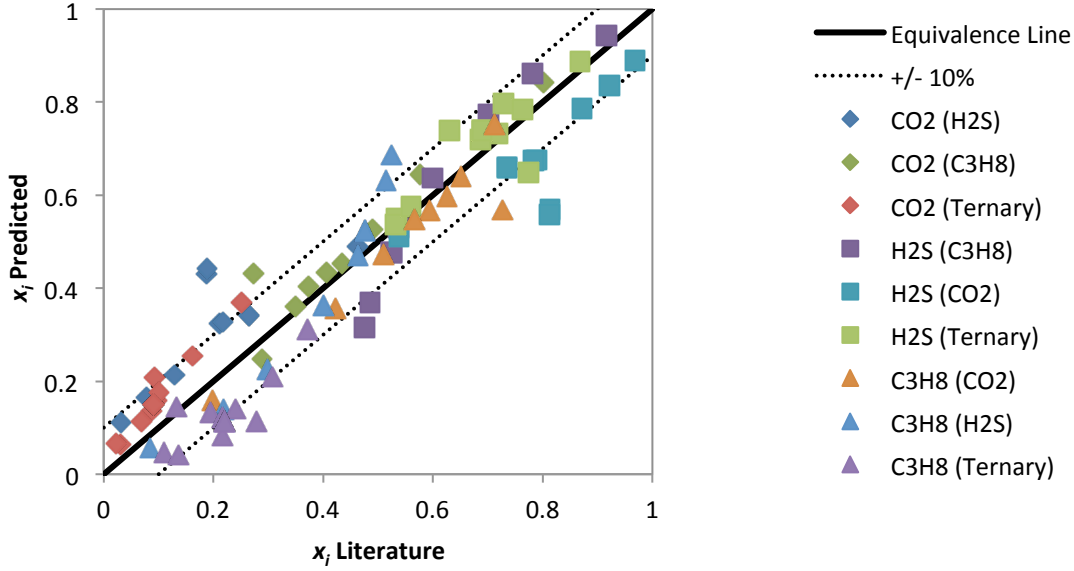


**Figure 38. Results of GPAST with the mSPD activity model compared against the experimentally determined adsorbed mole fractions of each component.** This figure represents the entire data set provided by Talu and Zwiebel (1986) in literature. All data were collected under isothermal conditions and low pressures (< 1 atm).

## 2.6 Kinetic Kernels

### 2.6.1 SKIMMER

In addition to equilibrium modeling, we have developed the SKIMMER model that may be used to describe the diffusion and kinetics of adsorption for commercial pellet-like adsorbents, as shown in Figure 41. The partial differential equations necessary to describe this system are summarized below in Equations 38 through 40 and are derived by considering a mass balance of the adsorbate (Tien, 1994; Simo et al., 2009), both in the pore space and in the crystal, as it diffuses into each sphere. Pore space concentration of adsorbate ( $c$ ) and adsorbed phase concentration ( $q$ ) are coupled with each other at the boundary of the crystal using the “local equilibrium” assumption (Equation 41).

$$\frac{\partial q}{\partial t} = \frac{1}{r^2} \frac{\partial}{\partial r} \left[ r^2 D_c \frac{\partial q}{\partial r} \right] \quad (38)$$

$$\bar{q} = \frac{3}{a_c^3} \int_0^{a_c} q r^2 dr \quad (39)$$

$$\varepsilon_p \alpha \frac{\partial c}{\partial t} + (1 - \alpha) \frac{\partial \bar{q}}{\partial t} = \frac{1}{R^2} \frac{\partial}{\partial R} \left[ R^2 D_p \varepsilon_p \alpha \frac{\partial c}{\partial R} \right] \quad (40)$$

$$q(a_c, t) = f(c(R, t)) \quad (41)$$

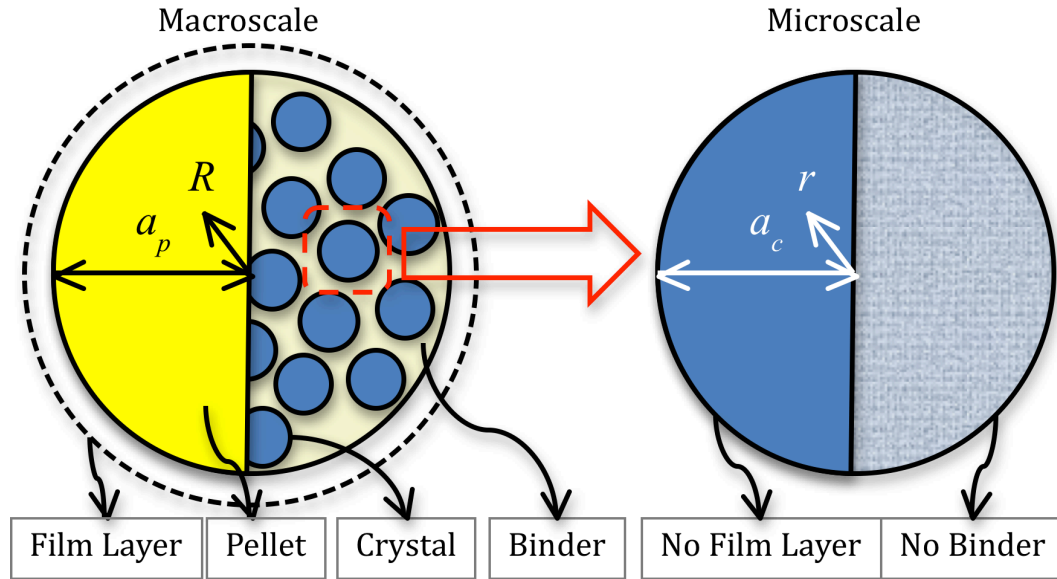


**Figure 39. Diagram showing the idealization of a commercial, biporous adsorbent made up of a collection of adsorbent crystals held together by an inert binder material.**

For the boundary of the pellet, there are two possible boundary conditions to be considered: (i) if the mass transfer resistance across the film layer of the pellet can be neglected, then a Dirichlet boundary condition can apply (Equation 42), (ii) otherwise, one must include a Neumann type boundary condition (Equation 43) in order to describe the rate of flux of material into the pellet. The boundary condition at the center of each sphere is a no flux or symmetry condition (Equation 44). This type model is commonly referred to as a Two-Phase (Jubin, 1994) or Biporous (Malek and Farooq, 1997) adsorption model because of the two different diffusion processes involved.

$$c(a_p, t) = C_b \quad (42)$$

$$D_p \left. \frac{\partial c}{\partial R} \right|_{R=a_p} = k_f (C_b - c(a_p, t)) \quad (43)$$

$$\left. \frac{\partial c}{\partial R} \right|_{R=0} = 0 = \left. \frac{\partial q}{\partial r} \right|_{r=0} \quad (44)$$

Below are the variables and parameters from Equations 38 through 44 and their physical significance:

- $c$  is the concentration of adsorbate in the pore space of the pellet
- $q$  is the concentration of adsorbate which has been adsorbed onto the crystal
- $\bar{q}$  is the average adsorbed concentration in a crystal
- $D_c$  is the crystalline diffusivity
- $a_c$  is the nominal crystal radius

- $\varepsilon_p$  is the porosity of the binder (i.e., volume of voids per volume binder)
- $\alpha$  is the binder fraction of the pellet (i.e., volume of binder per volume of pellet)
- $D_p$  is the macropore diffusivity
- $a_p$  is the nominal pellet radius
- $C_b$  is the concentration of adsorbate in the bulk phase
- $k_f$  is the film mass transfer coefficient

Many of these parameters can be determined from the physical properties of the particular system of interest, such as flow rate, pore size, and temperature, through either dimensionless numbers or other theoretical relationships. However, other parameters may require experimental data in order to determine.

Tien (1994) offers several techniques and expressions for determining the pellet diffusivity ( $D_p$ ) and mass-transfer coefficient ( $k_f$ ) based on the system parameters (see Equations 45 through 48 below). Parameters below are as follows:  $\varepsilon_p$  is pellet porosity,  $\tau$  is tortuosity,  $D_m$  is molecular diffusivity,  $D_k$  is Knudsen diffusivity,  $r_p$  is nominal pore radius,  $T$  is temperature,  $MW$  is molecular weight of adsorbing species,  $d_p$  is pellet diameter,  $Re$  is the Reynold's number, and  $Sc$  is the Schmidt number.

$$D_p = \frac{\varepsilon_p D_m}{\tau} \quad (45)$$

$$D_k = 9700 r_p \left( \frac{T}{MW} \right)^{1/2} \quad (46)$$

$$\bar{D}_p^{-1} = D_p^{-1} + D_k^{-1} \quad (47)$$

$$k_f = \frac{D_m}{d_p} \left[ 2 + 1.1 Re^{0.6} Sc^{0.3} \right] \quad (48)$$

Each species in a gas mixture will have a different molecular diffusivity ( $D_{m,i}$ ) that can be determined from the binary diffusivities ( $D_{ij}$ ) between all species present (Equation 49). The binary diffusivities vary theoretically with temperature and the viscosities ( $\mu_i$ ), densities ( $\rho_i$ ), and molecular weights ( $MW_i$ ) of each species according to Equation 50 (Wilke, 1950). We can determine the temperature relationship for the density of each species using the ideal gas law (Equation 51) and use the Sutherland's equation (Equation 52) to relate the viscosity of each pure species with temperature (Sutherland, 1893) using a reference state viscosity ( $\mu_i^o$ ) and temperature ( $T_i^o$ ) as well as the Sutherland's constant ( $C_i$ ). Combining all these theoretical models then allows us to accurately estimate the diffusivity effects for the kinetics of adsorption.

$$D_{m,i} = \frac{1 - y_i}{\sum_{j \neq i} \frac{y_j}{D_{ij}}} \quad (49)$$

$$D_{ij} = \frac{(4/\sqrt{2})(MW_i^{-1} + MW_j^{-1})^{1/2}}{\left[ \left( \frac{\rho_i^2}{1.92\mu_i^2 MW_i} \right)^{1/4} + \left( \frac{\rho_j^2}{1.92\mu_j^2 MW_j} \right)^{1/4} \right]^2} \quad (50)$$

$$\rho_i = \frac{P_T MW_i}{RT} \quad (51)$$

$$\mu_i = \mu_i^o \frac{T_i^o + C_i}{T + C_i} \left( \frac{T}{T_i^o} \right)^{3/2} \quad (52)$$

The Reynolds and Schmidt numbers (Equations 53 and 54) are also implicit functions of temperature and pressure (Wakao and Funazkri, 1978) because they relate kinematic viscosities ( $\nu_T$ ) and diffusivities with the flow rates ( $u_s$ ) and sizes of the particles ( $d_p$ ). To determine the kinematic viscosity of the mixed gas system requires the dynamic viscosity ( $\mu_T$ ) and the total density of the gas phase ( $\rho_T$ ). While the total density can be determined from ideal gas law, the dynamic viscosity of the mixed gas must be determined from a theoretical model, such as that outlined in Equations 55 through 57 (Krieger, 1951). This model takes into account the mole fractions ( $y_i$ ) of each species together with the binary diffusivities and a temperature correction factor ( $\chi$ ) to approximate the mixed gas viscosity.

$$Re_i = \frac{u_s d_p}{\nu_T} \quad (53)$$

$$Sc_i = \frac{\nu_T}{D_{ij}} \quad (54)$$

$$\mu_T = \sum_{i=1}^N \frac{\mu_i}{1 + \frac{113.65 \chi \mu_i T}{y_i MW_i} \sum_{j \neq i}^N \frac{y_j}{D'_{ij}}} \quad (55)$$

$$\chi = 0.873143 + (0.000072375)T \quad (56)$$

$$P^o D'_{ij} = P_T D_{ij} \quad (57)$$

Combining the theory and models from Equations 45 through 57 allows us to determine all parameters within the SKIMMER system of equations, except for the crystalline diffusivity. This parameter must be determined experimentally or optimized for from sets of kinetic adsorption data. Additionally, this parameter is likely to be a function of the actual adsorbed amount on the surface of the adsorbent crystals (Simo et al., 2009; Do et al., 2001). Therefore, to fully describe the kinetics of adsorption, the physical diffusion equations must be coupled with the adsorption equilibria kernels discussed earlier.

### 2.6.2 SKUA

The SKUA application combines SKIMMER and MAGPIE kernels in order to give a more complete description of the adsorption process for a single pellet. The equilibrium point determined by MAGPIE is applied to the crystal boundary condition within the adsorbent pellet shown in Equation 41 above. At each time step, a different equilibrium point is determined based on the changing conditions of the overall system and the concentration within the pellet binder at a particular location in the pellet. SKUA then serially and implicitly solves the systems of equations to simulate the system response to temperature and pressure at every time step.

Additionally, we need to update the crystalline diffusivity ( $D_c$ ) as the amount adsorbed changes with time. Theoretically, as the pellet loads, the diffusivity should increase because, as more surface sites are utilized, the surface mobility of molecules increases. The opposite effect occurs during desorption, which causes retardation in the rate of removal of adsorbed molecules (Do et al., 2001; Simo et al., 2009). A common diffusion model used to describe this behavior is the Darken expression (Equation 58), which relates the rate of diffusion to changes in the chemical potential gradient of the surface and a corrected diffusivity term ( $D_o$ ). Generally, this expression can be used in conjunction with the isotherm model to provide an explicit function of the crystalline diffusivity with the relative loading of the pellet ( $\varphi$ ). For the case of the Langmuir type isotherm, the Darken expression reduces to Equation 59 below (Do, 1998).

$$D_c = D_o \left( \frac{\partial \ln p}{\partial \ln q} \right) \quad (58)$$

$$D_c = \frac{D_o}{1 - \varphi} \quad (59)$$

Replacing the constant diffusivity in with the variable diffusivity, as defined by Equation 59, provides a more accurate description of the observed uptake behavior in the Syracuse University data shown in Figure 42. In this case, we show only one of the optimized model results for both a constant and variable diffusivity. However, for all data sets, the variable diffusivity model described the Syracuse data with a greater degree of accuracy.



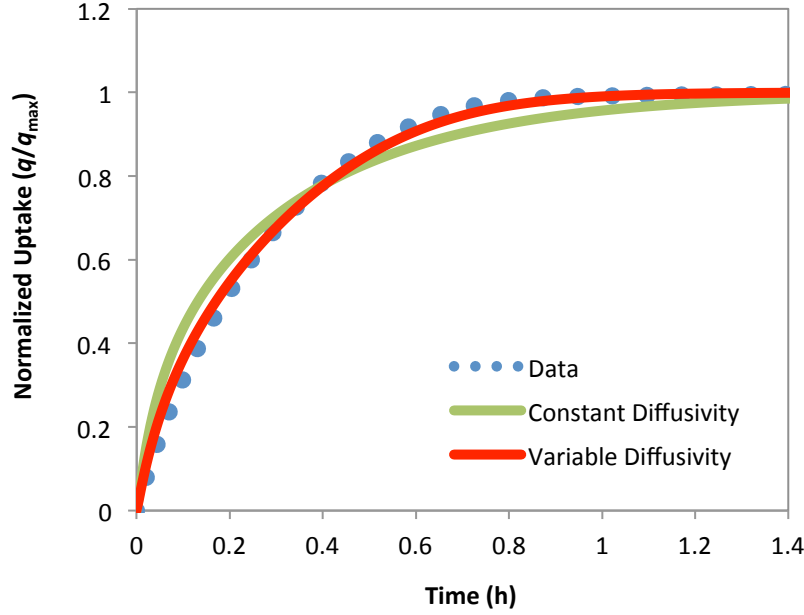


**Figure 40. Comparison between the SKUA optimized model results with constant and variable diffusivities. The data were collected at Syracuse and show the uptake of water vapor by MS3A at a partial pressure of 1.94 kPa and a temperature of 353 K.**

By performing a series of optimizations for all kinetic uptake curves from Syracuse, we can determine the optimum values of the corrected diffusivity terms ( $D_o$ ) from the Darken expression (Equation 59). Figure 43 below shows the optimized  $D_o$  parameter results from the optimizations. From these numerical experiments, we can clearly observe some relationship between  $D_o$  and temperature and pressure.

In theory, there is an exponential relationship between the corrected diffusion term ( $D_o$ ) and temperature (Sedláček, 1974), which follows an Arrhenius type rate expression (Equation 60). However, from Figure 43, it is clear that there is also a strong relationship between this diffusivity and the vapor pressure in the gas phase ( $p$ ). This relationship with pressure is roughly linear on a log-log scale, so we developed an equation that could capture this information (Equation 61). Combining Equations 60 and 61 yields a semi-empirical expression that can be used to describe the relationship between the corrected diffusion term with temperature and pressure. The parameters of the model below are the activation energy of adsorption ( $E$ ), reference diffusivity ( $D_{ref}$ ), reference temperature ( $T_{ref}$ ), and an affinity constant ( $B$ ).

$$D_o = D_\infty \exp\left(-\frac{E}{RT}\right) \quad (60)$$

$$D_\infty = D_{ref} \frac{p^{(T_{ref}/T)}}{p^B} \quad (61)$$

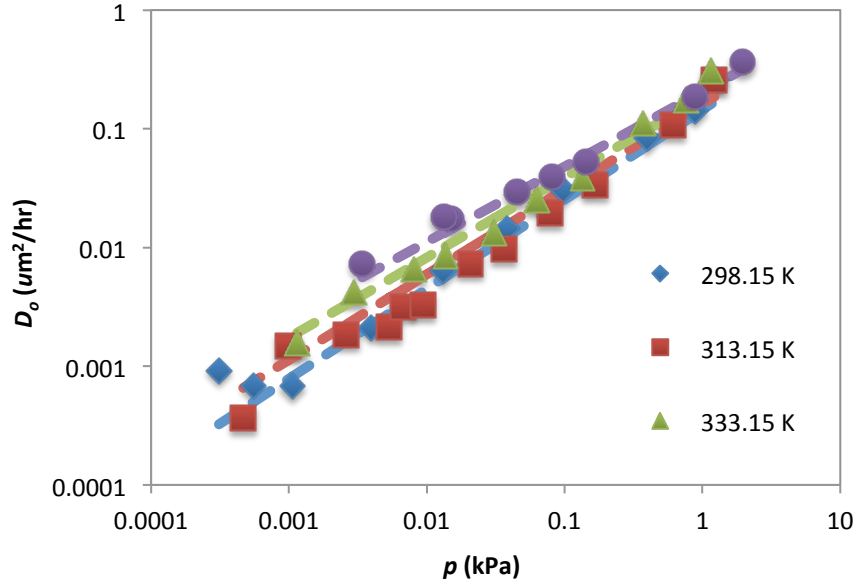


**Figure 41. Optimized corrected diffusivity from using the Darken model for crystal diffusion in the SKUA optimization routine. The dashed lines represent a semi-empirical model (Equations 60 and 61) used to describe how this corrected diffusion term varies with temperature and partial pressure.**

The optimized parameters, from Equations 60 and 61, used to describe the Syracuse uptake data are outlined below in Table 11. Using these parameters obtained from the uptake curves, we then successfully predicted the cycling behavior of the adsorbent observed in Syracuse University experiments. Results from that simulation can be viewed in Figure 44 below. In general, the model prediction from SKUA agrees very well with the experimentally obtained data. This helps to validate the modeling approach we have taken and demonstrates our capacity to accurately describe and predict both adsorption and desorption observed experimentally.

**Table 11. Optimized parameters for water vapor uptake by MS3A**

Parameter	Value	Units
$D_{ref}$	1.416	$\mu\text{m}^2/\text{hr}$
$T_{ref}$	230.310	K
$B$	0.017	-
$E$	5657.178	J/mol

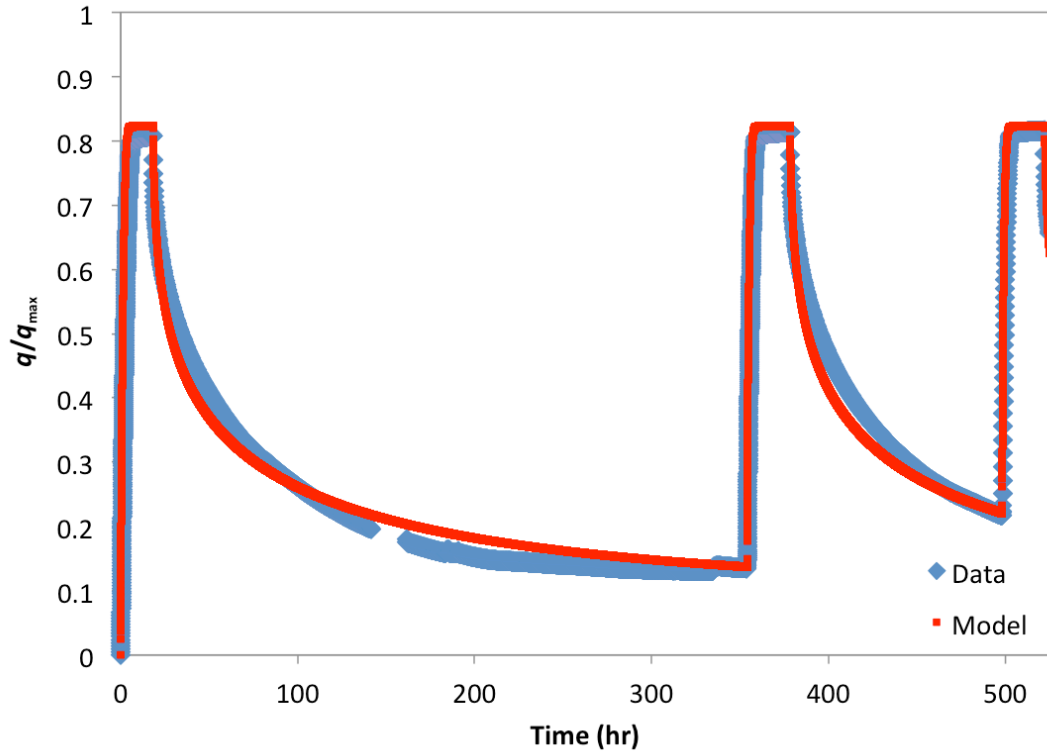


**Figure 42. SKUA prediction of the cycling behavior of MS3A and water vapor at 40 oC and a water vapor pressure of 0.337 kPa. The simulation assumes a step drop in water vapor pressure, down to the minimum dew point, at the start of each desorption cycle. Model predictions, shown in red, match very well with experimental data, collected at Syracuse, shown in blue.**

In order to consider these more complex diffusion mechanisms in optimization, we had to develop an optimization scheme around our numerical simulation of the diffusion kinetics. This approach allows us to consider all possible mechanisms within our system, as well as the possibility of a variable diffusivity. Figure 45 below shows a schematic of the type of scheme that we have developed for this purpose. The routine starts by giving an initial guess to the parameters of the model, and proceeds by running a simulation with those parameters. Results from the simulation are then compared against the actual data to form a residual, which is then fed into the actual non-linear optimization routine to determine by how much, and in what direction, to change the values of the parameters. With those new parameters, the simulation is rerun and the cycle continues until a suitable level of convergence is achieved. For simplicity, we decided to continue to use the Levenburg-Marquardt's algorithm (Wuttke, 2013), which is utilized by both the equilibria kernels discussed earlier.

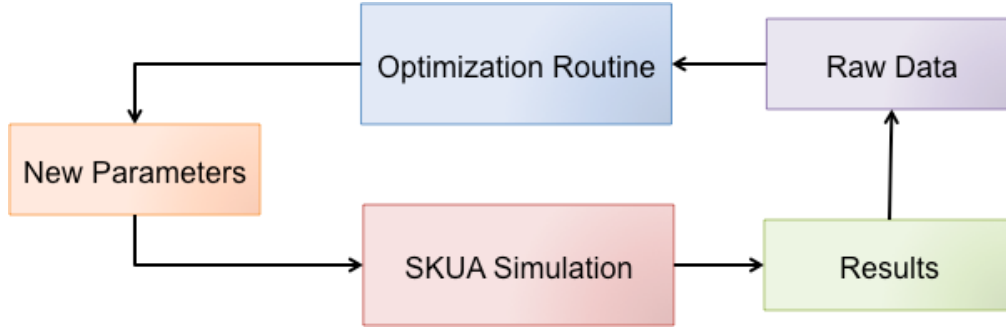


**Figure 43. Schematic of the routine developed to optimize for the unknown parameters within the SKUA model. This routine will allow us to consider any mechanism, which we think may be limiting the uptake rate, including the consideration of a variable diffusivity.**

## 2.7 Transport Modeling

### 2.7.1 OSPREY and the MOOSE Framework

The original OSPREY model, developed at INL (Rutledge, 2013), was built on top of the Multiphysics Object-Oriented Simulation Environment (MOOSE), which was also developed at INL (Gaston et al., 2009). This MOOSE framework has a modular based architecture by which engineers can build physics simulations by putting together multiple kernels into a residual calculation. MOOSE then constructs a non-linear system of equations from those residuals and proceeds to iteratively solve the problem at each time step.

#### 2.7.1.1 Issues with Advection-Diffusion Problems

Physics in MOOSE are discretized using a finite element method, wherein the PDE governing the problem is multiplied by a shape function ( $\psi$ ), then broken down into a series of kernels and boundary conditions using Gauss divergence theorem (Gaston et al., 2009). Equations 62 and 63 demonstrate how to discretize a simple parabolic equation (i.e. time-dependent diffusion) to fit it into the MOOSE framework. This type of finite element discretization is the default methodology used within MOOSE and is referred to as the Galerkin method.

$$\frac{\partial u}{\partial t} = \nabla \cdot (\nabla u) \quad (62)$$

$$\underbrace{(\dot{u}, \psi)}_{\text{kernel}} + \underbrace{(\nabla u, \nabla \psi)}_{\text{kernel}} - \underbrace{\langle \nabla u \cdot \vec{n}, \psi \rangle}_{BC} = 0 \quad (63)$$

In the first version of OSPREY, the standard Galerkin methods employed by MOOSE worked very well to describe the physics. Figure 46 shows the preliminary OSPREY results compared against a similar model (gPROMS) and experimental column breakthrough data for krypton collected at INL (Rutledge, 2013). These initial results were a large motivation behind wanting to continue modeling within the MOOSE framework.

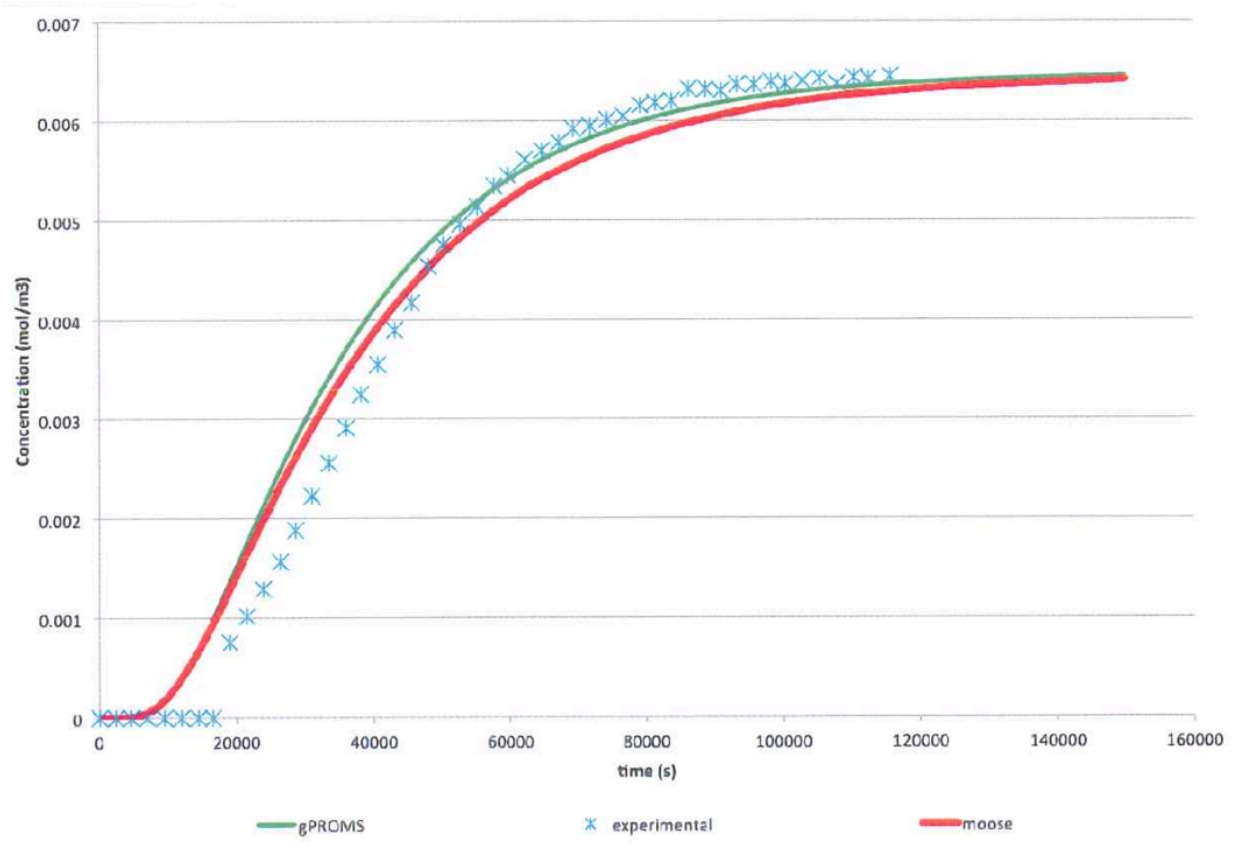


**Figure 44. Comparison between OSPREY, gPROMS, and INL data as reported by Rutledge (2013). Preliminary transport modeling at INL showed much promise for future development.**

Unfortunately, when we attempted to use the standard Galerkin methods for advectively dominant transport equations, we began to observe a significant amount of false diffusion, or even oscillations around sharp wave boundaries. Figure 47 demonstrates this point for a simple linear advection-diffusion transport equation in one-dimension. For this simple problem, there exists an analytical solution (Kumar et al., 2009) we can use to compare the numerical MOOSE results against as a validation step. The results in Figure 47 were generated from MOOSE using the standard Galerkin approach with a first order implicit time step (Implicit) and a second order implicit time step (BDF2). From these results, we can clearly see that using the standard Galerkin approach in MOOSE is unsatisfactory for simulating the types of physics we expect to see in the transport model for gas adsorption in a fixed-bed column.

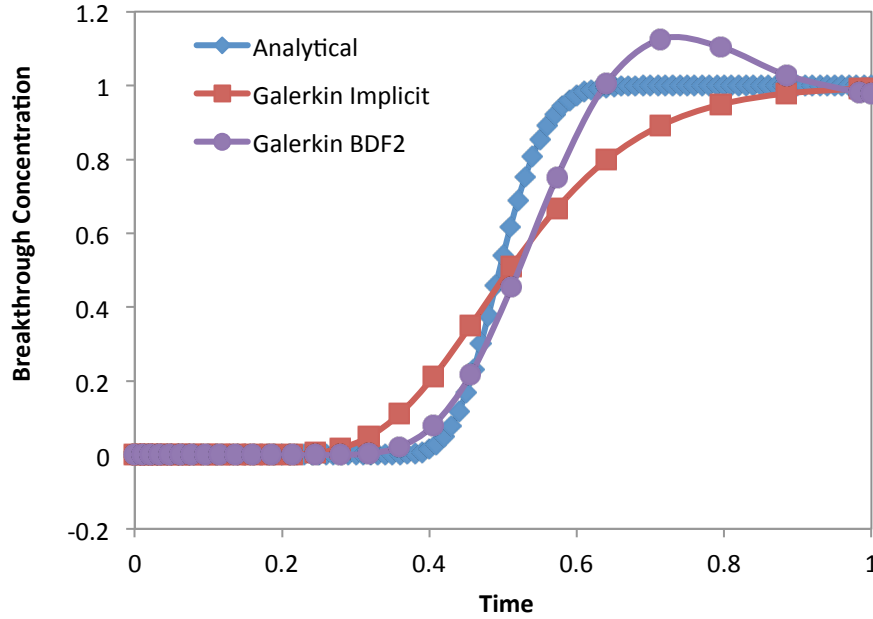


**Figure 45. MOOSE results when solving a linear advection-diffusion transport equation using the standard Galerkin approach. The implicit time step introduced false diffusion while the BDF2 time step forced oscillations to occur around the wave boundary.**

As it turns out, these types of issues commonly arise when trying to use Galerkin methods to model advection dominant processes or other flow/transport physics (Zienkiewicz and Taylor, 2000). Therefore, we should not use the standard MOOSE methods to model the transport equations. Instead, we could use a conservative class of finite elements called Discontinuous Galerkin (DG) methods (Rivière, 2008). MOOSE does support the use of DG methods, but the development of the MOOSE kernels for this type of problem is significantly more difficult.

DG methods involve the reconstruction of cell fluxes based on an upwind approach, whereby the fluxes into and out of a particular cell in the mesh is determined by the current cell being operated on and the neighboring cell that lies just upwind (Figure 48). By constructing the finite element method in this way, conservation of the conserved quantity  $u$  is ensured, as the overflow from one cell would become the inflow to the next cell.

To see this approach mathematically, consider the following advection diffusion problem in Equation 64. Notice here that the advective velocity ( $v$ ) is not moved out from under the differential operator, as it is usually represented in MOOSE. Instead, the equation is left in its conservative form before applying the Gauss divergence theorem. As a result, we will acquire a new boundary condition from the advective term after obtaining the weak form (Rivière, 2008).

$$\frac{\partial u}{\partial t} + \nabla \cdot (vu) = \nabla \cdot (D\nabla u) \quad (64)$$

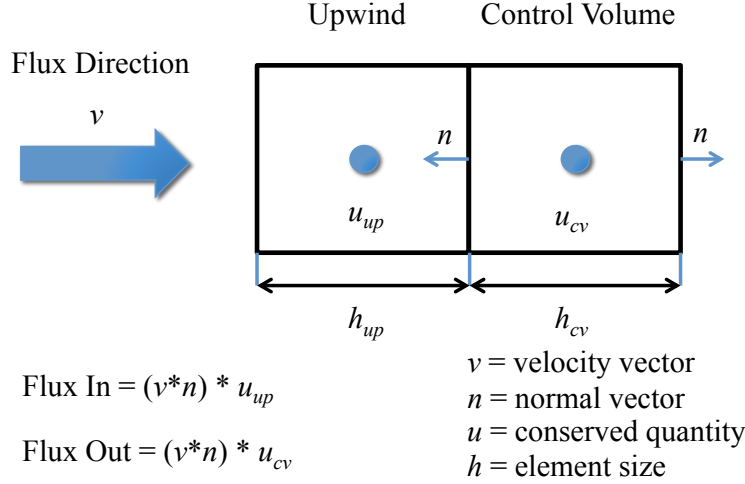


**Figure 46. Visualization of an upwind DG method for finite elements.**

From Equation 64, we seek to formulate a weak form based on the DG approach. First, the bilinear form for the discretization of the diffusion term is formulated (Equation 65), but this time it will contain two additional parameters ( $\varepsilon$  and  $\sigma$ ), as well as the mesh size ( $h$ ), which are used to penalize the jumps in discontinuity between interior cells (Rivière, 2008). The advection term will be discretized using the upwind approach shown in Figure 48 and have the bilinear form shown in Equations 66 and 67 (Rivière, 2008).

$$a(u, \psi) = \int D \nabla u \cdot \nabla \psi + \frac{\sigma}{h} \int u \cdot \psi - \int \{D \nabla u \cdot \vec{n}\} \cdot \psi + \varepsilon \int \{D \nabla \psi \cdot \vec{n}\} \cdot u \quad (65)$$

$$u^* = \begin{cases} u_{cv} & v \cdot \vec{n} \geq 0 \\ u_{up} & v \cdot \vec{n} < 0 \end{cases} \quad (66)$$

$$b(u, \psi) = \int (v \cdot \vec{n}) \cdot u^* \cdot \psi - \int (vu) \cdot \nabla \psi + \int (v \cdot \vec{n}) \cdot u \cdot \psi \quad (67)$$

Combining these bilinear forms into residuals within MOOSE creates a method that is conservative for the variable  $u$  (Equation 68). The input and output boundary conditions for the domain are based on the edge fluxes constructed by the DG method. Because of how these boundary conditions are formed, it is possible to place both input and output boundary conditions within the same kernel, so long as care is taken in determining which boundary is currently being acted on. This is the formulation of the problem that would form the basis for solving conservation laws in MOOSE.

$$\underbrace{(\dot{u}, \psi) + a(u, \psi) + b(u, \psi)}_{\text{kernels}} - \underbrace{\langle D \nabla u \cdot \vec{n}, \psi \rangle}_{\text{output}} + \underbrace{\langle (v \cdot \vec{n}) \cdot u, \psi \rangle + \langle (vu - D \nabla u) \cdot \vec{n}, \psi \rangle}_{\text{input}} = 0 \quad (68)$$

Currently, a new set of OSPREY kernels are being developed at GIT for the use of DG finite elements. However, progress on these DG-OSPREY kernels has been relatively slow due to the limited support within the MOOSE framework for implementation of DG methods. One major limitation is the lack of *slope limiting* available in the MOOSE framework. Recall from

section 4.3 that the FINCH kernel employs this type of method to create a high-resolution numerical scheme. Without a slope limiting implementation in MOOSE, the DG method described above is only first order accurate, and is therefore a low-resolution scheme.

### **2.7.1.2 Initial User Evaluation of OSPREY**

During the summer of 2014, this project interacted with Sigma Team researchers in evaluating the current development of OSPREY as a tool for engineering users. An undergraduate student from Syracuse University spent a semester at ORNL. The student acted as a new user of OSPREY, going through the steps to become a user and installing the MOOSE system on a computer. During this process, considerable help was needed, from INL MOOSE support personnel and from Georgia Tech in troubleshooting the operation of OSPREY.

Runs were made attempting to simulate the uptake of water vapor by MS3A, comparing predicted breakthrough curves to results previously obtained in the deep bed hydration tests conducted at ORNL. Two OSPREY input files were used for the water-MS3A system: the generalized statistical thermodynamic adsorption (GSTA) kernel developed in this project, and the original single-component input file, using Langmuir parameters estimated from a fit of isotherm data published by the sorbent manufacturer. Input variables were either known from experimental conditions or estimated from the literature (e.g., thermal conductivity of sorbent). Mass transfer coefficients were averaged over time, based on values estimated from experiments conducted in this project at Syracuse University.

The simulations did not match well with laboratory tests. Predicted breakthrough time for the Langmuir model was significantly greater than the experimental value; in that case, it appears that there may have been an error in isotherm parameters used by the student. Agreement was better using the GSTA isotherm; however, the predicted breakthrough curve was significantly broader than the experimental results. Variation of input mass transfer coefficient had little impact on the result. In this case, it appears there may be some issue in prediction of axial dispersion.

The exercise indicated that there is opportunity for improvement both in the capability of the current modeling tool and in the guidance for engineering users. In addition to a user's manual with test cases, recommended improvements include: greater flexibility for input of mass transfer parameters, capability for user-defined, time-variable gas inlet concentrations, and greater options for output of results. Further information on this may be found in FCR&D report FCRD-SWF-2014-000459.

### **2.7.2. FALCON**

FALCON was meant to be a competitor for OSPREY in modeling the same transport equations for the fixed-bed adsorption problem. In both cases, the transport equations were assumed to exist in a one-dimension, observing the axial direction of the column. Mass balances for each gas species (Equation 69) would be coupled with the energy balance (Equation 70) and contain the following parameters:  $\varepsilon_b$  is the bed porosity,  $C_i$  is the concentration of the  $i^{\text{th}}$  species in the bed,  $v$  is the superficial velocity of the gas,  $D_z$  is the axial dispersion of the gas,  $\rho_b$  is the bed packing density,  $q_i$  is the average amount adsorbed for the  $i^{\text{th}}$  species,  $h_g$  is the heat capacity



of the gas phase,  $\rho$  is the gas density,  $h_s$  is the solid heat capacity,  $T$  is the temperature in the column,  $K_z$  is the axial thermal conductivity,  $q_T$  is the total amount adsorbed,  $Q_{st}$  is the heat of adsorption,  $U_w$  is the bed-wall heat transfer coefficient,  $d_{in}$  is the inner wall diameter, and  $T_w$  is the wall temperature.

$$\varepsilon_b \frac{\partial C_i}{\partial t} + \frac{\partial}{\partial z}(\varepsilon_b v C_i) = \frac{\partial}{\partial z} \left( \varepsilon_b D_z \frac{\partial C_i}{\partial z} \right) - \rho_b \frac{\partial q_i}{\partial t} \quad (69)$$

$$(h_g \rho \varepsilon_b + h_s \rho_b) \frac{\partial T}{\partial t} + \frac{\partial}{\partial z} (h_g \rho \varepsilon_b v T) = \frac{\partial}{\partial z} \left( \varepsilon_b K_z \frac{\partial T}{\partial z} \right) + \rho_b \frac{\partial (Q_{st} q_T)}{\partial T} + \frac{4U_w}{d_{in}} (T_w - T) \quad (70)$$

The difference between FALCON and OSPREY is in the approach to modeling the physics of this system. OSPREY was built on top of MOOSE, as discussed above, which had its own advantages and disadvantages. However, the plan for FALCON was to model the system using the FINCH framework discussed in section 4.3. Recall that the FINCH system used conservative finite differences with slope limiting to handle the advectively dominant physics. This methodology is actually superior to the MOOSE method for solving the 1-D advectively dominant transport equation (Figure 49), which was the primary motivation behind transitioning to this type of modeling.

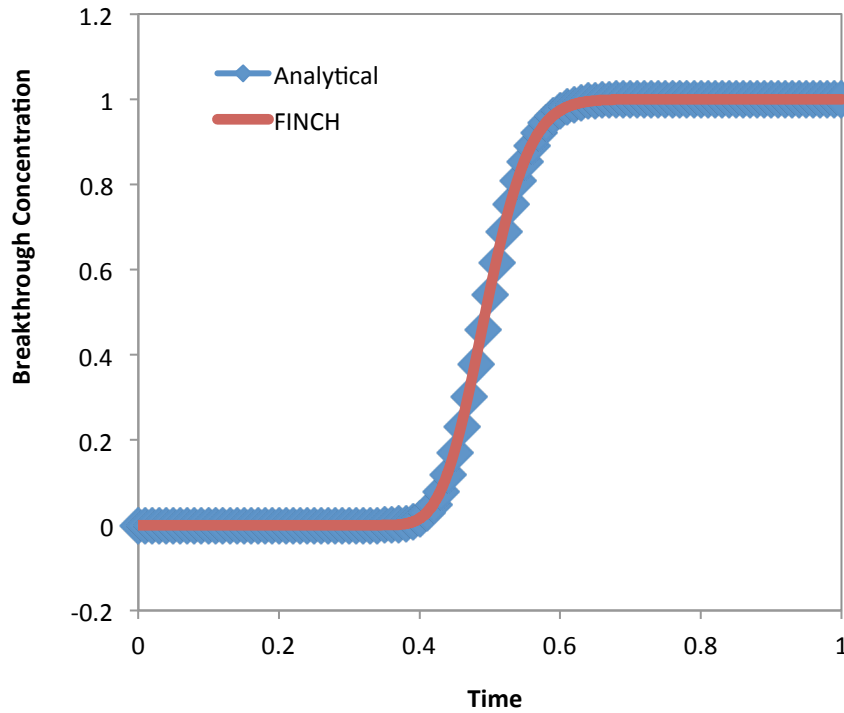


**Figure 47. FINCH results for modeling the same 1-D linear advection-diffusion transport problem from Figure 47. Results from FINCH significantly outperform MOOSE at describing this physical process.**

## 2.8 User Requirements and Documentation

For all the GIT developed kernels, there are no hardware requirements since the tools developed exist strictly as source code. The only requirements necessary would therefore be some form of C/C++ compiler to build a binary (executable file) from that source code. Currently, the source code has been successfully compiled and run using the gcc 4.2 (or newer) as well as the LLVM compiler available in Xcode 4.6 (or newer) for Macintosh computers. However, it is possible to build and run these codes on any platform with a supported C/C++ compiler.

To use OSPREY, DG-OSPREY, or MOOSE will require either a Linux or Macintosh computer, as MOOSE compilers do not support a Windows operating system. For more information on how to set up a computer to run and compile MOOSE applications, visit <http://mooseframework.org/>. This reference has detailed information on how to get started using MOOSE and some common problems with getting MOOSE to work on most computers.

OSPREY is not currently available as an open-source project, but MOOSE users can already gain access to the DG-OSPREY working directory, which is available on GitHub at <https://github.com/aladshaw3/dgosprey>. To get started using DG-OSPREY, one will first have to follow the “Getting Started” instructions found on the MOOSE framework URL above. After MOOSE has been successfully installed and tested, one can then clone the DG-OSPREY working files onto the desktop by opening up a terminal window, changing directories to the folder containing the “moose” folder, and typing “git clone https://github.com/aladshaw3/dgosprey.git” into the terminal.

After the DG-OSPREY files have downloaded and while still in a terminal window, it is necessary to change directories into the folder named “dgosprey” and type the “make” command into the terminal. If the build did not produce an error, then type “./run\_tests” in the terminal to confirm that DG-OSPREY was compiled correctly and that all its test cases passed. From this point on you are ready to start using DG-OSPREY. However, as it is still under development, there is no guarantee that it will always run properly. To keep DG-OSPREY up-to-date, you will need to use the “git pull” command from within the “dgosprey” directory whenever an update is needed.

Currently, since this is still an ongoing project, there is no official user documentation available for any of the kernels discussed above. However, a user manual is planned and being developed to cover all members of the FLOCK discussed in sections 4 through 7 above. Once that manual is complete, it will be made available to all users of the models being developed.

## 2.9 Conclusions and Path Forward

The tools developed under this project are widely varied and applicable to many different adsorption systems beyond just the gases and adsorbents we are interested in here. We have demonstrated that our equilibria kernels for gas-solid adsorption are very robust and flexible enough to be useful for analyzing large sets of adsorption data, including those reported in literature (Figures 35 through 37). Combining the data gathered in this project at Syracuse University with data available in literature, we were able to validate our single-component

equilibria kernels. Additionally, utilizing the literature data we were also able to validate our multi-component equilibria theory and models for real mixed-gas systems (Figures 39 and 40).

Adsorption kinetic uptake kernels were based mostly on theory available in literature (Equations 38 through 60), but were validated using the Syracuse-collected data (Figure 42). We also developed a methodology by which we could determine the unknown surface diffusivities when supplied with uptake data. Using those optimum parameters, we were successful in accurately predicting the cycling behavior of the system observed by Syracuse (Figure 44).

While the transport modeling is still in progress, we were at least able to identify the causes of the problems (Figure 47). Additionally, having identified the problems with the transport model, we are now in a position to take the necessary corrective steps to improve those models. Once we have a good transport-modeling framework to build off from, we will start again to couple the kinetic and equilibria kernels into the transport model, as indicated in Figure 30.

As part of the effort to develop a stronger modeling platform, we also developed the basic PDE kernels discussed in section 4. These are a general set of algorithms and routines that can be used to robustly solve systems of equations that arise from physical phenomena, including chemical transport and adsorption. Using these newly developed kernels, we plan to revisit the kinetic models to develop a more robust and efficient set of codes. Additionally, we can use these PDE kernels as a platform for building a new 2-D version of FINCH if the DG kernels in MOOSE do not work as expected. Therefore, this more generic set of kernels will serve as a starting point for future modeling needs within this program.

## **ABSORPTION**

### **3. CO<sub>2</sub> absorption modeling**

#### **3.1 Key personnel**

Jorge Gabitto (Co-PI), Prairie View A&M University

#### **3.2 Scope**

The absorption of carbon dioxide is an important process in many practical applications such as, reduction of greenhouse gases, several processes in the chemical and petroleum industries, captured of radioactive isotopes in the nuclear cycle, etc. The goal of this research process is to develop a dynamic model to simulate CO<sub>2</sub> absorption by using high alkaline content water solutions. The model is based upon transient mass and energy balances for the chemical species commonly present in CO<sub>2</sub> gas-liquid absorption. A computer code has been written to implement the proposed model. An experimental program has been also carried out as part of this project. The experimental program determined values of liquid phase mass transfer coefficients with and without chemical reactions. The model has been implemented into a computer code capable of simulating complex transient absorption processes. The influence of geometric parameters and operating variables has been studied using the proposed model.

#### **3.3 Task and Description of major milestones:**

The main task of this part of the project was to develop a dynamic absorption model for CO<sub>2</sub> based on current literature. The effort in Year 1 was focused on extending the literature search, working on model development and writing computer codes, and preparing and calibrating the experimental setup. Work in Year 2 was focused on computer code development, generation of numerical results, and collection and processing of experimental data. Year 3 included generation of numerical results based on model development, completion and processing of experimental data, model validation, conclusions, and preparation of the Final Report.

This Final Report completes all milestones and deliverables required for this part of the project.

### 3.4 Technical Description

#### 3.4.1 Dynamic Model

##### 3.4.1.1 Mass Transfer

Gas absorption with chemical reaction is widely used in the chemical and petroleum industries. The removal of CO<sub>2</sub> from flue gases in coal-fired power plants is also an important technology to mitigate greenhouse gas emissions and meet environmental regulations. One of the well-known technological alternatives for CO<sub>2</sub> capture is absorption/stripping with aqueous solvents such as alkanolamines and their blends.<sup>1</sup>

We follow in this project an approach similar to the one used by Greer et al.<sup>2,3,4</sup> in the dynamic simulation of the absorption/desorption of carbon dioxide from monoethanolamine. A dynamic model for the absorption process has been developed using a concentrated sodium hydroxide solution (pH>10) to increase the absorption rate. Henry's law was used for modeling the vapor phase equilibrium of CO<sub>2</sub>. The Henry's constant values for the different gas phase species is calculated using fugacity ratios obtained by the Peng-Robinson equation of state (EOS). Chemical reactions between CO<sub>2</sub> and the high pH solution are included in the model along with the enhancement factor for chemical absorption. Liquid and vapor energy balances were developed to calculate the liquid and vapor temperature, respectively. A schematic of the column is shown in Figure 50.

The model of the absorption tower is developed by taking a small slice of the tower of height dz. The height of the packing goes from z=0 and to z=H, where H is the packing height. The components in the gas phase are CO<sub>2</sub>, H<sub>2</sub>O, N<sub>2</sub>, and O<sub>2</sub> while the species considered in the liquid phase are CO<sub>2</sub>, H<sub>2</sub>O, N<sub>2</sub>, O<sub>2</sub>, CO<sub>3</sub><sup>=</sup>, OH<sup>-</sup> and H<sub>3</sub>O<sup>+</sup>.

We carry out mass balances for the gas and liquid phases in the control volume of height dz and area A<sub>s</sub>.

In general form, the liquid mass balance is given by:

$$\frac{dC_i^l}{dt} = \dot{N}_{in} - \dot{N}_{out} - \dot{N}_{diff} + \dot{N}_{gen}. \quad (1)$$

where  $C_i^l$  is the molar concentration of species i in the liquid phase,  $\dot{N}_i$  terms refer to the input, output, diffusional and generation molar flows, respectively.

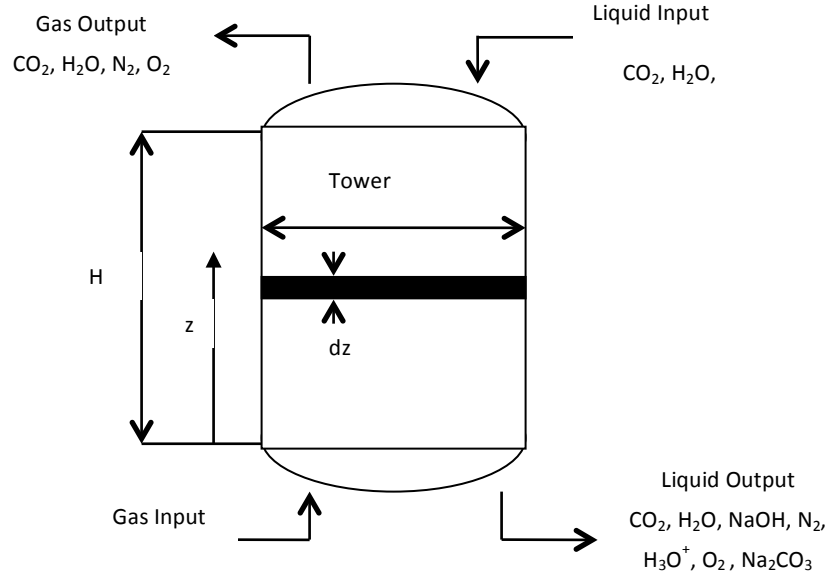


**Figure 48. Absorption tower used for carbon dioxide absorption.**

After algebraic manipulation, eqn. (1) becomes:

$$\frac{\partial C_i^l}{\partial t} = u \frac{\partial C_i^l}{\partial z} - \dot{N}_{\text{diff}} + R_{i,\text{gen}} \quad (2)$$

the  $R_{i,\text{gen}}$  term represents moles of species  $i$  generated/consumed by interphase reaction per unit volume.

A similar equation can be derived for the vapor phase:

$$\frac{\partial C_i^v}{\partial t} = -u \frac{\partial C_i^v}{\partial z} + \dot{N}_{\text{diff}} \quad (3)$$

Here, the fact that the reaction takes place on the liquid side of the interphase has been used. The diffusion driven flows are reversed as they move from one phase to the other.

The mass flux of component  $i$  ( $\dot{N}_{\text{diff}}$ ) is calculated using:

$$\dot{N}_{\text{diff}} = k_l a_w (C_i^b - C_i^*) \quad (4)$$

where  $k_l$  is the liquid side mass transfer coefficient,  $a_w$  is the interphase surface area per unit volume,  $C_i^b$  is the liquid bulk concentration and  $C_i^*$  is the interfacial liquid equilibrium concentration.

The mass flux of  $\text{CO}_2$  ( $\dot{N}_{\text{CO}_2}$ ) needs to be dealt separately as this component participates in a complex chemical reaction<sup>2, 6-10</sup>; however, in strong hydroxide solutions the overall reaction is given by:



In the case of high pH value and low  $\text{CO}_2$  concentrations, eqn. (5) can be treated as a pseudo first order reaction<sup>6-10</sup>:

$$-r_{\text{CO}_2} = k_R [\text{CO}_2] [\text{OH}^-] \quad (6)$$

Here,  $k_R$  is the specific reaction rate constant for the pseudo first order reaction.

The carbon dioxide absorption is accompanied by a strong chemical reaction. Therefore, the calculation of the  $\text{CO}_2$  flux term requires the use of an enhancement factor (E) to account for the enhanced mass transfer. The enhancement factor is defined as the mass transfer rate under absorptive reaction divided by the mass transfer rate under non-reactive absorption conditions<sup>11</sup>. The  $\text{CO}_2$  molar flux term ( $\dot{N}_{\text{CO}_2}$ ) is given by<sup>2-5</sup>:

$$\dot{N}_{\text{CO}_2} = -k_{l,\text{CO}_2} E a_w H^{\text{cc}} C_{\text{CO}_2}^g \quad (7)$$

Here,  $H^{\text{cc}}$  ( $H^{\text{cc}} = C_i^l / C_i^g$ ) is the concentration based Henry's constant, the enhancement factor (E) is given by the Hatta number defined as:

$$\text{HA} = \frac{\sqrt{k_R D_{\text{CO}_2} C_{\text{OH}^-}}}{k_l} = E \quad (8)$$

Here,  $D_{\text{CO}_2}$  is the diffusion coefficient, and  $k_l$  is the liquid layer mass transfer coefficient. The influence of the reaction on the total rate of  $\text{CO}_2$  absorption is considered by the enhancement factor E. In the case of  $\text{Ha} > 2$  the enhancement factor E is equal to the HA number. E is also proportional to the square root of the hydroxyl ion concentration.

In our formulation, it was assumed that for the vapor phase components the mass transfer resistance on the liquid thin layer is much bigger than the mass transfer resistance on the gas side<sup>2,3</sup>. In the case of water the reverse assumption was used, i.e., the mass transfer resistance on the vapor side is the biggest one. Figure 51 reflects these assumptions and it depicts the different concentrations used in the different balance equations.

For  $\text{CO}_2$ , however, in the case of very high pH solutions the assumption of mass transfer controlled by the liquid phase can break down. In this case, we used a formulation replacing the liquid phase mass transfer coefficient ( $k_l$ ) by a global mass transfer coefficient ( $K_{\text{OL}}$ ). This global mass transfer coefficient depends upon the enhancement factor and is calculated by:

$$\frac{1}{K_{OL}} = \frac{H_{cc}}{k_g} + \frac{1}{k_l E} \quad (9)$$

In order to compare transient and steady-state behavior for all chemical species we developed steady-state versions of eqs. (2) and (3).

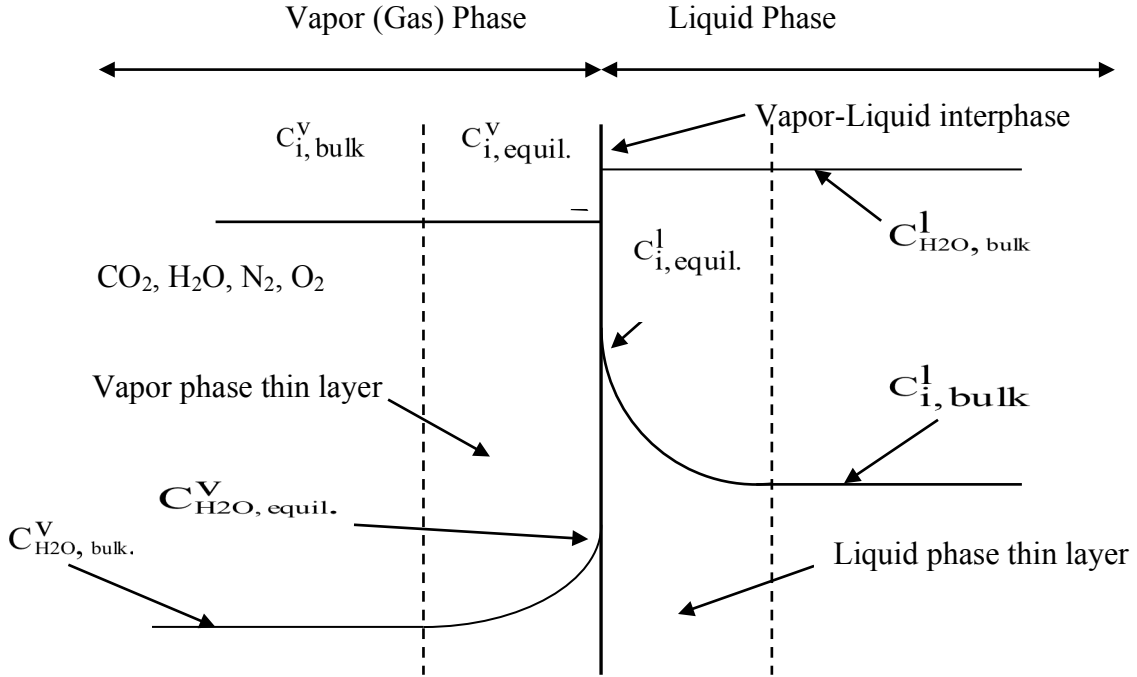


**Figure 49. Concentration gradients at vapor-liquid interphase.**

### 3.4.1.2 Heat Transfer

The reaction given by eq. (5) is highly exothermic; therefore, an energy balance has to be solved in order to consider temperature changes. A two equation model for the transient energy balance in the control volume depicted in Figure 50 leads to the following equations for all the components shown in Figure 51<sup>2, 3, 5</sup>:

$$\frac{\partial T^l}{\partial t} = -u_l \frac{\partial T^l}{\partial z} - \dot{N}_{CO_2} \Delta H_R / \sum_i C_i^l C_{pi}^l - U_T a_w (T^l - T^v) / \sum_i C_i^l C_{pi}^l \quad (10)$$

$$\frac{\partial T^v}{\partial t} = -u_v \frac{\partial T^v}{\partial z} + U_T a_w (T^l - T^v) / \sum_i C_i^v C_{pi}^v \quad (11)$$



Here,  $C_{pi}^v$  and  $C_{pi}^l$  are the heat capacities of component  $i$  in the mixture,  $U_T$  is the global heat transfer coefficient,  $\Delta H^{vl}$  is the latent heat for the change of phase,  $u_l$  and  $u_v$ , are the convective velocities inside the liquid and vapor phases, and  $\Delta H_R$  is the heat released by the chemical reaction.

The  $CO_2$  molar flux term ( $\dot{N}_{CO_2}$ ) is given by eqn. (7) while the enhancement factor ( $E$ ) is given by the Hatta number defined in eqn. (8).

### 3.4.1.3 Vapor-Liquid Equilibrium

The development of a vapor equilibrium model is necessary to evaluate the diffusion molar flows. A general expression for the vapor-liquid equilibrium is given by:

$$P_T \phi_i^v y_i = P_v^0 \phi_i^l x_i \quad (12)$$

Here,  $P_T$  is the system total pressure;  $P_v^0$  is the pure component vapor pressure,  $y_i$  and  $x_i$ , are the gas and liquid molar fractions;  $\phi_i^l$  and  $\phi_i^v$  are the gas and liquid fugacity coefficients, respectively.

The fugacity coefficients can be calculated using different thermodynamic models<sup>12</sup>. A preliminary approximation is to consider fugacity coefficients equal to one (ideal model). This approximation represents Raoult's law. Another approach is to handle interfacial gas-liquid equilibrium by using Henry's law:

$$y_i = H x_i = \frac{P_v^0 \phi_i^l}{P_T \phi_i^v} x_i \quad (13)$$

Here,  $H$  is the Henry's constant.

The Virial equation of state<sup>13</sup> was used to calculate fugacity coefficients for the gas phase  $\phi_i^v$ . The Tsonopoulos equations were used to estimate the cross coefficients and second Virial coefficients of the gas mixture<sup>14</sup>.

The UNIQUAC (Universal Quasi Chemical) group contribution model was used to calculate the activity coefficients in liquid phase<sup>15</sup>. In any group-contribution method, the basic idea is that whereas there are many chemical compounds of interest in chemical technology, the number of functional groups that constitute these compounds is much smaller. Therefore, if we assume that a physical property of a fluid is the sum of contributions made by the molecule's functional groups, we can correlate the properties of a very large number of fluids in terms of a much smaller number of parameters that characterize the contributions of individual groups<sup>15</sup> (Poling et al., 2001). The method requires the values of the UNIQUAC parameters,  $r_i$  and  $q_i$ , for component  $i$  plus binary interaction parameters. The interaction parameters are calculated by fitting experimental data. The technique allows calculation of multicomponent equilibria using only binary interaction parameters<sup>15</sup>. The method was implemented using the computational approach reported by Prausnitz et al., 1980<sup>12</sup>. Three databases compiling thermodynamic

information for physical property calculations, interaction parameters and other required information were prepared. The physical properties database includes data for 84 components.

In Table 12, some typical vapor-liquid results are shown for a mixture of CO<sub>2</sub>-N<sub>2</sub>-O<sub>2</sub>. In the table,  $\gamma_i$ ,  $\phi_i$  represent the activity and fugacity coefficients of component i, respectively. The results show the equilibrium composition of the first condensing drop (dew point). The liquid phase behaves in an ideal way. The  $K_i$  values are the modified Henry's law constant values calculated using molar fractions. Results for the H<sub>2</sub>O- CO<sub>2</sub>-N<sub>2</sub>-O<sub>2</sub> system are also shown. In this case the composition of the first bubble evaporating at equilibrium is shown. Both phases show real behavior with the liquid phase being the one farther apart from an ideal mixture. The accuracy of the results is tied to the presence of experimental information about these mixtures. This information is used to determine interaction coefficients. These results show the difficulty associated with this kind of calculations. An alternative approach would be the use of experimentally determined  $K_i$  constant values.

**Table 12. Typical vapor-liquid equilibrium results.**

Component	$y_i$	$x_i$	$\gamma_i$	$\phi_i$	$K_i$
O <sub>2</sub>	0.170	0.955	0.922	1.000	0.178
N <sub>2</sub>	0.789	.0013	0.778	1.000	61.186
CO <sub>2</sub>	0.040	0.032	0.889	1.000	1.238
T <sub>Dew</sub> =	299.2 K		P=	P=101.3 kPa	
H <sub>2</sub> O	0.469	0.970	0.565	0.743	0.478
O <sub>2</sub>	0.032	0.010	0.852	0.934	3.233
N <sub>2</sub>	0.367	.0010	0.434	0.956	37.720
CO <sub>2</sub>	0.137	0.010	0.675	0.898	13.670
T <sub>bubble</sub> =	353.6 K		P=	P=101.3 kPa	

The interfacial gas-liquid equilibrium can also be determined by using Henry's law values experimentally or empirically calculated. The most common equations available are:

$$H^{cp} \equiv c_i^l / p_i^v \quad (14)$$

Here,  $H^{cp}$  is the dimensional Henry's constant using concentrations and pressure units,  $c_i^l$  is the concentration of a species in the aqueous phase and  $p_i^v$  is the partial pressure of that species in the gas phase.

$$H^{cc} \equiv c_i^l / c_i^v = H^{cp} R T \quad (15)$$

Here,  $H^{cc}$  is the dimensionless Henry's constant,  $c_i^v$  is the concentration of species i in the gas phase.

This second approach is attractive because is much less computer intensive; however, it can lead to inaccurate results, especially for multicomponent mixtures comprising polar and non-polar components. In this work we decided to try both approaches and pick the second one if there are no significant differences in the results. At the same time we were able to get a good source of equilibrium data<sup>16</sup>. This source even includes procedures to correct the values of Henry's constants by taking into account changes in temperatures and pressures.

#### 3.4.1.4 Parameter Determination

A successful computer code requires the computation of a lot of supporting information such as, mass and heat transfer coefficients, specific heat values for multicomponent mixtures, enhancement factors (Hata number dependent), diffusivity coefficients, and several physical properties. Several correlations were implemented in order to calculate operating and transport parameters<sup>3</sup>. Liquid phase mass transfer coefficients were calculated by:

$$k_l^i = C_l \left( \frac{\rho_l g}{\mu_l} \right)^{1/6} \left( \frac{a_t D_l^i}{4 \varepsilon} \right)^{1/2} \left( \frac{u_l}{a_t} \right)^{1/3} \quad (16)$$

Liquid-phase mass transfer coefficients are used for O<sub>2</sub>, N<sub>2</sub> and CO<sub>2</sub>. Here, C<sub>l</sub>, is the packing constant for liquid phase; a<sub>t</sub>, is the bed specific area; ε, is the void fraction; u<sub>l</sub>, is the liquid phase superficial velocity; D<sub>l</sub><sup>i</sup>, is the diffusivity of component i in the liquid phase; and μ<sub>l</sub>, is the dynamic viscosity of the liquid phase.

The gas-phase mass transfer coefficients are calculated by:

$$k_g^i = C_g \frac{a_t D_g^i}{(4 \varepsilon^2 - 4 \varepsilon h_t)^{1/2}} \left( \frac{\rho_g u_g}{a_t \mu_g} \right)^{3/4} \left( \frac{\mu_g}{\rho_g D_g^i} \right)^{1/3} \quad (17)$$

where, C<sub>g</sub>, is the packing constant for gas phase; h<sub>t</sub>, is the liquid hold-up per unit volume; u<sub>g</sub>, is the gas phase superficial velocity; D<sub>g</sub><sup>i</sup>, is the diffusivity of component i in the gas phase; and μ<sub>g</sub>, is the dynamic viscosity of the gas phase.

The liquid hold-up per unit volume is calculated using<sup>3</sup>:

$$h_t = \left( \frac{12 a_t^2 \mu_l}{g \rho_l} \right)^{1/3} \left( \frac{a_w}{a_t} \right)^{2/3} \quad (18)$$

where a<sub>w</sub> is the specific wetted area for mass transfer calculated by:

$$\frac{a_w}{a_t} = C_h \left( \frac{\rho_l u_l}{a_t \mu_l} \right)^{0.15} \left( \frac{a_t u_l^2}{g} \right)^{0.1} \quad \text{when } Re_l < 5 \quad (19)$$

and

$$\frac{a_w}{a_t} = 0.85 C_h \left( \frac{\rho_l u_l}{a_t \mu_l} \right)^{0.25} \left( \frac{a_t u_l^2}{g} \right)^{0.1} \text{ when } Re_l > 5 \quad (20)$$

Here,  $C_h$  is the packing constant for liquid hold-up.

The specific heat capacities were calculated in both phases using a polynomial equation in the corresponding temperature<sup>18</sup>:

$$c_{pi}^j = c_1 + c_2 T + c_3 T^2 + c_4 T^3 \quad (21)$$

Here, the superscript  $j$  denotes the phase and the subscript  $i$  the component.

The global heat transfer coefficient ( $U_T$ ) is calculated using the assumption of all resistance in gas phase as:

$$U_T = \left( \frac{1}{h_l} + \frac{1}{h_g} \right)^{-1} \cong h_g \quad (22)$$

Here,  $h_l$  and  $h_g$  are the convective heat transfer coefficients in the liquid and gas phases, respectively.

The convective heat transfer coefficient ( $h_g$ ) is calculated<sup>19</sup> by:

$$Nu = 2 + 0.69 Re^{0.5} Pr^{0.33} \quad (23)$$

Here,  $Nu = h_v d_p / k$ ,  $Re = d u_v \rho / \mu$ , and  $Pr = c_p \mu / k$ ,  $d_p$  is the porous particle diameter,  $u_v$  is the vapor phase superficial velocity,  $k$ ,  $\rho$ ,  $\mu$ , and  $c_p$  are the vapor phase thermal conductivity, density, viscosity, and specific heat at constant pressure, respectively.

The thermal conductivity of component  $i$  in vapor phase is calculated using<sup>20</sup>:

$$k_i = C_{i1} T_v + C_{i2} \quad (24)$$

The constants  $C_{i1}$  and  $C_{i2}$  are taken from reference 20.

The diffusivities in vapor phase are calculated using the following formula from Reid et al.<sup>18</sup>

$$D_i^v = C_{Di} T_v^{1.75} / P \quad (25)$$

Here, the  $C_{Di}$  are coefficients calculated for all mixture components, see appendix.

The diffusivity of  $CO_2$  in liquid phase is calculated<sup>3</sup> using:

$$D_{CO_2}^l = 2.35 \cdot 10^{-6} \exp(-2119/T_l) \quad (26)$$

The latent heat for the change of phase ( $\Delta H^{vl}$ ) is calculated using:

$$\Delta H_i^{vl} = \Delta H_i^v - \Delta H_i^l \quad (27)$$

All the mixture properties are computed as weighted fractions, i.e., for a generic property  $A$ :

$$A_{\text{mixture}} = \sum_{i=1}^{nc} x_i A_i \quad (28)$$

Here,  $x_i$  is the component  $i$  molar fraction.

The absorption of  $\text{CO}_2$  in strong hydroxide solutions has been successfully treated as absorption accompanied by an irreversible second order reaction. In strong hydroxide solutions, the equilibrium concentration of  $\text{HCO}_3^-$  ions can be neglected and the overall reaction is



The reaction rate is given by:

$$-r_{\text{CO}_2} = k_R [\text{CO}_2] [\text{OH}^-] \quad (30)$$

The specific rate constant  $k_R$  is calculated<sup>17</sup> using:

$$k_R = \text{Exp}(31.396 - 6658.0/T_1)/1000, (\text{m}^3 \text{mol}^{-1} \text{s}^{-1}) \quad (31)$$

The calculation of the heat of reaction ( $\Delta H_R$ ) was carried out using the heat of formations for the different compounds in eq. (29). The values used were taken from reference 20, -1131.0, -241.8, -393.5, and -426.7 kJ/mol, respectively. The computed value at room temperature is  $\Delta H_R = -367.7$  kJ/mol.

### 3.4.2 Solution Procedure

#### 3.4.2.1 Introduction

The system of equations that describes the proposed dynamic model is given by eqs. (2) and (3) for mass balances of the  $i$ -components in both phases plus the definitions of the interphase mass transfer terms given by eqs. (4) and (7). The computation of the temperature profiles in both phases is accomplished by solving numerical eqs. (10) and (11). The values of all the parameters used in the aforementioned equations were calculated using eqs. (16) to (29) presented in the parameter determination sections.

#### 3.4.2.2 Numerical Methods

The main equations derived in this model are hyperbolic partial differential equations which may be solved using numerical techniques. Numerical methods for solving hyperbolic partial differential equations yield non-singular difference schemes. Let consider, for example, the hyperbolic equation

$$\frac{\partial u}{\partial t} + \alpha \frac{\partial u}{\partial z} + N_i = 0, \alpha = \text{const.} > 0, \quad (32)$$

Eq. (32) can be solved using different finite differences schemes. In this work, we tried two simple schemes. One explicit given by<sup>21</sup>:

$$\frac{u_j^{n+1} - u_j^n}{\Delta t} + \alpha \frac{u_j^n - u_{j-1}^n}{\Delta z} = 0 \quad (33)$$

Here  $n$  and  $j$  are the time and length indexes,  $\Delta t$  and  $\Delta z$  are the time and axial length intervals, respectively. This scheme is very simple to implement computationally. It is also consistent with

the original differential equation (32) and conditionally stable. Thus, the finite-difference scheme (33) will be stable if the following condition (Courant's condition<sup>21</sup>) is met:

$$\left| \alpha \frac{\Delta t}{\Delta z} \right| \leq 1 \quad (34)$$

The other alternative used was an implicit scheme given by:

$$\frac{u_j^{n+1} - u_j^n}{\Delta t} + \alpha \frac{u_{j+1}^{n+1} - u_{j-1}^{n+1}}{2 \Delta z} = 0 \quad (35).$$

This scheme is absolutely stable for any relation  $\Delta t/\Delta z$ ; however, it is more difficult to implement computationally, requiring a diagonal matrix equation solver. We implemented both schemes and we compared the results produced by both, in order to select the most appropriate.

Repeated runs showed that the results obtained with both methods were very similar. Therefore, we decided to use the explicit scheme.

### 3.4.2.3 Computer Code Development

The proposed model was implemented in a computer code written in a structured language (FORTRAN). Figure 52 shows a description of the code. The key parts of the code are:

- I. **Geometric parameter determination.** All input data are read from especial datafiles or calculated from the raw data in a DATA subroutine.
- II. **Vapor-Liquid equilibrium** data are calculated in a especial subroutine using the procedure described in section 1.1.3.
- III. **Physical properties calculation.** A especial subroutine interacts with the mass and energy balances subroutines to update the values of all physical properties.
- IV. **Mass and energy balances** are solved using numerical methods programmed in appropriate subroutines.

The key area of the code is given by the interaction between the mass and heat balance subroutines supported by the physical properties calculation subroutine.

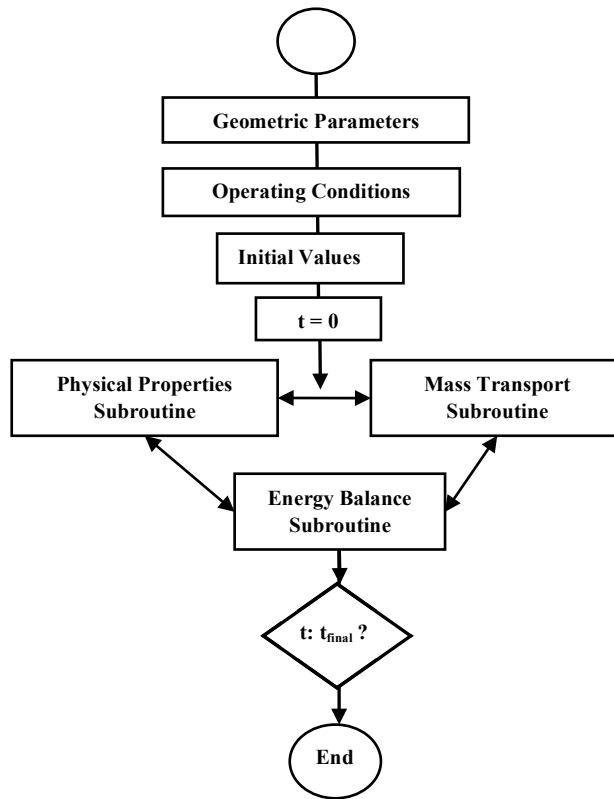


**Figure 50. Structure of the Computer code**

### 3.4.3. Experimental Part

In order to support the work done on the theoretical model, experiments were carried out using a commercial laboratory column available in our laboratory. The goal of this part of the project work was to measure gas-liquid mass transfer coefficients with and without chemical reaction.

#### 3.4.3.1 Experimental Apparatus

A computer controlled gas absorption column from EDIBON (CAGC)<sup>23</sup> is used to carry out the experimental program. The packed column consists of a glass cylindrical column with a height of 1400 mm and 75 mm internal diameter. This column is filled with Raschig rings, 8 mm diameter. It includes glass ends for input and output of gases and liquids, three sample points, and liquid (water and NaOH aqueous solution) and gas circuits (air and CO<sub>2</sub>). The liquid is impelled towards the column using a centrifugal pump (maximum flow rate: 540 L/h). The liquid flow is measured using a flow sensor and controlled by a PID controller. The gas mixture is mobilized by a compressor, which provides a maximum flow of 6 m<sup>3</sup>/h at a pressure of 1 bar. Gas mixtures of CO<sub>2</sub> and air were fed into the experimental equipment using the gas mixing system shown in Figure 52.

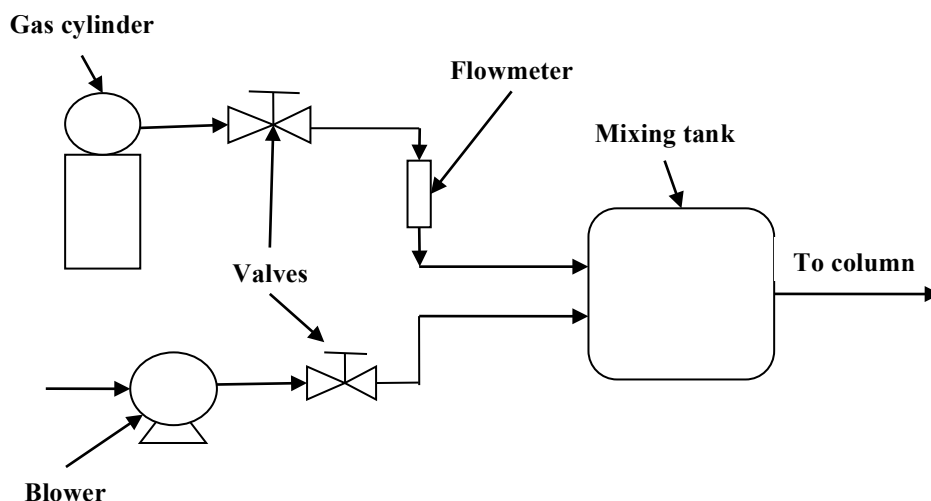


**Figure 51. Gas feed system.**

The gas circuit consists of CO<sub>2</sub> provided by a pressured cylinder and control through a needle valve and air supplied by a blower. Both gaseous currents are mixed into an 8 liter capacity tank and enter the base of the column through a side inlet located below the bed level, so that the gaseous mixture is as homogeneous as possible. Both gas flows are measured by sensors and flowmeters. The temperature, pressure, and flow rate of the input stream to the column are measured by sensors and computer controlled.

Carbon dioxide samples are extracted from the upper and lower parts of the column. The measuring system consists of a glass syringe of 100 ml capacity and two interconnected glass tanks located at different heights. A KOH solution is used to absorb the gas sample to be analyzed. Two 3 way-valves direct the gaseous currents during the analysis process. Liquid samples are also taken from the same points to be analyzed and complete the data collection.

All experiments are computer controlled. Simultaneously, visualization of all parameters involved in the process is provided using Labview software. Graphic representation, in real time, of all the process/system parameters is possible. All sensors involved in the process are automatically calibrated. It is possible to change the values of the actuators in real time to allow immediate analysis of curves and responses of the entire process.

### 3.4.3.2 Experimental Procedure

The experimental procedure was taken from the commercial column manual<sup>22</sup>. Modifications were introduced to simplify the experiments. Liquid and gas phase samples are taken from the bottom and top parts of the column. The liquid samples were supposed to be analyzed by titration with HCL using phenolphthalein as indicator. The procedure for analyzing gas samples is based upon taking samples from the bottom and top parts of the column; mix them with a 5% KOH solution until complete absorption by the base; and analysis of the alkaline solution by titration with a HCl 5% solution using phenolphthalein as indicator. However, due to the inaccuracy and unreliability of the prescribed original procedure we decided to analyze the



concentration of the gas and liquid exit samples by using an electronic Fisher pH-meter. The pH-meter has an absolute error of 0.1 pH units and gives more reliable and accurate values plus the procedure is much simpler to carry out than the titration.

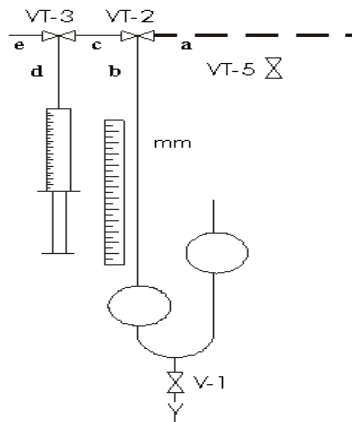


**Figure 52. Apparatus for gas analysis, reproduced from reference 22.**

The sample is taken from the column and analyzed using the two three ways valves, VT-3 and VT-2, depicted in Figure 54. Combinations of the two valves positions allow the operator to get sample from the column through lines a/c/d, inject the sample into the spherical containers filled with the KOH solution through lines b/c/d, and once the  $\text{CO}_2$  is completely absorbed take a solution sample for analysis through lines b/c/e.

### 3.4.3.3 Theoretical Derivation

A mass balance for  $\text{CO}_2$  is carried out in the differential volume depicted in Figure 55.

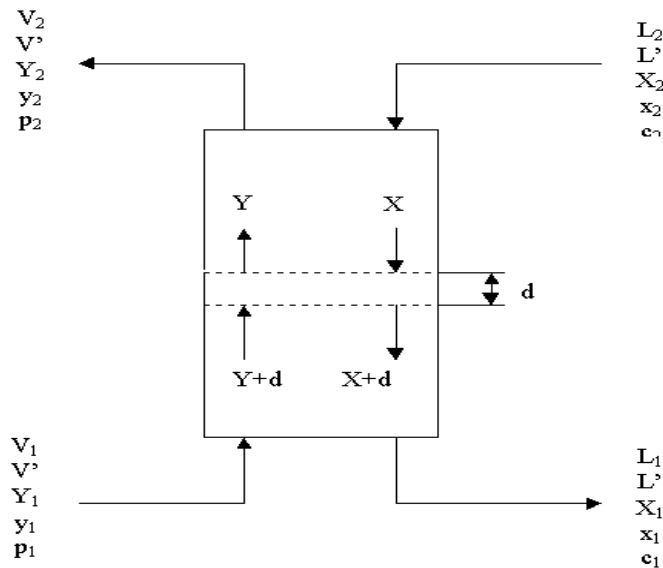


**Figure 53. Mass transfer control volume in the packed absorption tower (ref. 23).**

Here,  $L$  and  $V$  are the liquid and gas molar flow rates, respectively;  $L'$  and  $V'$  are the solute free molar flows;  $X$  and  $Y$  are the solute free molar fractions,  $d$  is the differential height,  $c$  is the molar concentration, and  $P$  is the pressure. The subscripts 1 and 2 refer to the variables values at the bottom and the top of the column, respectively.

A mass balance in the differential volume shown in Figure 55 leads to:<sup>23</sup>

$$H = \text{HTU NTU} \quad (36)$$

where  $H$  is the column height, HTU is the height of a transfer unit, NTU is the number of transfer units to achieve a given separation.

Eq. (36) can be written as:

$$H = \frac{L_m}{K_{OL} a_v c_t} \int_{c_1}^{c_2} \frac{dc}{c_{eq} - c} \quad (37)$$

Here,  $L_m$  is the liquid molar flux,  $a_v$  is the mass transfer specific area for the packing (area per unit volume),  $c_t$  is the total molar concentration in liquid phase, and  $K_{OL}$  is the global liquid side mass transfer coefficient. In the case where Henry's law holds, i.e., the equilibrium curve is a straight line with slope equal to the Henry's constant eq. (37) becomes,

$$H = \frac{L_m}{K_{OL} a_v c_t} \frac{c_1 - c_2}{(c_{eq} - c)_{ml}} \quad (38)$$

Here,  $(c_{eq} - c)_{ml}$  is the logarithmic mean of the concentration difference given by:

$$(c_{eq} - c)_{ml} = \frac{(c_{eq} - c)_1 - (c_{eq} - c)_2}{\ln \left( \frac{(c_{eq} - c)_1}{(c_{eq} - c)_2} \right)} \quad (39)$$

The global liquid side mass transfer coefficient,  $K_{OL} a_v$ , is calculated from:

$$K_{OL} a_v = \frac{L_m}{H c_t} \frac{c_1 - c_2}{(c_{eq} - c)_{ml}} \quad (40)$$

where the logarithmic mean of the concentration difference is calculated using eq. (39).

Evaluation of eq. (40) requires experimental determination of the bottom and top  $\text{CO}_2$  liquid phase concentrations. The total molar concentration,  $c_t$ , is approximated by the solvent only molar concentration as the solutions are dilute. The procedure requires determination of the gas and liquid phase  $\text{CO}_2$  concentrations. The gas phase concentration values are used to evaluate the liquid phase equilibrium concentrations,  $c_{eq}$ , using Henry's law.

### 3.5 Results and Discussion

#### 4.4.1 Experimental Results

##### 4.4.1.1 Mass Transfer Coefficients without Chemical Reaction

We were able to calculate liquid side global mass transfer coefficients,  $K_{OL}$ , as a function of liquid and gas superficial velocities,  $u_l$  and  $u_g$ , respectively. Carbon dioxide absorption is controlled by the liquid side resistance; therefore, we get the liquid side mass transfer coefficient as:

$$\frac{1}{K_{OL}} = \frac{H_{cc}}{k_g} + \frac{1}{k_l} \cong \frac{1}{k_l} \quad (41)$$

where  $H_{cc}$  is the dimensionless concentration Henry's constant,  $k_l$  and  $k_g$  are the liquid and gas sides mass transfer coefficients, respectively.

The results are presented in Figures 56, 57 and Table 13. In order to calculate the values of the mass transfer coefficient ( $k_l$ ) we need to estimate the value of interfacial mass transfer area as the experimental values measure the product of the mass transfer coefficient times the interfacial mass transfer area ( $k_l a_v$ ). In two phase flow the interfacial mass transfer area ( $a_v$ ) is better approximated by the value of the packing wetted area,  $a_w$ , than by the specific area of dry packing,  $a_t$ . The variation of the wetted area has been calculated using eqs. (19) and (20) proposed by Billet and Schultes<sup>24</sup>.

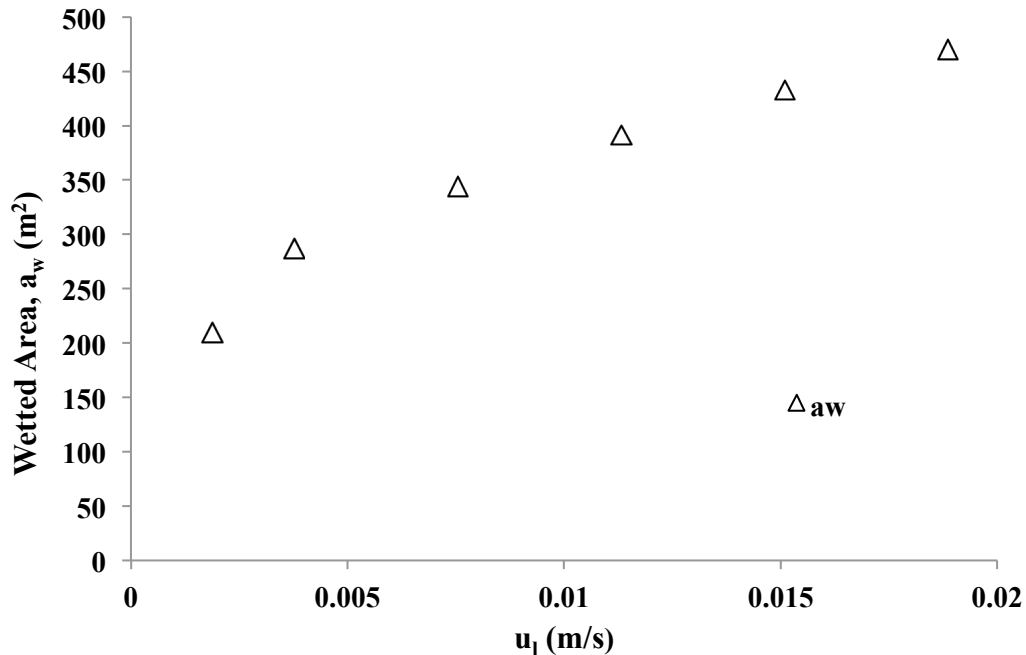


**Figure 54. Variation of the packing wetted area versus liquid phase superficial velocity.**

The calculated values of  $a_w$  as a function of the liquid phase superficial velocity are depicted in Figure 56. It is shown that, as the gas flow remains constant, the wetted area increases

continuously. We used these calculated values of the wetted area in the mass transfer coefficients calculations. We also calculated liquid hold-up values,  $h_t$ , using eq. (18), as these values are needed to calculate corrected values for liquid phase velocities. The calculated liquid side mass transfer coefficients are shown in Figure 57.

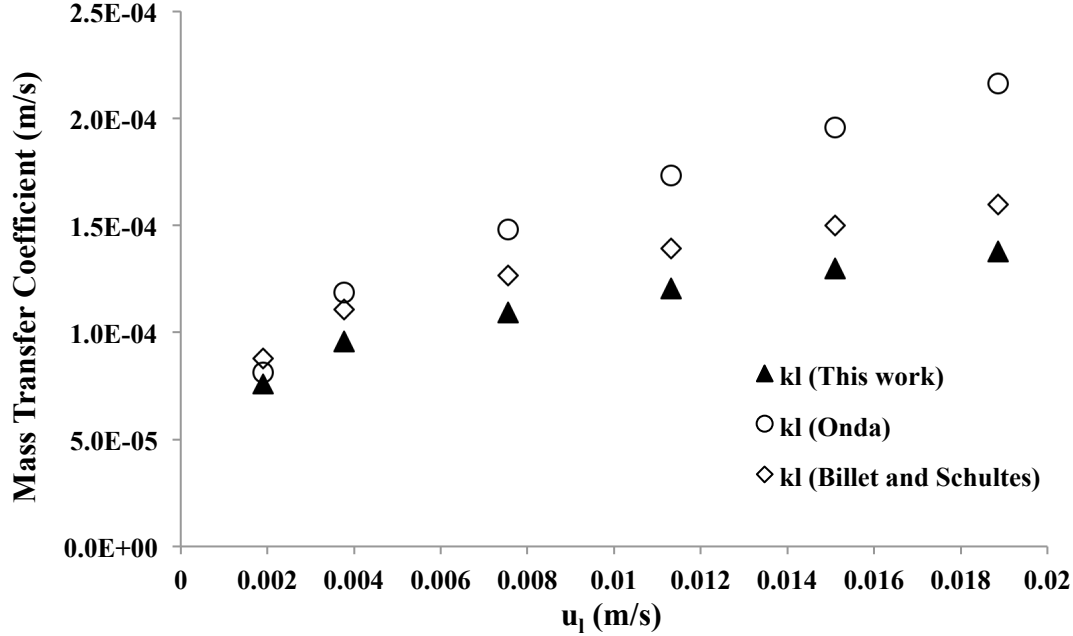


**Figure 55. Comparison of calculated mass transfer coefficients.**

The Figure 57 shows that the value of the mass transfer coefficients increases as the liquid phase superficial velocity increases. Calculations, not shown here, approximately correlated this increase with the cubic root of the superficial velocity.

The comparison of the results determined in this work with literature data is also shown in Figure 57. In the comparison we used the values calculated by Billet and Schultes<sup>24</sup> and Onda et al.<sup>25</sup>.

Billet and Schultes<sup>24</sup> proposed the following equation to calculate mass transfer coefficients for a variety of dumped and structured packings:

$$k_l^i = C_l \left( \frac{\rho_l g}{\mu_l} \right)^{1/6} \left( \frac{a_t D_i}{4 \epsilon} \right)^{1/2} \left( \frac{u_l}{a_t} \right)^{1/3} \quad (42)$$

Here,  $C_l$ , is the packing constant for liquid phase and  $\epsilon$  is the void fraction.

Onda et al.<sup>25</sup> correlated experimental data of several authors to calculate mass transfer coefficients using:

$$k_l^i = 0.0051 \left( \frac{\rho_l}{\mu_l g} \right)^{-1/3} \left( \frac{u_l \rho_l}{a_w \mu_l} \right)^{2/3} \left( \frac{\mu_l}{\rho_l D_l} \right)^{-1/2} (a_t D_p)^{0.4} \quad (43)$$

Liquid-phase mass transfer coefficients are used for O<sub>2</sub>, N<sub>2</sub> and CO<sub>2</sub>. Here, D<sub>p</sub> is the packing particle equivalent sphere diameter. This equation can be also used for calculating the liquid-phase mass transfer coefficients for O<sub>2</sub> and N<sub>2</sub>.

It is also shown in Figure 57 that the calculated liquid side mass transfer coefficients are smaller than the ones predicted by the other authors. The discrepancy with Onda et al.<sup>25</sup> data increases as the liquid superficial velocity increases. This behavior is produced because Onda et al.<sup>25</sup> proposed an increase with the power 2/3 of the liquid superficial velocity and in this work we determined that the mass transfer coefficient increases with a power 1/3. It is important to consider that a 2/3 power is associated with a turbulent flow regime while the exponent 1/3 is associated with a laminar flow regime. In this regard, both sets of data can represent different fluid-dynamic situations and; therefore, a true comparison cannot be achieved. Better agreement is achieved with the data calculated using Billet and Schultes<sup>24</sup> correlation. This behavior is expected as these authors also reported an increase with a power 1/3.

The data used to calculate the mass transfer coefficients are shown in Table 13.

**Table 13. Experimental Data for calculation of mass transfer coefficients.**

Q <sub>l</sub> (m <sup>3</sup> /s)	Q <sub>g</sub> (m <sup>3</sup> /s)	C <sub>g1</sub> (mol/m <sup>3</sup> )	C <sub>g2</sub> (mol/m <sup>3</sup> )	C <sub>l1</sub> (mol/m <sup>3</sup> )	C <sub>l2</sub> (mol/m <sup>3</sup> )	K <sub>OL</sub> a <sub>w</sub> (s <sup>-1</sup> )	a <sub>w</sub> (m <sup>2</sup> /m <sup>3</sup> )	k <sub>l</sub> (m/s)
8.33E-06	5.56E-04	21	20.54	15.315	0.0153	6.36E-03	209.7	7.58E-05
1.67E-05	5.56E-04	21	20.12	14.52	0.0153	1.10E-02	286.7	9.55E-05
3.33E-05	5.56E-04	21	19.73	14.13	0.0153	1.50E-02	343.78	1.09E-04
5.00E-05	5.56E-04	21	19.35	13.75	0.0153	1.88E-02	391.3	1.20E-04
6.67E-05	5.56E-04	21	18.99	13.42	0.0153	2.25E-02	432.63	1.30E-04
8.33E-05	5.56E-04	21	18.64	13.14	0.0153	2.59E-02	469.62	1.38E-04
1.00E-04	5.56E-04	21	20.77	15.34	0.0153	6.36E-03	207.17	7.58E-05
1.67E-05	1.11E-03	21	20.54	15.315	0.0153	1.50E-02	347.52	1.30E-04
5.00E-05	1.11E-03	21	2036	14.35	0.0153	2.35E-02	432.67	1.56E-04

Table 13 also shows some data for a different gas flow rate, 1.11E-3 m<sup>3</sup>/s. These extra data do not show significant variations with the original ones calculated with a gas flow rate equal to 5.56E-4 m<sup>3</sup>/s.

#### 4.4.1.2 Mass Transfer Coefficients with Chemical Reaction

The experimental procedure presented in section 1.3.3 allows one to measure  $K_{OL} a_w$  values as it is necessary to lump together both values because there is no simple experimental procedure to determine the wetted area ( $a_w$ ). Values of  $K_{OL} a_w$  as a function of the liquid superficial velocity ( $u_l$ ) are plotted in Figure 58.

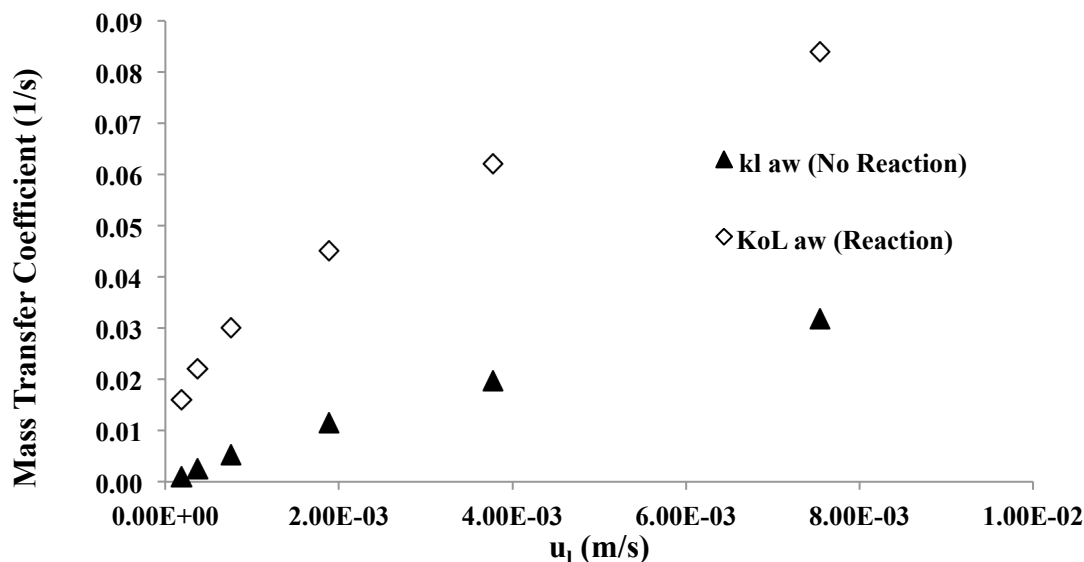


**Figure 56. Comparison of calculated mass transfer coefficients with and without chemical reaction. Chemical reaction data were calculated for  $C_{NaOH} = 0.01$  M.**

In Figure 58 we can see that the global mass transfer coefficient increases as the liquid phase superficial velocity increases. A comparison with similar data measured without chemical reaction shows that the chemical reaction significantly increases the value of the mass transfer coefficients. Similarly to what was done for mass transfer coefficients without chemical reaction we estimated  $a_w$  using eqs. (19) and (20) and calculated the values of  $K_{OL}$ . These results are shown in Figure 59.

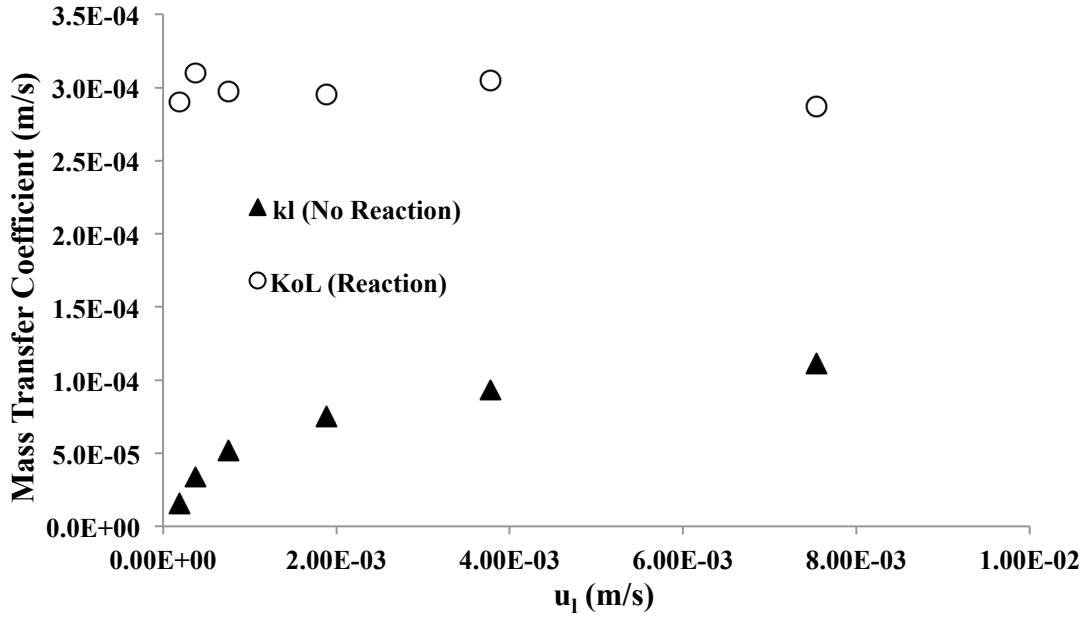


**Figure 57. Calculated mass transfer coefficients with and without chemical reaction.**

We can see in this Figure that, once we account for experimental error, the mass transfer coefficients do not vary with the liquid superficial velocity. This finding is contrary to what happened in the case without chemical reaction shown in the same Figure. In order to find an explanation we used the equation for the global mass transfer coefficient in the presence of chemical reaction eq. (9):

$$\frac{1}{K_{OL}} = \frac{H^{\infty}}{k_g} + \frac{1}{E k_l} \quad (9)$$

where E is the enhancement factor given by eq. (8). An estimation of the values of the terms  $kg/H^{\infty}$  and  $E k_l$  proved that the mass transfer process is controlled by the liquid phase resistance and consequently,

$$K_{OL} = E k_l = \frac{\sqrt{k_R D_{CO_2} C_{OH^-}}}{k_l} k_l = \sqrt{k_R D_{CO_2} C_{OH^-}} \quad (44)$$

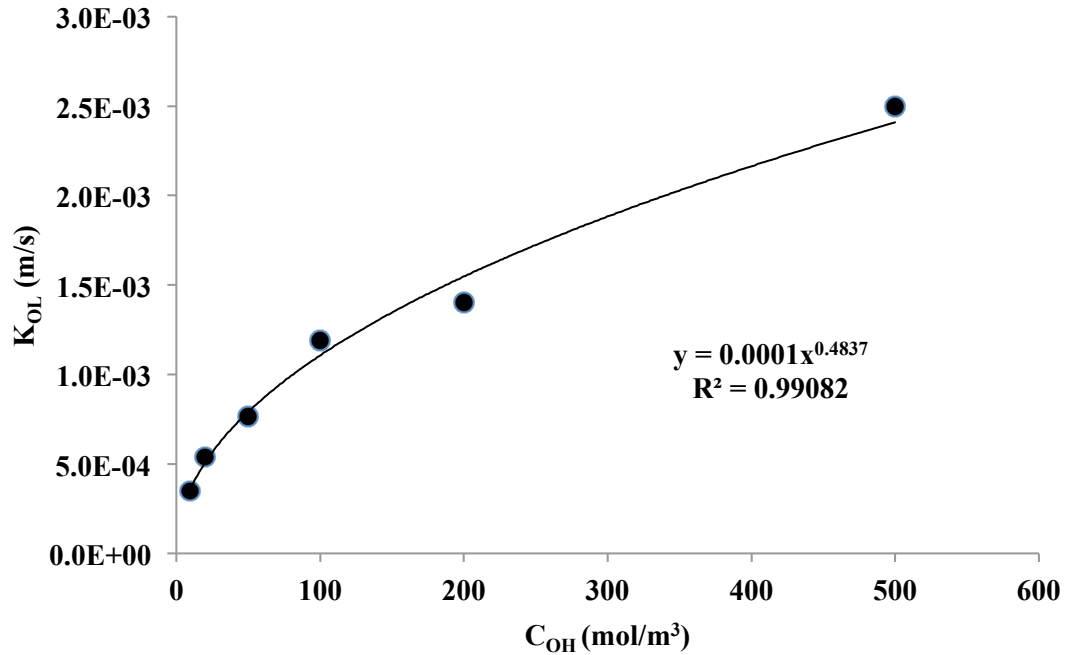


**Figure 58. Variation of mass transfer coefficients with NaOH concentration.**

Therefore, in the case when the liquid phase resistance controls the process the global mass transfer coefficient is proportional to the square root of the  $OH^-$  concentration. In order to test this conclusion we conducted several experiments with different  $OH^-$  concentrations. The results are shown in Figure 60. Figure 60 shows very good agreement with eq. (44) confirming the variation of the global liquid mass transfer coefficient with the square root of the NaOH concentration.

In order to test our estimates that showed liquid mass transfer resistance is the controlling step in all cases we also conducted some experiments varying the gas phase velocity only. These results, not presented here, showed that there was only marginal variation of the global liquid side mass transfer coefficient with the value of the gas velocity. In conclusion, all these experiments show that the value of the global mass transfer coefficient is mainly controlled by the value of square root of the concentration of the  $OH^-$  ion.

## 4.4.2 Dynamic Simulation Results

### 4.4.2.1 Code Validation

The computer code implementing the proposed model was thoroughly checked. The values of all geometry parameters, physical properties, and transport properties were calculated using the computer code and verified against literature values. Particularly useful in this endeavor was the work of Greer's<sup>3</sup>. A direct comparison with Greer's work<sup>2,3</sup> could not be achieved as these authors used alkylamines as solvents in their work instead of water alkaline solutions; however, we introduced a modification in our code by simulating their kinetics in a simple limiting case,



direct reaction kinetics. Typical data for this case are shown in Figure 61. These results, and others not shown here, produced very good agreement with Greer's results<sup>3</sup>.

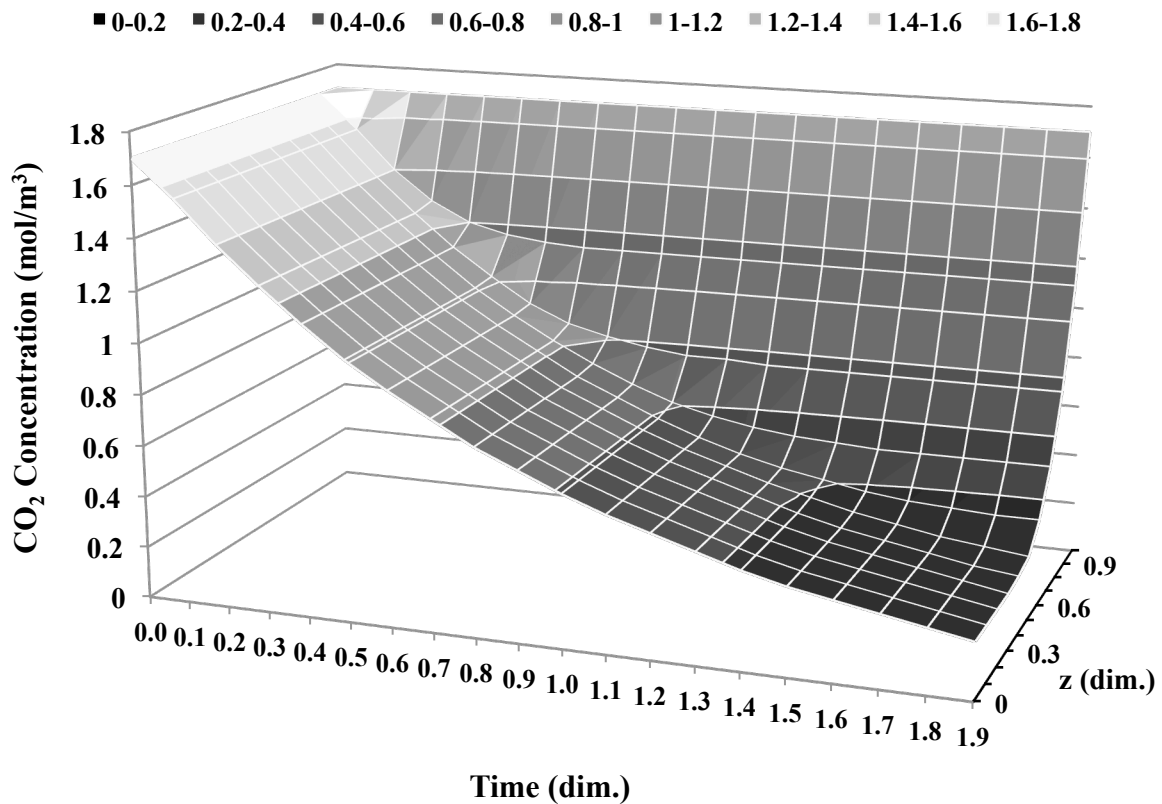


**Figure 59. Contour plot showing typical carbon dioxide concentration change with time and position.**

The values used in the simulations that produced Figure 61 are, gas phase  $C_{CO_2} = 1.7 \text{ mol/m}^3$ , gas superficial velocity ( $u_g$ ) = 0.5 m/s, liquid superficial velocity ( $u_l$ ) = 0.1 m/s,  $C_{OH} = 50 \text{ mol/m}^3$ , and height = 4 m. The values of the geometric and packing parameters for the column are listed in Table 14.

The plot depicts a top-view of the absorption column. The depth axis depicts the dimensionless height from the top ( $z=0$ ) to the bottom ( $z=1$ ). The horizontal axis depicts the dimensionless time, from left to right, while the vertical axis shows  $CO_2$  concentration values in gas phase. The results on the back wall ( $z=1$ ) represent the input  $CO_2$  concentration values,  $C_{CO_2} = 1.7 \text{ mol/m}^3$ . The left side wall ( $t=0$ ) represents the initial condition inside the column. In our simulations we assumed that before significant reaction occurs, the gas and liquid phases saturated the column. The reason is that the highest  $CO_2$  concentration is always located at the bottom of the column while the chemical species that produces the reaction, NaOH, enters by the top. The concentration decreases as the color increases, i.e., light color values are higher than darker ones. We can see that as time increases the gas concentration of  $CO_2$  at the top of the column decreases. We will comment in other sections on the influence of operating parameters on  $CO_2$  concentration values.

**Table 14. Column geometric and packing parameters (Montz B 200 metal structured packing<sup>3</sup>)**

Parameter	Units	Default value	Range	Reference
Height	m	4	1-10	Richardson et al. <sup>23</sup>
Tower Diameter	m	1	0.5-2	Richardson et al. <sup>23</sup>
Dry specific area ( $a_T$ )	$m^2/m^3$	200	200-500	Billet and Schultes <sup>24</sup>
Void Fraction ( $\epsilon$ )	$m^3/m^3$	0.979	0.979	Billet and Schultes <sup>24</sup>
Equivalent diameter	m	0.01	0.005-0.02	This work
Packing coefficient ( $C_l$ )	dimensionless	0.971	0.971	Billet and Schultes <sup>24</sup>
Packing coefficient ( $C_h$ )	dimensionless	0.547	0.547	Billet and Schultes <sup>24</sup>
Packing coefficient ( $C_v$ )	dimensionless	0.390	0.390	Billet and Schultes <sup>24</sup>

#### 4.4.2.2 Heat Transfer Results

We will present our results throughout this report by including a series of Figures. In order to calculate the required results we based all our runs in a default set of parameters mainly taken from Greer<sup>3</sup>. Geometric parameters of the column, packing parameters, and operating variables comprise this default set. The default set provides all the required information to simulate the operation of the column. In case we were interested in studying the influence of one parameter on the absorption process we only varied this parameter while the others were taken from the values listed in the default set.

Table 14 lists the geometrical and packing parameters used while Table 15 lists the operating variables used. Both tables also list the variation range used for each parameter in this work.

The temperature profiles throughout the column were calculated solving the energy balances given by eqs. (13) and (14) for both phases. In the absorption process by high alkaline solutions CO<sub>2</sub> is always the limiting reactant; therefore, the amount of heat generated by the reaction will be related to the amount of CO<sub>2</sub>.

**Table 15. Input data for mass and heat transfer subroutines.**

Variable	Units	Default value	Range	Reference
Liquid phase superficial velocity ( $u_l$ )	m/s	0.1	0.05-1	Greer <sup>3</sup>
Gas superficial velocity ( $u_g$ )	m/s	0.1	0.05-1	Greer <sup>3</sup>
CO <sub>2</sub> concentration	mol/m <sup>3</sup>	1.7	1.7-17	This work
OH <sup>-</sup> concentration	mol/m <sup>3</sup>	50	10-200	This work
N <sub>2</sub> concentration	mol/m <sup>3</sup>	32.1	32.1	Reid et al. <sup>18</sup>
O <sub>2</sub> concentration	mol/m <sup>3</sup>	5.1	5.1	Reid et al. <sup>18</sup>
Pressure ( $P_o$ )	Pa	$1.1 \cdot 10^5$	$1.0 \cdot 10^5$ - $1.1 \cdot 10^5$	This work
Temperature ( $T_o$ )	K	300	300	This work

We show in Figures (62) and (63) the computed temperature profiles for both phases at steady-state conditions (long times) for high NaOH concentrations (0.1M) and different CO<sub>2</sub> concentrations.

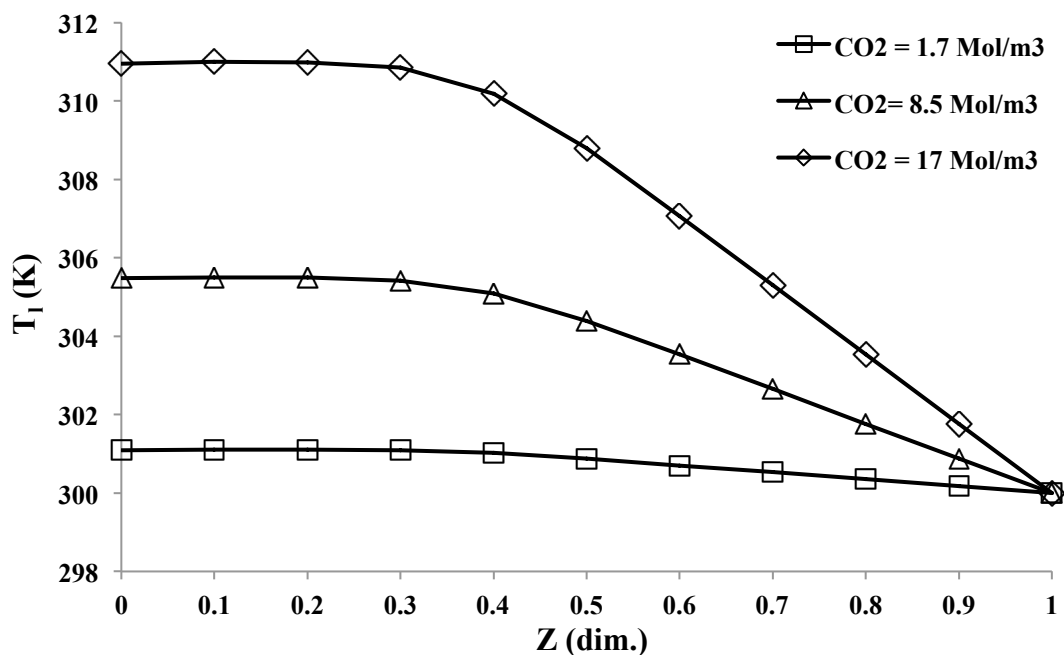


**Figure 60. Liquid phase temperature profile as a function of input CO<sub>2</sub> concentration.**

Figure 62 shows that the liquid phase temperature increases from the inlet (top of the column,  $z=1$ ) to the exit (bottom,  $z=0$ ). We can also see that increasing the concentration of the limiting reactant  $\text{CO}_2$  increases the chemical reaction and, consequently, the temperature value.

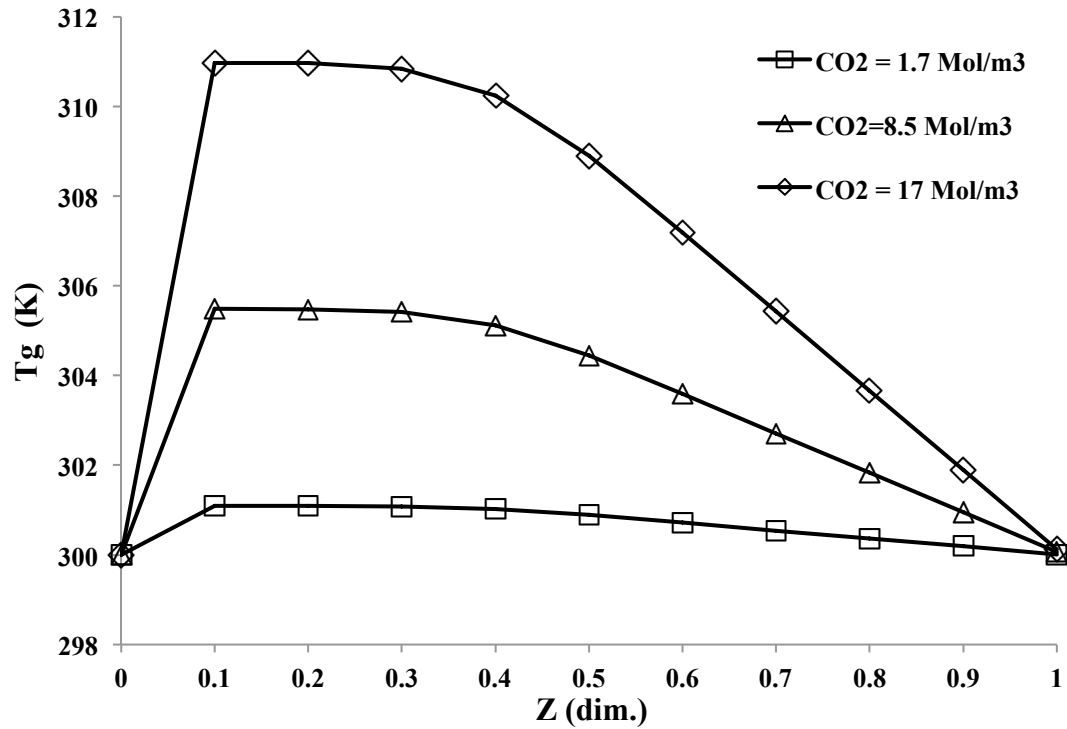


**Figure 61. Gas phase temperature profile as a function of input  $\text{CO}_2$  concentration.**

Figure 63 depicts the steady-state gas phase temperature profile throughout the column. We can see that the gas phase temperature also increases value close to the inlet point (bottom of the column,  $z=0$ ) while decreasing in the rest of the column. The major increase in temperature in the bottom part of the column is produced by the high concentration of  $\text{CO}_2$  in that part of the column. As the  $\text{CO}_2$  concentration decreases to the top the heat generated by the reaction decreases too and interfacial heat transfer becomes also important. Probably, this effect produces a decrease in the temperature of the gas phase in the rest of the column as it comes in contact with increasingly colder liquid.

Inspection of Figures (62) and (63) shows that through most of the column length both phases are at thermal equilibrium, i.e., both temperatures are almost the same even though gas phase temperatures are always slightly smaller than the liquid phase ones. Exceptions to this finding are the top and bottom parts of the column. This finding sheds light on the critical role played by the global heat transfer coefficient ( $H_L$ ). We have assumed in this work that the interfacial heat transfer is controlled by the resistance in the gas phase ( $1/h_g$ ). Calculation of the heat transfer coefficients in both phases, using eq. (22), supports this assumption. Therefore, the value of this transport parameter determines the magnitude of the interfacial heat exchange term. Greer<sup>3</sup> also pointed out this fact in his work. Unfortunately, there are not reported values of direct measurements of this transport parameter in porous media for two phase flow. Normally,

researchers use data for wetted columns<sup>23</sup> or apply the analogy between heat and mass transfer (Greer<sup>3</sup> and this work as examples). Greer<sup>3</sup> used the analogy between the Chilton-Coburn analogy (Dewitt and Incropera<sup>20</sup>) to approximate the heat transfer coefficient with the mass transfer coefficient. The Chilton-Coburn analogy is based on the assumption that the boundary layer profiles for the heat and mass are the same<sup>3</sup>; therefore, the dimensionless heat transfer coefficient Colburn factor ( $j_H$ ), is considered equal to the dimensionless mass transfer coefficient Colburn factor ( $j_M$ ) or:

$$j_H = St^{2/3} Pr^{1/3} = j_M = St_m^{2/3} Sc^{1/3} \quad (45)$$

Here,  $St$  is the heat transfer Stanton number [ $h_g/(\rho V C_p)$ ],  $Pr$  is the Prandtl number ( $C_{pm} \mu/k$ ),  $St_m$  is the mass transfer Stanton number ( $k_m/V$ ),  $Sc$  is the Schmidt number [ $\mu/(D \rho)$ ],  $D$  is the diffusion coefficient,  $C_{pm}$  is the specific heat per unit mass, and  $k_m$  is the mass transfer coefficient.

Simple algebraic calculations, after replacing into eq. (45) the definitions given above, show that  $h_g$  can be calculated using:

$$h_g = k_m (k/D)^{2/3} (\rho C_{pm})^{1/3} \quad (46)$$

Eq. (46) was used by Greer<sup>3</sup> in his work. In this research project we used eq. (22) derived for mass transfer in porous media assuming once again equivalence between heat and mass transport. Calculation of the heat transfer coefficients using both eqs. (22) and (47) showed that they agree reasonably well with differences between them never bigger than 20%. However, the error in the evaluation of the heat transfer coefficient can affect the results. The most impacted variable is the temperature in the gas phase. In any case, our results show conclusively that for the small  $CO_2$  concentrations relevant to this work,  $C_{CO_2} < 2 \text{ mol/m}^3$ , there are only very small variations of temperature in both phases throughout the column, one or two Ks. Greer<sup>3</sup> also drew similar conclusion.

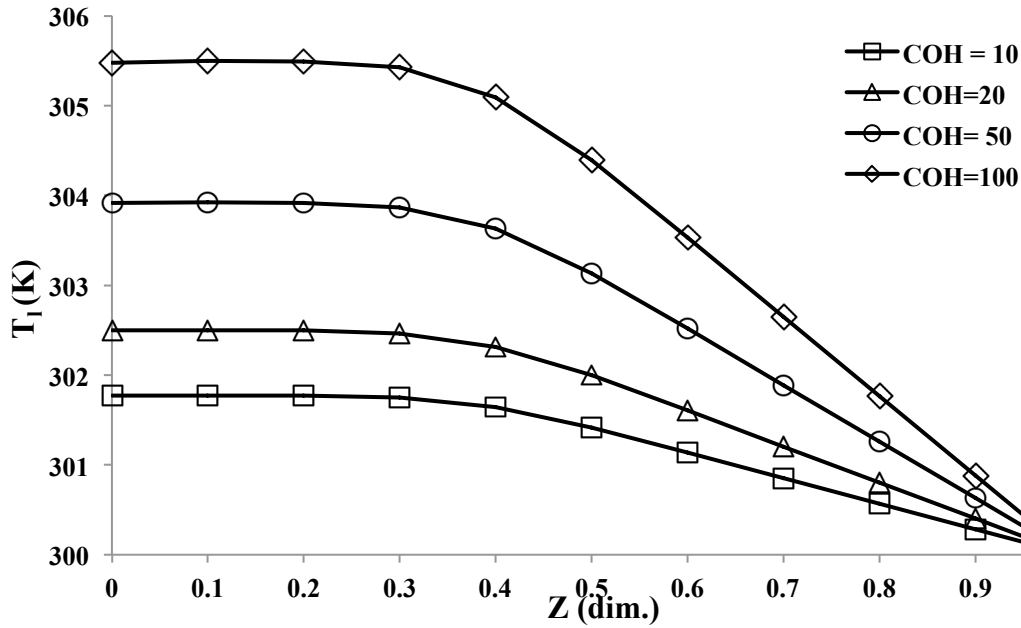


**Figure 62. Liquid phase temperature profile as a function of NaOH concentration.**

In Figure 64 a  $\text{CO}_2$  input concentration value equal to  $8.5 \text{ mol/m}^3$  was used to study the temperature differences. We can see that the liquid phase temperatures increase as the NaOH concentration increases. The effect is less pronounced than in the case of the limiting reactant  $\text{CO}_2$ . However, NaOH is the excess reactant and it should not affect the conversion. The concentration of NaOH ( $C_{\text{OH}}$ ) affects the value of the enhancement factor ( $E$ ), eq. (44); therefore, affects the mass transfer process and not, directly, the heat transfer. From eq. (44) we know that the global mass transfer coefficient is proportional to the square root of the NaOH concentration; consequently, we propose that the increase in  $C_{\text{OH}}$  leads to an increase in the mass flow of the limiting reactant ( $\text{CO}_2$ ) towards the liquid phase and to more chemical reaction followed by increased heat release. In order to test this proposition we plotted the maximum temperature in liquid phase compared to the value of the enhancement factor. The results are shown in Figure 64.

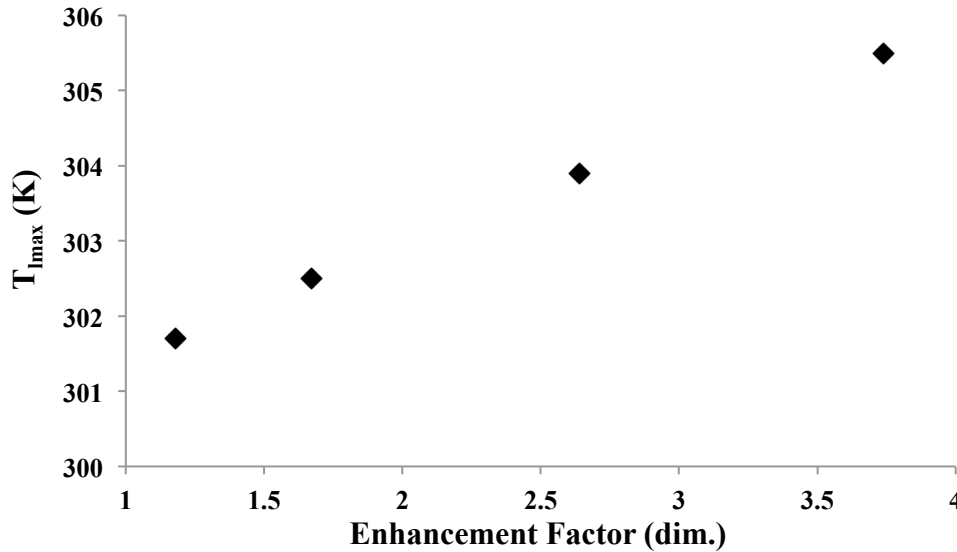


**Figure 63. Maximum temperature in liquid phase as a function of enhancement factor.**

A clear relationship between the values of the maximum liquid phase temperature and the value of the enhancement factor is shown in Figure 65. This finding supports the explanation presented above.

In practically all computations carried out in this project the variations in temperature were very minor due to the small values of the CO<sub>2</sub> concentrations relevant to this study. In conclusion, heat effects are not an important issue within the practical problems dealt with in this research project. We can even say that an isothermal model will be adequate in most practical cases.

#### 4.4.2.3 Mass Transfer Results

The concentration profiles throughout the column were calculated solving the mass balances given by eqs. (2) and (3) for both phases. We depict our results in a series of Figures. In our simulations we worked with all dimensionless variables, except chemical species concentrations and temperatures, in the following way:

$$t^* = z_0/u_0, z^* = z/z_0, u_g^* = u_g/u_0, u_l^* = u_l/u_0 \quad (47)$$

where  $u_0$  is a reference velocity equal to 2 m/s and all the variables with asterisks are dimensionless variables.

The horizontal axis represents the dimensionless length of the absorption tower with  $z=0$  being the bottom and  $z=1$  the top of the tower. It should be remembered that the liquid phase enters by the top and the gas phase by the bottom. The critical chemical species are O<sub>2</sub>, N<sub>2</sub>, CO<sub>2</sub>, and H<sub>2</sub>O in the gas phase. In the liquid phase the ion CO<sub>3</sub><sup>=</sup> is the most important chemical species to consider. The hydroxyl ion (OH<sup>-</sup>) enters from the top in high concentrations, pH ≥ 12. In the case of high alkaline concentration solutions it is normally assumed that this concentration remains constant throughout the column. The model proposed here assumes that chemical reaction occurs only inside the thin layer on the liquid phase; therefore, the concentration of CO<sub>2</sub>

is zero in the liquid phase and this chemical species is replaced by the carbonate ion ( $\text{CO}_3^{=}$ ). We also calculated the concentration of this ion in the liquid phase.

Typical simulation results are shown in Figures 66 and 67. These simulations were conducted using the default set of parameters shown in Tables 14 and 15.

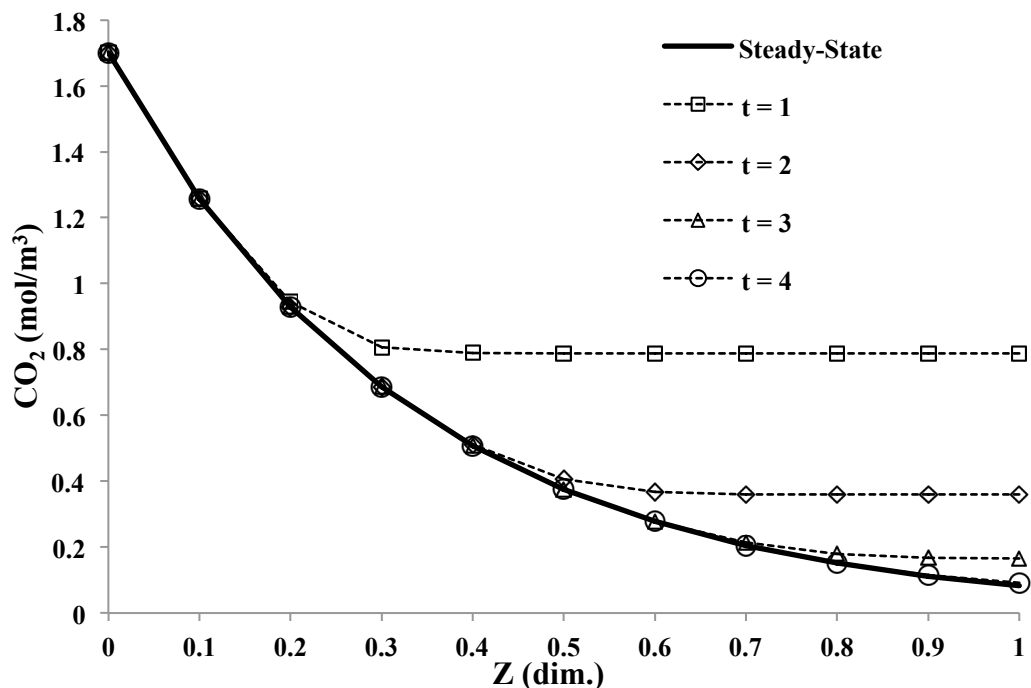


**Figure 64. Gas phase CO<sub>2</sub> concentration profile through the absorption column.**

The highest CO<sub>2</sub> concentration in the gas phase occurs at the bottom of the column ( $z=0$ ), gas phase inlet. There is a continuous decrease from the bottom to the top of column ( $z=1$ ), the minimum concentration point. As time increases the CO<sub>2</sub> profile approaches the steady-state solution.

There is a relationship between the CO<sub>2</sub> concentration in gas phase and the  $\text{CO}_3^{=}$  ion concentration in the liquid phase as the carbonate ions appear due to the consumption of CO<sub>2</sub> and the stoichiometric ratio is one to one. Figure 67 shows that the time evolution of the carbonate profile in liquid phase is more complex than the corresponding CO<sub>2</sub> profile in gas phase. Initially, the values of the ion concentration are higher than the steady-state values in the top of the column while the reverse is true in the bottom of the column. As times increases the concentration of carbonate ion decreases in the top region while the concentration in the bottom increases until converging to the steady-state solution. The results shown in Figure 67 suggest intense axial mass transport for the carbonate ions.



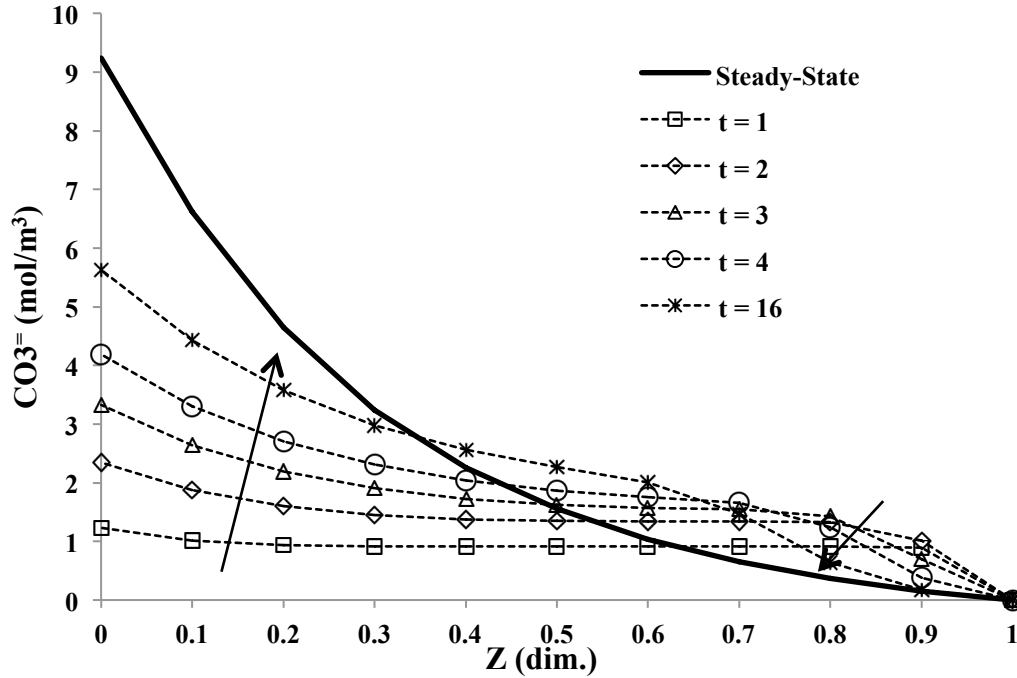


**Figure 65. Time evolution of the carbonate ion profiles at different times.**

The influence of the superficial liquid ( $u_l$ ) on the different chemical species concentration profiles is shown in Figures 68 and 69.

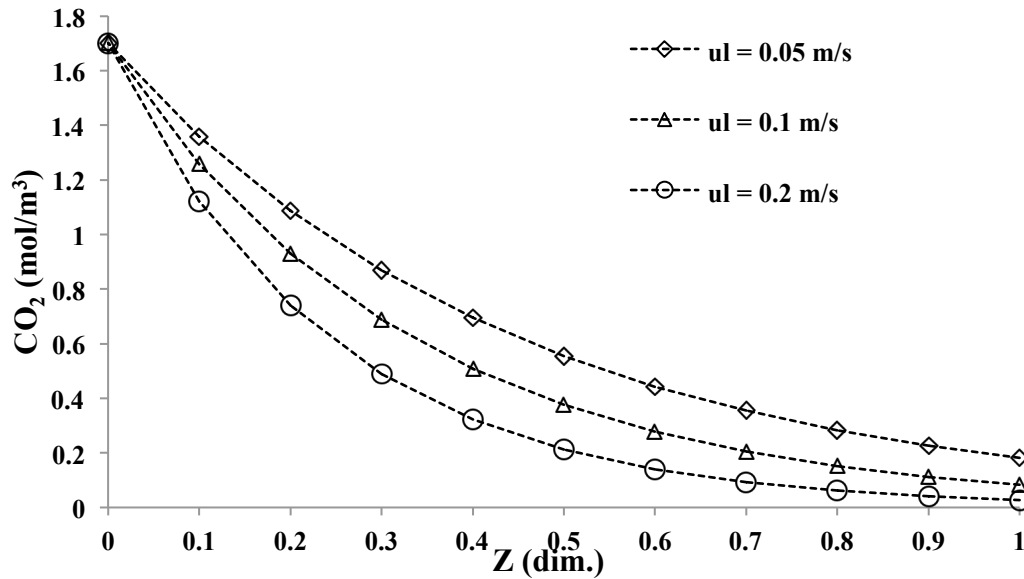


**Figure 66. Influence of the liquid phase superficial velocity ( $u_l$ ) on the  $\text{CO}_2$  profile.**

In Figure 68 it is shown that as the liquid velocity increases the amount of  $\text{CO}_2$  in gas phase decreases. This is produced by an increased in the mass transfer from the gas into the liquid phase. The decrease in the amount of  $\text{CO}_2$  in gas phase is accompanied by an increase in the amount of carbonate ion produced in the liquid phase, see Figure 69. This effect is produced by

the increased reaction rate produced by the increased amount of  $\text{CO}_2$  transferred into the liquid phase.

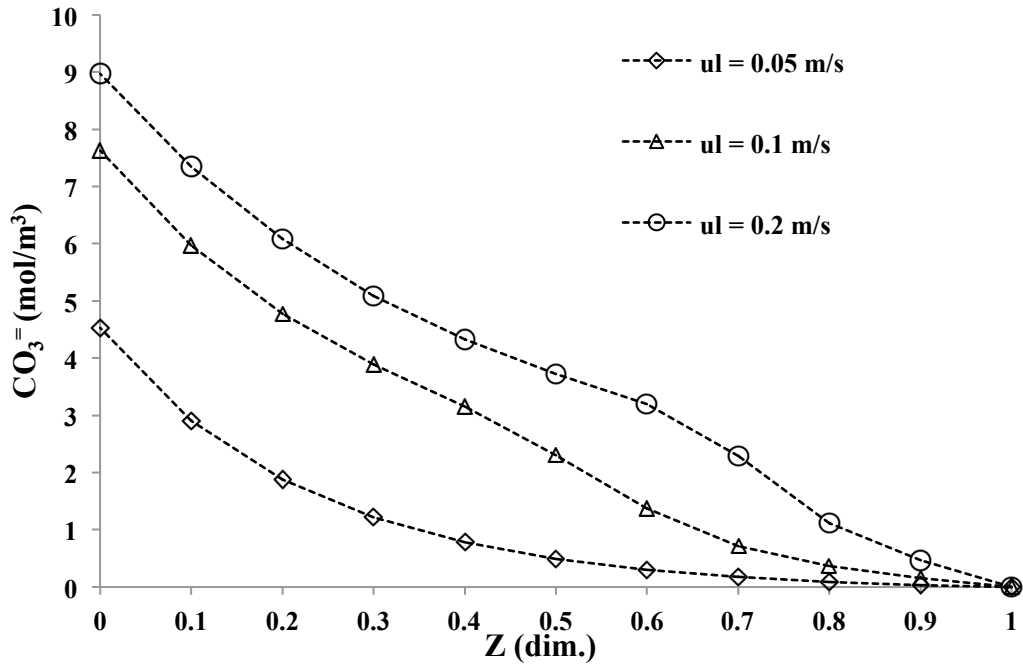


**Figure 67. Influence of the liquid phase superficial velocity ( $u_l$ ) on the carbonate ion profile.**

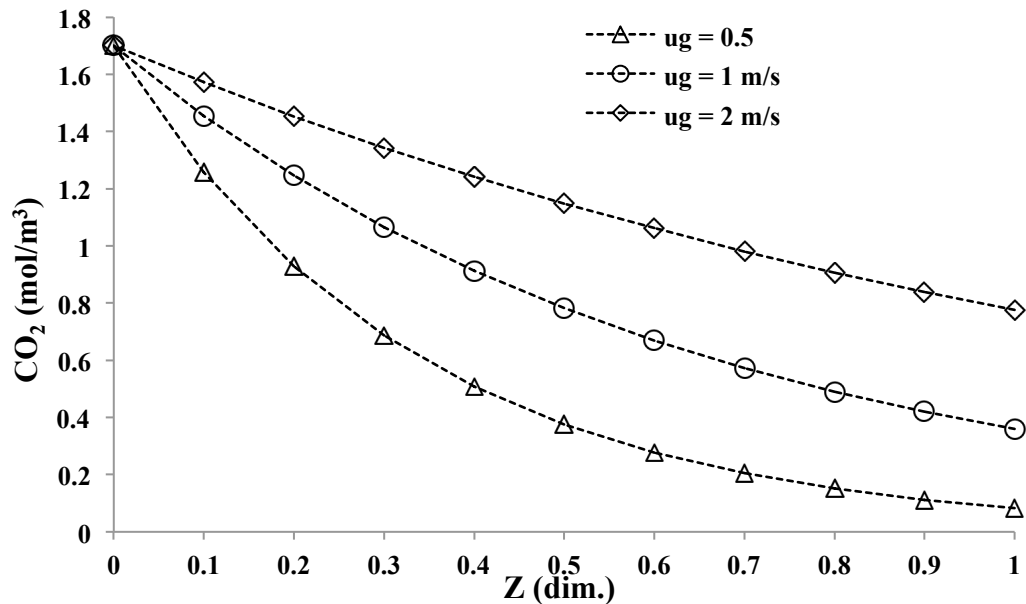


**Figure 68. Influence of the gas phase superficial velocity ( $u_g$ ) on the  $\text{CO}_2$  profile.**

The influence of the gas velocity is shown in Figure 70. It is shown that the concentration of carbon dioxide decreases as the gas velocity decreases. The decrease in gas velocity increases the residence time of  $\text{CO}_2$  in the column and; therefore, the amount consumed increases too.

The effect of column height is depicted in Figures 71 and 72. Steady-state values of the gas phase concentration profiles are compared at different column heights. In Figure 71 we can see that higher columns heights decrease the amount of CO<sub>2</sub> in gas phase. Therefore, the amount absorbed increases with the increased in height.

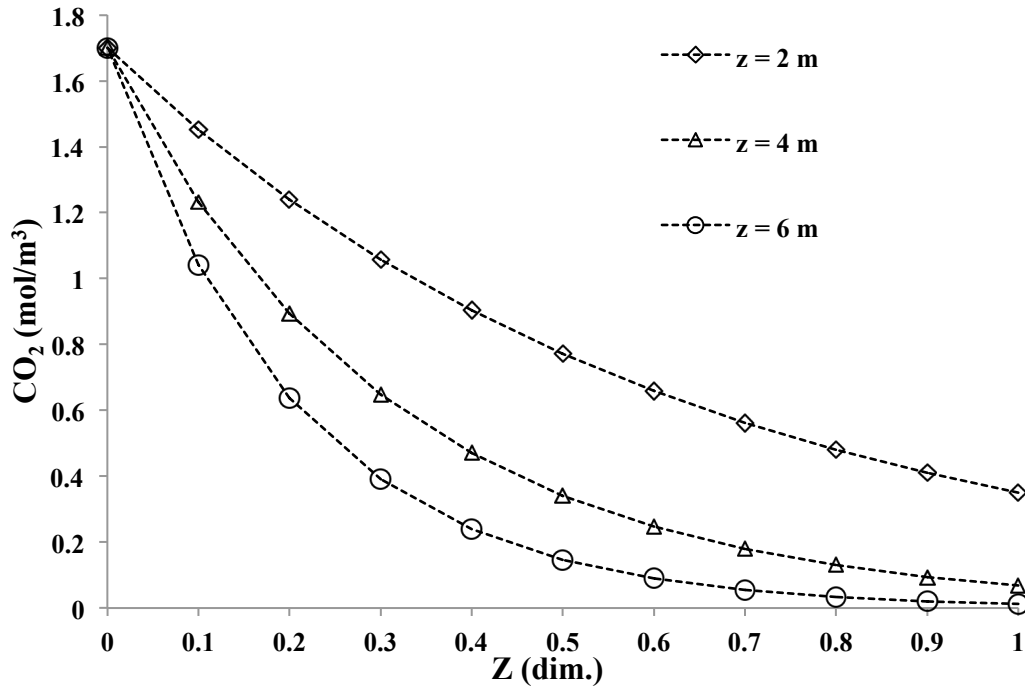


Figure 69. CO<sub>2</sub> profile as a function of dimensionless column height (z).

#### 4.4.2.4 Response to Changes in Input Parameters

The true test for a dynamic simulator is given by how it describes sudden changes in input parameters. In order to test our model we simulate the response to two sudden changes in input CO<sub>2</sub> concentrations, a step and a discrete pulse.

In the case of a step change in input concentration we assumed that the column reaches steady-state operating conditions and at  $t=t_0$  the CO<sub>2</sub> input concentration doubles its value. The results are shown in Figures 72 and 73.

Figure 72 shows the time evolution of the CO<sub>2</sub> concentration profile until steady-state is reached, prior to the step. The CO<sub>2</sub> concentration values decrease continuously as time increases until reaching their steady-state values. The steady-state profile (solid black line) is the starting point for the simulation of the step change.

Figure 73 shows that the CO<sub>2</sub> gas phase concentration starts increasing in value from the bottom of the column (input) towards the top (output) until a new equilibrium is achieved at higher values. There is a continuous gradual increase in CO<sub>2</sub> concentration until the new steady-state values are reached. The area between both curves is proportional to the amount of extra mass added.

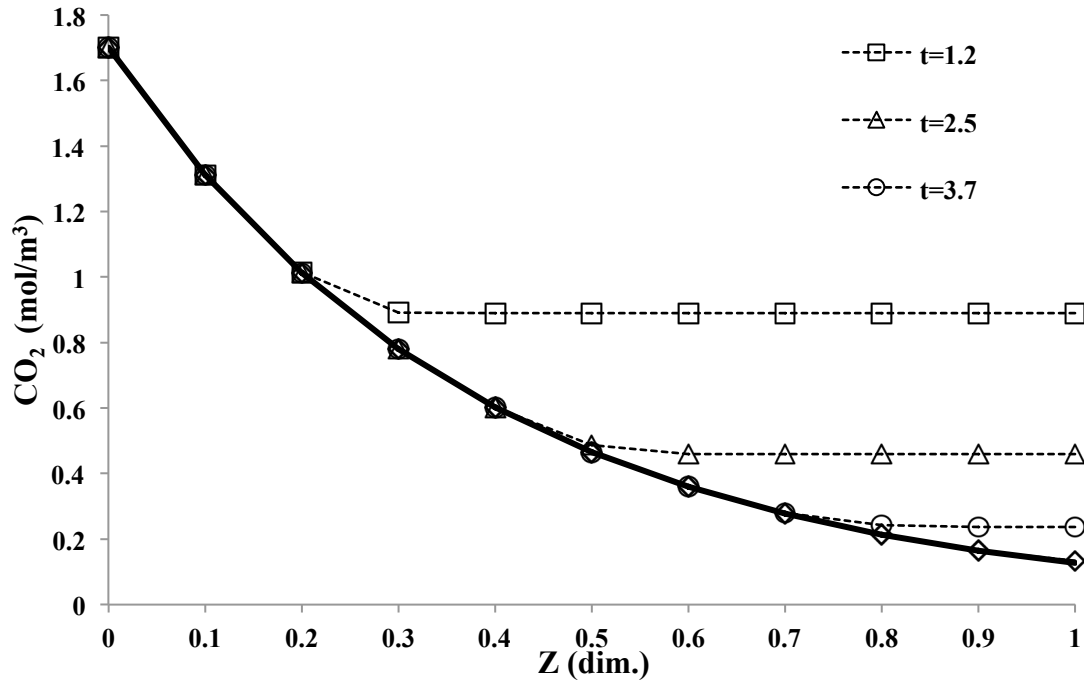


Figure 70. Time evolution of the CO<sub>2</sub> profile until reaching steady-state.

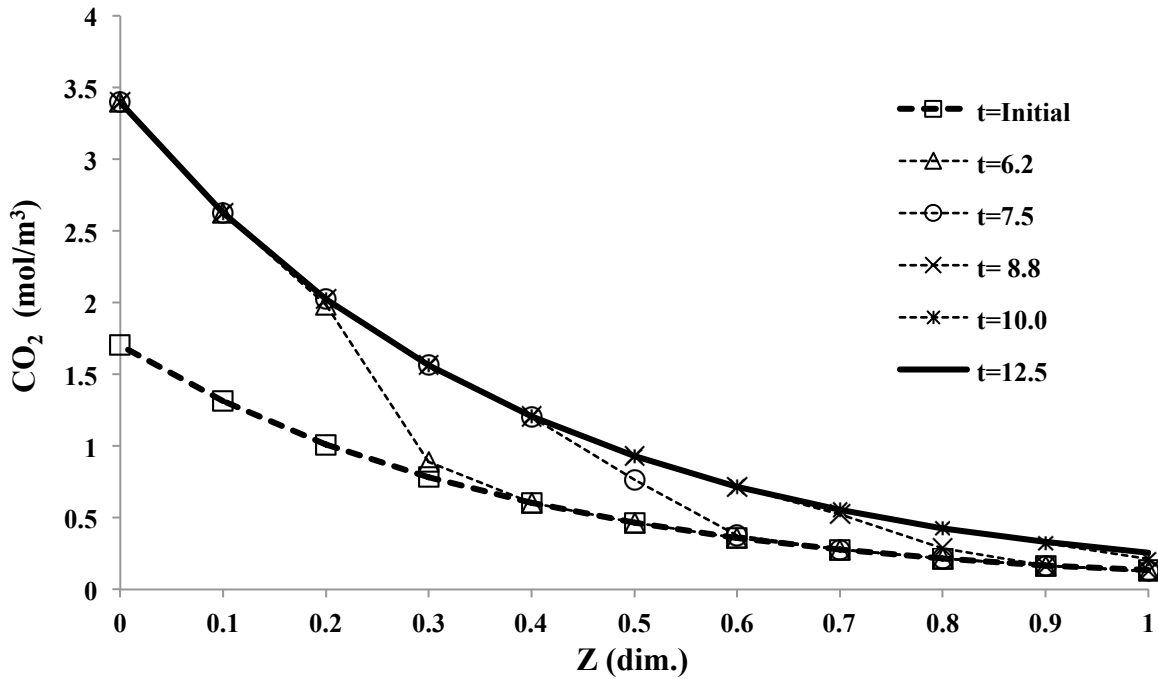


Figure 71. Dynamic change of the CO<sub>2</sub> profile produced by a doubling of the input CO<sub>2</sub> concentration.

In order to simulate the discrete pulse we start from the steady-state shown in Figure 72, at  $t=t_0$  we double the CO<sub>2</sub> input concentration, but at  $t=t_1$  we reduce the CO<sub>2</sub> input concentration to its original value. The results are shown in Figures 74 and 75.

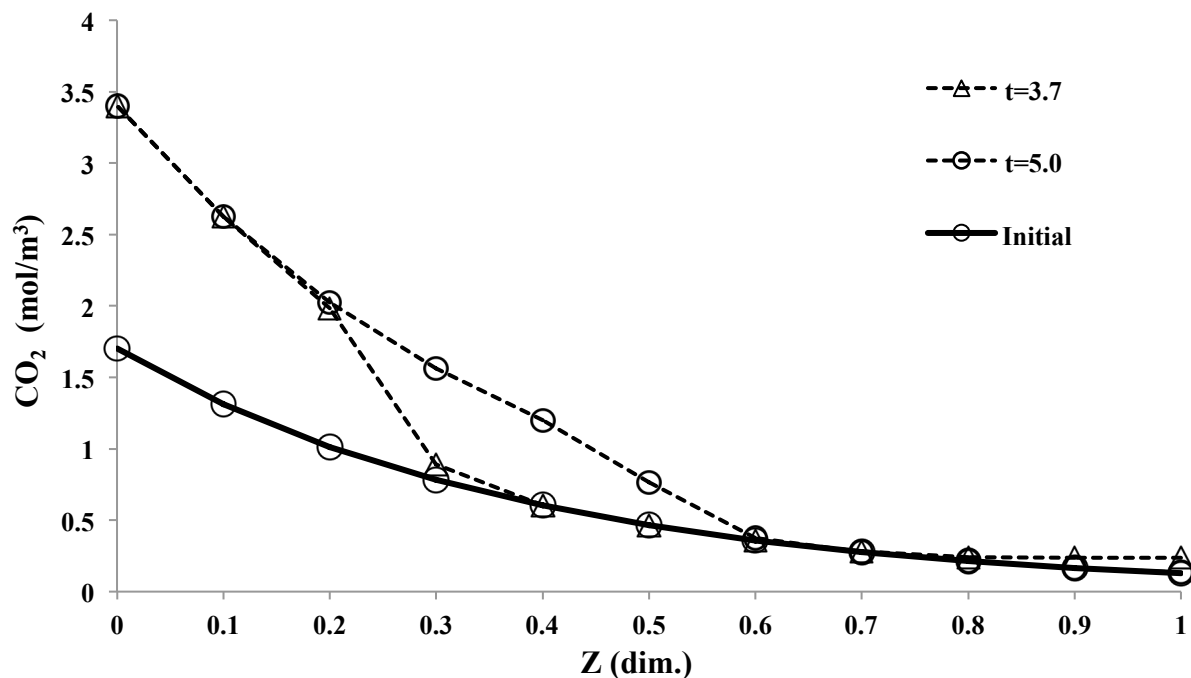


Figure 72. Dynamic change of the CO<sub>2</sub> profile between  $t = t_0$  and  $t = t_1$ .

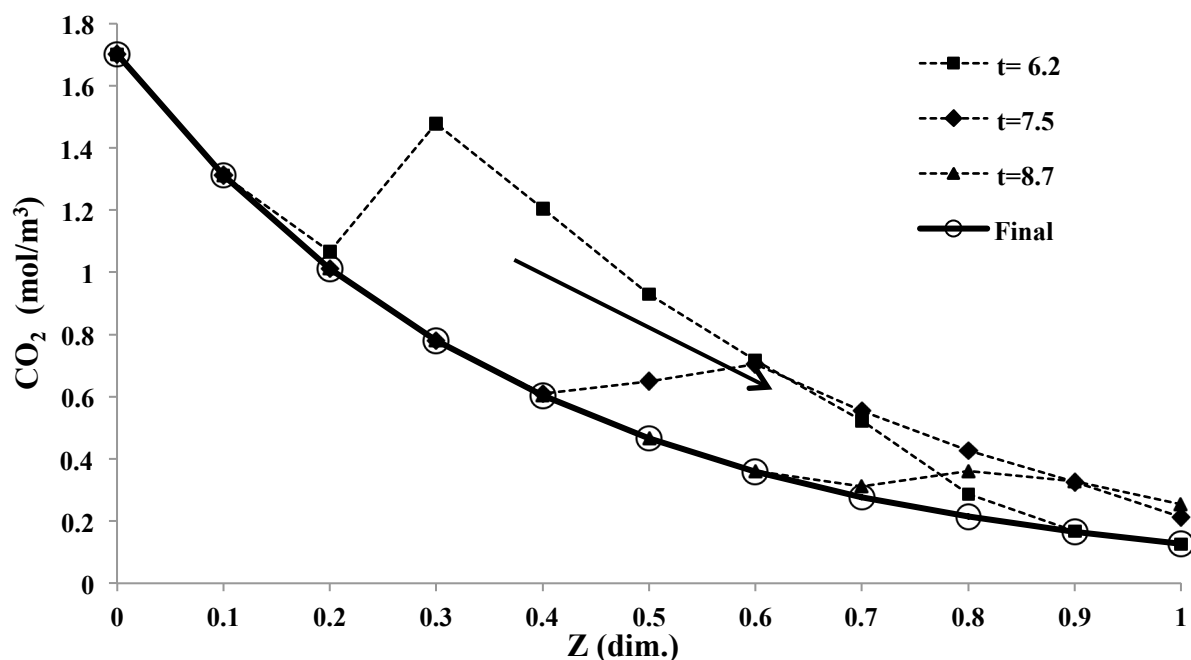
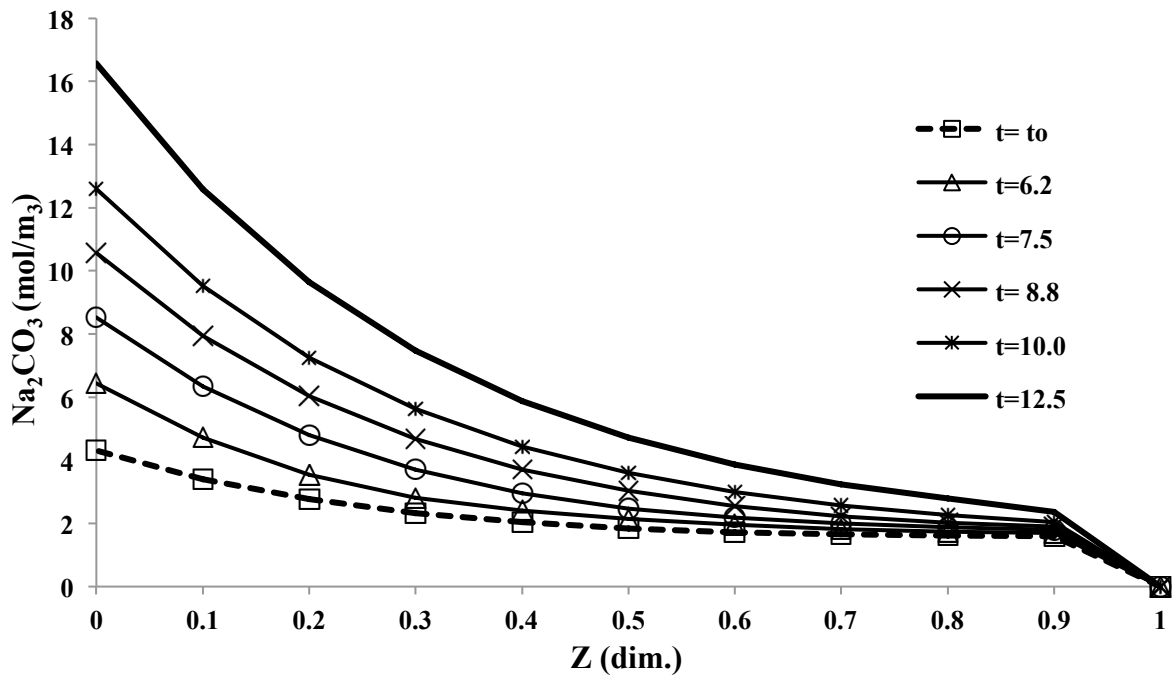


Figure 73. Dynamic change of the CO<sub>2</sub> profile after  $t = t_1$ .

Figure 74 shows that after  $t = t_0$  the dynamic behavior is similar to the one for the step. The CO<sub>2</sub> concentration increases continuously with time from the bottom of the column to the top. The solid line represents the initial steady-state. The area between the initial steady-state curve

and the  $\text{CO}_2$  concentration profile at each particular time represents the extra  $\text{CO}_2$  mass injected during the pulse and increases continuously with time. After  $t = t_1$  the  $\text{CO}_2$  input concentration is restored to its original value and the  $\text{CO}_2$  concentration starts decreasing throughout the column. This behavior is more noticeable in the bottom of the column as the extra amount of  $\text{CO}_2$  injected during the pulse travels through the column. The solid line in Figure 75 represents the new steady-value to be reached and the area in between the steady-state curve and the  $\text{CO}_2$  concentration profile at a particular time represents the remaining extra  $\text{CO}_2$  mass injected during the pulse. Figure 75 shows that after  $t = t_1$  the area between the  $\text{CO}_2$  decreases continuously with time until the original steady-state is reached. At this point in time all the mass injected by the pulse has been absorbed and removed from the gas phase.

In the case of the carbonate ion produced in the liquid phase we can see in Figure 76 that the mass introduced into the column by the pulse produces a continuous increase in the  $\text{CO}_2$  concentration above the steady-state value at  $t = t_0$ . Eventually, this extra amount of mass will leave the liquid phase; however, we have to remember that the liquid phase has a higher residence time than the gas phase due to its smaller superficial velocity.



**Figure 74. Dynamic behavior of the  $\text{Na}_2\text{CO}_3$  profile during pulse injection.**

Figures 77 and 78 depict the time evolution of the gas phase pulse in input  $\text{CO}_2$  concentration using contour plots where time is plotted as the third variable. In both Figures the horizontal axis depicts the dimensionless time, from left to right. The volume enclosed by the plotted 3-D surface is directly proportional to the injected amount of  $\text{CO}_2$ . Planes perpendicular to the horizontal axis show the concentration profile inside the column at that time value.

In Figure 77 the depth axis depicts the dimensionless height of the column from top ( $z=0$ ) to bottom ( $z=1$ ). The vertical axis shows  $\text{CO}_2$  concentration values in gas phase. The results on the back wall ( $z=1$ ) represent the input  $\text{CO}_2$  concentration values,  $C_{\text{CO}_2} = 1.7 \text{ mol/m}^3$ . The left side wall ( $t=0$ ) represents the initial condition inside the column.

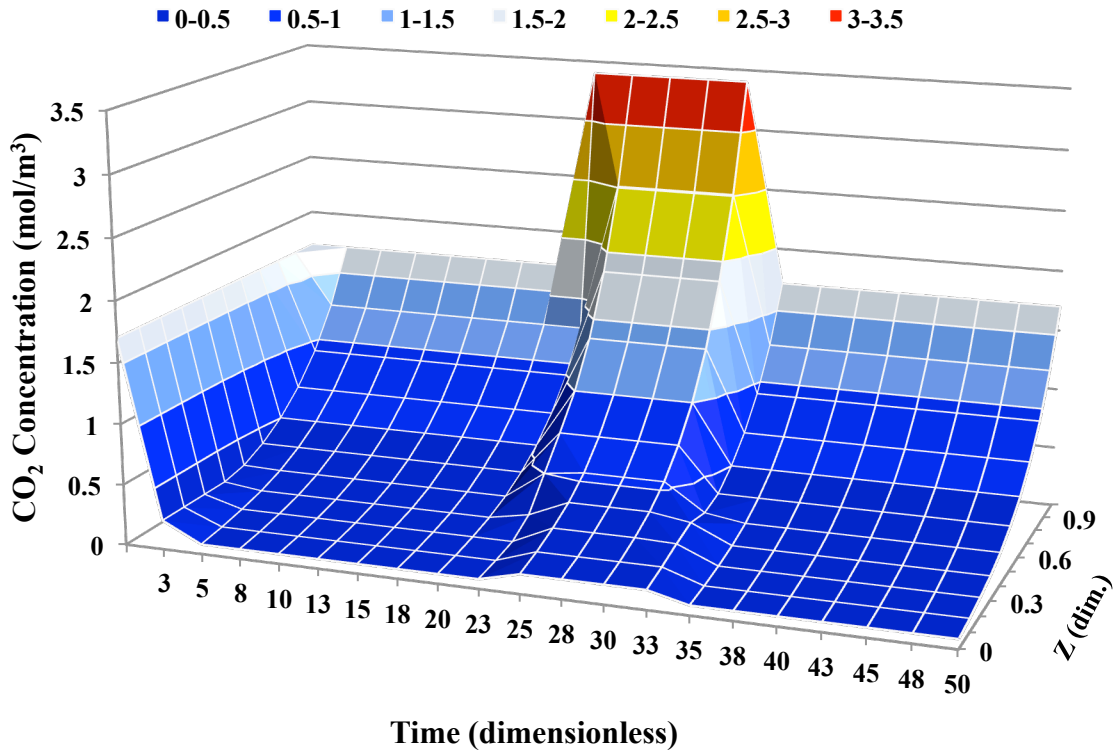


**Figure 75. Contour plot showing the time evolution of the discrete  $\text{CO}_2$  pulse in gas phase.**

The pulse injection begins at  $t=20$  and lasts until  $t=30$ . In Figure 77 we can see that before the start of the pulse the system reaches steady-state. After the pulse injection,  $t=20$ , the system reaches a new steady-state by  $t = 25$ . The original steady-state is reached after  $\text{CO}_2$  input is restored to the original value.

A similar contour plot for the  $\text{Na}_2\text{CO}_3$  concentration in liquid phase is depicted in Figure 78. In the Figure the depth axis depicts the dimensionless height of the column from the top ( $z = 1$ ) to bottom ( $z=0$ ). The vertical axis shows  $\text{Na}_2\text{CO}_3$  concentration values in liquid phase. The results on the back wall ( $z = 1$ ) represent the output  $\text{Na}_2\text{CO}_3$  concentration, and the front ( $z = 0$ ) shows the input concentration equal to zero.

The results in Figure 78 confirm that before the pulse steady-state is reached in liquid phase by a more complex process that in the case of the gas phase, see Figure 67. After the start of the pulse,  $t=20$ , the output concentration at the bottom ( $z = 1$ ) increases continuously until reaching a maximum value at  $t=30$ . After the  $\text{CO}_2$  injection in gas phase is restored to its original value ( $t=30$ ), the output concentration decreases continuously until the original steady-state value is

reached at  $t=50$ . It takes longer to reach steady-state in the liquid phase than in the gas phase due to the smaller residence time.

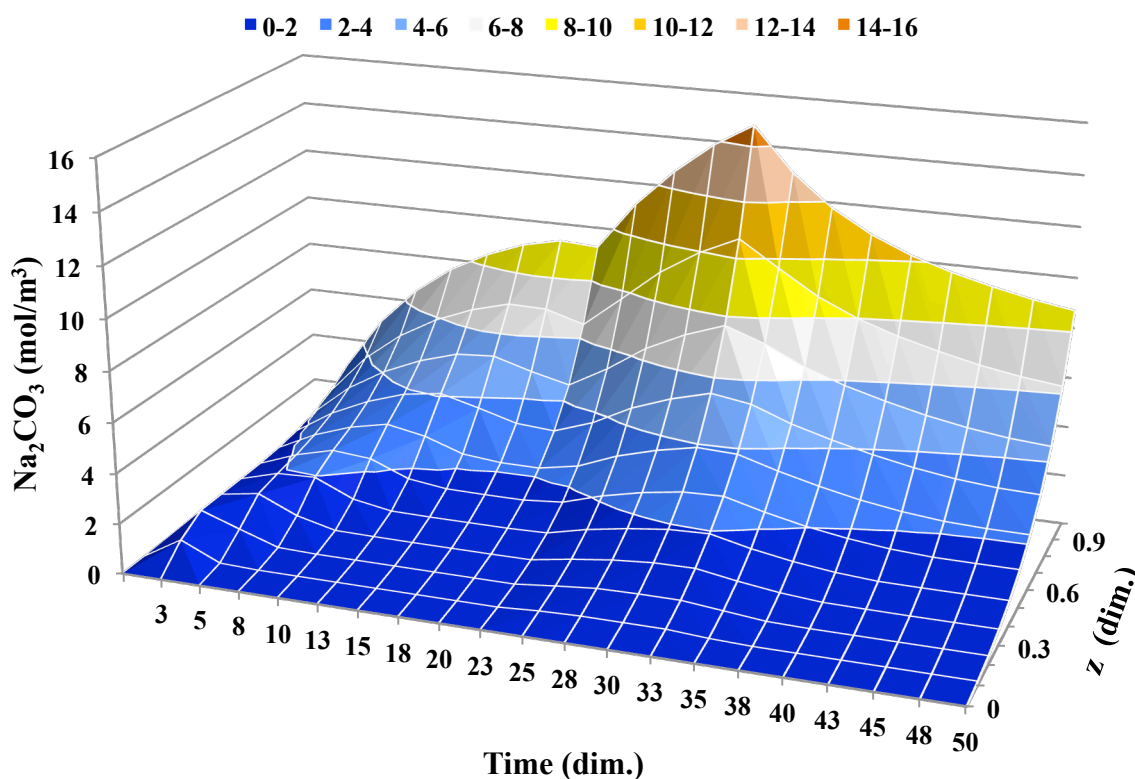


**Figure 76.** Contour plot showing the time evolution of the discrete  $\text{CO}_2$  pulse in liquid phase.

These results prove that the computer code can simulate complex dynamic behavior. In conclusion, we can say that the model seems to be versatile enough to capture the fine details of the dynamic behavior.

### 3.6 Summary

A model for the dynamic behavior of reactive  $\text{CO}_2$  absorption has been successfully developed. The model is based upon transient mass and energy balances for several different chemical species commonly present in  $\text{CO}_2$  gas-liquid absorption. Phase equilibrium has been considered using a thermodynamic model and through the use of experimentally based Henry's law values. Typical values for the geometric parameters of the absorber and the packing characteristics have been collected. A computer code has been written to implement the proposed model. Several versions of the computer code has been written, steady-state operation, isothermal mass balance only, and combined mass and energy balances. The computer code has



been properly validated by thoroughly checking all the values of parameters calculated and comparing results to literature.

An experimental program has been also carried out as part of this project. The experimental program determined values of liquid phase mass transfer coefficients with and without chemical reactions. Data were measured and compared with literature values. The values of the mass transfer coefficients were used in the simulations.

An energy balance routine calculates temperature profiles. Computed results show that for most typical applications in this project only minor temperature variations occur; therefore, even an isothermal version of the model presented here will give acceptable results. This effect is due to the small values of the concentration of the limiting reactant ( $\text{CO}_2$ ). In other applications, where higher values of  $\text{CO}_2$  are used, temperature variations can be significant.

All our simulations show that the dynamic results converge to the steady state solution after a transient period. The model has been used to study the influence of operating parameters. Results demonstrate that the absorbed amount of carbon dioxide increases as the gas superficial velocity decreases and the liquid superficial velocity increases. The amount of  $\text{CO}_2$  absorbed also increases as the column height increases. The calculated carbonate concentration profiles in liquid phase confirmed the conclusions drawn using the computed  $\text{CO}_2$  concentration profiles in gas phase. These results are logical and comply with physical expectations.

The model was used to simulate complex dynamic conditions such as, step changes and discrete pulses in concentration inputs. The computed results throughout this project showed that the model is versatile enough to capture the fine details of the dynamic processes.

In conclusion, this model can be used for successful simulations of  $\text{CO}_2$  absorption processes.

## REFERENCES

### References for Section 1

1. P. Filss, Sampling and Counting Tritiated Water Vapor from Radioactive Off-gas Streams by Adsorption of Silica Gel, *Radiochem. Radioanal. Lett.*, 15(3), 213 (1973).
2. L.L. Burger and J.L. Ryan, The Technology of Tritium Fixation and Storage, Tech. Report No. BNWL-1807, Battelle Pacific Northwest Laboratories, Richland, Washington (1973).
3. J.H. Good, R.D. Baybarz, S.D. Clinton, L.G. Farrar, C.L. Fitzgerald, R.G. Haire, V.J. Tennery, V.C.A. Vaughen and C.D. Watson, Voloxidation – Removal of Volatile Fission Products from Spent LMFBF Fuels, Tech. Report No. ORNL-TM-3723, Oak Ridge National Laboratories (1973).
4. S. Tanaka and Y. Yamamoto, Removal of Tritiated Water Vapor by Adsorption, *J. Nucl. Sci. Technol.*, 13, 251 (1976).
5. W.D. Holland, A.H. Shah, A.F. Kaiser and J.C. McGee, Experimental Studies Concerning the Drying of Voloxidizer Off-gases, Tech. Report No. ORNL/SUB-7164/1, Tennessee Technological University, Cookeville (1981).
6. M. Nakashima, E. Tachikawa, M. Saeki and Y. Aratono, Removal Mechanism of Tritium by Various Pretreated Silica Gel, *J. Inorg. Nucl. Chem.*, 43, 369 (1981).
7. M. Nakashima and E. Tachikawa, Removal of Tritiated Water Vapor by Molecular Sieves 5A and 13X, Silica-gel and Activated Alumina, *J. Nucl. Sci. Technol.*, 19, 571 (1982).
8. S. Tanaka, F. Ono, Y. Takahashi and R. Kiyose, Removal of Tritiated Water Vapor by Adsorption on Molecular Sieves: Effect of Co-existing H<sub>2</sub>O, *Fusion Technol.*, 8, 2196 (1985).
9. M. Llano-Restrepo and M.A. Mosquera, Accurate correlation, thermochemistry, and structural interpretation of equilibrium adsorption isotherms of water vapor in zeolite 3A by means of a generalized statistical thermodynamic adsorption model, *Fluid Phase Equilibria* 283 (1–2), 73–88 (2009).
10. W.R. Grace & Co., Grace Davison: Sylobead Adsorbents for Process Applications, Columbia, Maryland, p. 11 (2002).
11. Gleuckauf, E.; Coates, J. I. Theory of chromatography. Part IV. The influence of incomplete equilibrium on the front boundary of chromatograms and on the effectiveness of separation. *J Chem Soc.*, 0, 1315-1321 (1947).
12. Ruthven, D. M. *Principles of adsorption and adsorption processes (1st edition)*; Wiley-Interscience: New York (1984).
13. R.T. Jubin, The Mass Transfer Dynamics of Gaseous Methyl-iodide Adsorption by Silver-exchanged Sodium Mordenite, Ph.D dissertation, The University of Tennessee (1994).
14. S. Sircar and J.R. Hufton, Why Does the Linear Driving Force Model for Adsorption Kinetics Work? *Adsorption*, 6(2), 137 (2000).

15. Plazinski, W.; Rudzinski, W.; Plazinska, A. Theoretical models of sorption kinetics including a surface reaction mechanism: A review. *Adv Colloid Interface Sci.* 152, 2–13 (2009).
16. Y.-S. Ho, Review of second-order models for adsorption systems, *Journal of Hazardous Materials B*, 136, 681–689 (2006).
17. H. Qiu, L.Lv, B. Pan, Q. Zhang, W. Zhang and Q. Zhang, Critical review in adsorption kinetic models, *J Zhejiang Univ Sci A*, 10(5), 716-724 (2009).
18. R. Lin, J. Liu, Y. Nan, D. W. DePaoli, and L. L. Tavlarides. Kinetics of Water Vapor Adsorption on Single-Layer Molecular Sieve 3A: Experiments and Modeling. *Industrial & Engineering Chemistry Research*, 53(41), 16015-16024 (2014).
19. Langmuir, I. The adsorption of gases on plane surfaces of glass, mica and platinum. *J Am Chem Soc.* 40, 1361-1403 (1918).
20. Ranz, W. E.; Marshall, W. R. Evaporation from drops. *Chem Eng Progress.* 48, 141-146 (1952).
21. Poling, B. E.; Prausnitz, J. M.; O'Connell, J. P. *The properties of gases and liquids (5th edition)*. McGraw-Hill: New York (2000).
22. Lemmon, E. W.; Huber, M. L.; McLinden, M. O. NIST standard reference database 23: Reference fluid thermodynamic and transport properties – REFPROP, Version 9.0. (2010).
23. Sircar, S. Linear-driving-force model for non-isothermal gas adsorption kinetics, *J Chem Soc Faraday Trans.* 79, 785-796 (1983).
24. Do, D. D. *Adsorption analysis: Equilibria and kinetics*. Imperial College Press: London, (1998).
25. Dzhigit, O. M.; Kiselev, A. V.; Mikos, K. N.; Muttik, G. G.; Rahmanova, T. A. Heats of adsorption of water vapour on X-zeolites containing  $\text{Li}^+$ ,  $\text{Na}^+$ ,  $\text{K}^+$ ,  $\text{Rb}^+$ , and  $\text{Cs}^+$  cations. *Trans Faraday Soc.* 67, 458-467 (1971).
26. Moise, J. C.; Bellat, J. P.; Méthivier, A. Adsorption of water vapor on X and Y zeolites exchanged with barium. *Micropor Mesopor Mat.* 43, 91-101 (2001).
27. Llano-Restrepo, M.; Mosquera, M. A. Accurate correlation, thermochemistry, and structural interpretation of equilibrium adsorption isotherms of water vapor in zeolite 3A by means of a generalized statistical thermodynamic adsorption model. *Fluid Phase Equilib.* 283, 73-88 (2009).

## References for Section 2

1. Do, D.D., “Analysis of Adsorption Kinetics in a Zeolite Particle”, *Adsorption Analysis: Equilibria and Kinetics*, Imperial College Press: London, (1998).
2. Do, H.D.; Do, D.D.; Prasetyo, I., *Chem. Eng. Sci.*, 56, p. 4351-4368, (2001).
3. Fernandez, C.A.; Liu, J.; Thallapally, P.K.; Strachan, D.M.; “Switching Kr/Xe Selectivity with Temperature in a Metal-Organic Framework”, *JACS*, 134, p. 9046-9049, (2012).

4. Gaston, D.; Newman, C.; Hansen, G.; Lebrun-Grandie, D., "MOOSE: A parallel computational framework for coupled systems of nonlinear equations". *Nuclear Engineering and Design*, 239, 1768 – 1778 (2009).
5. Grace Davison, Sylobead Adsorbents for Process Applications, (2002).
6. Jubin, R. T., "The Mass Transfer Dynamics of Gaseous Methly-Iodide Adsorption by Silver-Exchanged Sodium Mordenite", *PhD Dissertation*, University of Tennessee, December, (1994).
7. Knoll, D.A. and Keyes, D.E., "Jacobian-Free Newton-Krylov methods: a survey of approaches and applications", *J. Comp. Physics*, 193, 357-397, (2004).
8. Krieger, F.J., "Calculation of the Viscosity of Gas Mixtures", *U.S. Air Force: Project RAND Research Memorandum*, RM-649, (1951).
9. Kumar, A.; Jaiswal, D.K.; Kumar, N.; "Analytical Solutions of One-Dimensional Advection-Diffusion Equation with Variable Coefficients in a Finite Domain", *J. Earth Syst. Sci.*, 118, 539-549, (2009).
10. Kurganov, A. and Tadmor, E., "New High-Resolution Central Schemes for Nonlinear Conservation Laws and Convection-Diffusion Equations", *J. of Comp. Phy.*, 160, 241-282, (2000).
11. Llano-Restrepo, M.; Mosquera, M. A., "Accurate correlation, thermochemistry, and structural interpretation of equilibrium adsorption isotherms of water vapor in zeolite 3A by means of a generalized statistical thermodynamic adsorption model". *Fluid Phase Equilibria*, 283, 73-88 (2009).
12. Madsen K., H.B. Nielsen, O. Tingleff, *Methods for Non-Linear Least Squares Problems*, Informatics and Mathematical Modeling, Technical University of Denmark, (2004).
13. Malek, A. and Farooq, S. "Kinetics of Hydrocarbon Adsorption on Activated Carbon and Silica Gel", *AIChE J.*, 43, 761-776, (1997).
14. Markowitz, H., "Mean-Variance Approximations to the Geometric Mean", *Annals of Financial Economics*, 7, No. 1, (2012).
15. Myers AL, Prausnitz JM. *AIChE Journal*. 34,121-127, (1965).
16. Ritter, J.A. and Yang, R.T., "Equilibrium Adsorption of Multicomponent Gas Mixtures at Elevated Pressures", *Ind. Eng. Chem. Res.*, 26, 1679-1686, (1987).
17. Rivi re, B. *Discontinuous Galerkin Methods for Solving Elliptic and Parabolic Equations: Theory and Implementation*, SIAM, Frontiers in Applied Mathematics, (2008).
18. Rutledge, V., "OSPREY Model", *U.S. DOE: Separations and Waste Forms*, Idaho National Laboratory, January 25th (2013).
19. Saad, Y., *Iterative Methods for Sparse Linear Systems*, 2nd Ed., SIAM, (2003).
20. Sakuth, M.; Meyer; J. Gmehling, J., *Chem. Eng. & Process*, 37, 267-277, (1998).
21. Sedl  ek, Z., "Isosteric adsorption heats in correlation with activation energy of diffusion", *Chem. zvesti*, 29, 344-349, (1975).

22. Simo, M., Sivashanmugam, S. Brown, C.J., and Hlavacek, V., "Adsorption/Desorption of Water and Ethanol on 3A Zeolite in Near Adiabatic Fixed Bed", *Ind. Eng. Chem. Res.*, 48, 9247-9260, (2009).
23. Sutherland, W., "The Viscosity of Gases and Molecular Force", *Philosophical Magazine*, 36, 507-531, (1893).
24. Talu, O. and Myers, A.L., "Rigorous Thermodynamic Treatment of Gas Adsorption", *AIChE Journal*, 34, 1887-1893, (1988).
25. Talu, O. and Zwiebel, I., "Multicomponent Adsorption Equilibria of Nonideal Mixtures", *AIChE Journal*, 32, 1263-1276, (1986).
26. Thomas, J. W., *Introduction to Numerical Methods for Partial Differential Equations*, Springer, (1995).
27. Tien, C., *Adsorption Calculations and Modeling*, Butterworth-Heinemann Series in Chemical Engineering, (1994).
28. Wakao, N.; Funazkri, T. "Effect of fluid dispersion coefficients on particle-to-fluid mass transfer coefficients in packed beds: Correlation of sherwood numbers", *Chemical Engineering Science*, 33, 1375–1384, (1978).
29. Wilke, C.R., "A Viscosity Equation for Gas Mixtures", *J. Chem. Phys.*, 18, 517-519, (1950).
30. Wuttke, J., lmfit -Version <lmfit-3.4>, <http://joachimwuttke.de/lmfit/>, retrieved on January 21st, (2013).
31. Zienkiewicz, O.C. and Taylor, R.L., *The Finite Element Method: Volume 3: Fluid Dynamics*, Fifth Ed., Butterworth-Heinemann, (2000).

### References for Section 3

1. Freguia, S.; Rochelle, G. T. Modeling of CO<sub>2</sub> capture by aqueous monoethanolamine. *AIChE J.* **2003**, 49 (7), 7, 1676–1686.
2. Greer, T., Bedelbayev, A., Igreja, J. M., Pereira Gomes, J. F. and Lie, B. "A dynamic model for the de-absorption of carbon dioxide from monoethanolamine solution," *Proceedings SIMS 2008*, Oslo University College, October 7-8, 2008.
3. Greer, T., "Modeling and simulation of post combustion CO<sub>2</sub> capturing," Ms. Thesis, Telemark University College, Faculty of Technology, 2008.
4. Bedelbayev, A., Greer, T., and Lie, B. "Model based control of absorption tower for carbon dioxide capturing," *Proceedings SIMS 2008*, Oslo University College, October 7-8, 1420-1440, 2008.
5. Lawal, A., Wang, M., Stephenson, P., and Yeubg, H., "Dynamic modeling of CO<sub>2</sub>-absorption for post combustion capture in coal-fired power plants," *Fuel*, **88** (12), 2455-2462, 2009.
6. Onda, K., Kobayashi, T., Fujine, M., and Takahashi, M. "Behavior of the reaction plane movement in gas absorption accompanied by instantaneous chemical reactions. *Chem. Eng. Sci.*, **26**, 2009-2026, 1971.

7. Hikita, H., Asai, S., and Takatsuka, T. "Absorption of carbon dioxide into aqueous sodium hydroxide and sodium carbonate-bicarbonate solutions." *The Chem. Eng. Journal*, **4**, 31-40, 1972.
8. Hikita, H., Asai, S., and Takatsuka, T. "Gas absorption with a two-step instantaneous chemical reaction." *The Chem. Eng. Journal*, **11**, 131-141, 1976.
9. Hikita, H., Asai, S., and Takatsuka, T. "Absorption of carbon dioxide into aqueous sodium hydroxide and sodium carbonate-bicarbonate solutions." *The Chem. Eng. Journal*, **4**, 31-40, 1972.
10. Hikita, H., Asai, S., and Takatsuka, T. "Absorption of carbon dioxide into aqueous sodium hydroxide and sodium carbonate-bicarbonate solutions." *The Chem. Eng. Journal*, **4**, 31-40, 1972.
11. Perry R. H. and Green D. W., *Chemical Engineers Handbook*. 7<sup>th</sup> edition, McGraw-Hill, New York, 1999.
12. Prausnitz, J. M., Lichtenthaler, R. N., and Gomes de Azevedo, E., *Molecular thermodynamics of fluid-phase equilibria*, 3rd edition, Prentice Hall, 1998.
13. Mason, E. A., and Spurling, T. H., "The Virial Equation of State," Pergamon, New York, 1968.
14. Tsonopoulos, C., *AIChE J.*, **20**, 263 (1974).
15. Poling, B. A., Prausnitz, J. M., and O'Connell, J. P., "The Properties of Gases and Liquids," Prentice-Hall Inc., McGraw Hill, N.Y., 2001.
16. Sandler, R. "Compilation of Henry's Law Constants for Inorganic and Organic Species of Potential Importance in Environmental Chemistry." Downloaded from: <http://www.mpch-mainz.mpg.de/~sander/res/henry.html>, 1999.
17. Zeman, F., "Energy and material balance of CO<sub>2</sub> capture from ambient air," *Environ. Sci. Technol.*, **41**, 7558-7563, 2007.
18. Reid, R. C., Prausnitz J. M., and Poling, B. E. "The Properties of Gases and Liquids." New York: McGraw-Hill. Fourth edition, 1987.
19. Backhurst, J. R., Harker, J. H., Richardson, J. F., Coulson, J. M. "Coulson and Richardson's Chemical Engineering," Volume 1, 6th edition, Butterworth-Heinemann, 1999.
20. DeWitt, D. P. and Incropera, T. P. "Fundamentals of Heat and Mass Transfer." Fifth edition, John Wiley & Sons, 2002.
21. Thomas, J. W. "Numerical Partial Differential Equations; Finite Difference Methods," Springer-Verlag, New York Inc., 1995.
22. Computer Controlled Gas Absorption Column. Edibon, Technical Teaching Equipment, 2010 catalog downloadable from: <http://www.edibon.com/products/catalogues/en/units/chemicalengineering/chemicalengineeringbasic/CAGC.pdf>.

23. Richardson, J. H., Harker, J. H., and Backhurst, J. R. "Chemical Engineering. Vol. 2, Particle Technology and Separation Processes." Oxford; Burlington: Butterworth-Heinemann, publishers, 5<sup>th</sup> edition, 2008.
24. Billet, R. and Schultes, M. "Prediction of mass transfer columns with dumped and arranged packing's: Updated Summary of the Calculation Method of Billet and Schultes." *Trans. IChemE.* , **77**, 1999.
25. Onda, K., Takeuchi, H., and Okumoto, Y. "Mass Transfer Coefficients between Gas and Liquid Phases in Packed Columns." *Journal of Chem. Eng. Japan*, **1** (2), 56-62, 1968.

## Publications and Presentations

### Publications

1. R. Lin, L. L. Tavlarides, "Removal of Water and Iodine by Solid Adsorbents: Adsorption Isotherms and Kinetics", *Global 2013 International Nuclear Fuel Cycle Conference*, Salt Lake City, Utah, USA, September 29 – October 3, 2013. (Published in refereed proceedings.)
2. A. Ladshaw, K. Sharma, S. Yiacoumi, C. Tsouris, "Adsorption Modeling for Off-Gas Treatment", *Global 2013 International Nuclear Fuel Cycle Conference*, Salt Lake City, Utah, USA, September 29 – October 3, 2013. (Published in refereed proceedings.)
3. V. Rutledge, L. Tavlarides, R. Lin, A. Ladshaw, "Tritium Specific Adsorption Simulation Utilizing the OSPREY Model," INL/EXT-13-30274, Sept. 2013.
4. R. Lin, J. Liu, Y. Nan, D. W. DePaoli, and L. L. Tavlarides. "Kinetics of Water Vapor Adsorption on Single-Layer Molecular Sieve 3A: Experiments and Modeling", *Industrial & Engineering Chemistry Research*, 53(41), 16015-16024 (2014).
5. L. M. Pompilio, D. W. DePaoli, B. B. Spencer, "Evaluation of INL Supplied MOOSE/OSPREY Model: Modeling Water Adsorption on Type 3A Molecular Sieve," FCRD-SWF-2014-000459, August 2014.
6. A. Ladshaw, S. Yiacoumi, C. Tsouris, "A Generalized Procedure for the Prediction of Multicomponent Adsorption Equilibria", *AIChE J.*, Submitted September 2<sup>nd</sup>, 2014.
7. A. Ladshaw, S. Yiacoumi, C. Tsouris, D.W. DePaoli, "Generalized gas-solid adsorption modeling: Single-component equilibria", *Fluid Phase Equilibria*, 388, 169-181, 2015.

### Publications in preparation:

1. R. Lin, A. Ladshaw, Y. Nan, J. Liu, S. Yiacoumi, C. Tsouris, D. W. DePaoli, and L. L. Tavlarides. "Isotherms for Water Adsorption on Molecular Sieve 3A". In preparation. 2015.
2. V. Rutledge, J. Law, A. Ladshaw, S. Yiacoumi, D.W. DePaoli, C. Tsouris, "Off-gas Adsorption Model Capabilities and Recommendations", *U.S. Department of Energy Material Recovery and Waste Form Development*, in preparation.
3. J. Gabitto, "Dynamic Simulation of CO<sub>2</sub> using Concentrated NaOH Solutions in Packed Towers," in preparation, 2015

### Presentations

1. R. Lin and L.L. Tavlarides, "Removal of radioactive iodine species by solid sorbents", *AIChE 2012 Annual Meeting*, Pittsburgh, PA, USA, October 28 – November 2, 2012.
2. R. Lin, L. L. Tavlarides, "Removal of Water and Iodine by Solid Adsorbents: Adsorption Isotherms and Kinetics", *Global 2013 International Nuclear Fuel Cycle Conference*, Salt Lake City, Utah, USA, September 29 – October 3, 2013.



3. A. Ladshaw, K. Sharma, S. Yiacoumi, C. Tsouris, "Adsorption Modeling for Off-Gas Treatment", *Global 2013: International Nuclear Fuel Cycle Conference*, Salt Lake City, UT, September 29<sup>th</sup> - October 3<sup>rd</sup>, 2013.
4. J. Law, V. Rutledge, L. L. Tavlarides, R. Lin, S. Yiacoumi, C. Tsouris, A.P. Ladshaw, D. DePaoli and J. Gabitto, "Adsorption Modeling: Current Status and Research Needs", *Mini Waste Form Working Group Meeting*, Salt Lake City, Utah, October 4, 2013. [Invited]
5. L.L. Tavlarides, R. Lin, "Adsorption of tritiated water from off-gases from spent fuel reprocessing plants", *AIChE 2013 Annual Meeting*, San Francisco, CA, USA, November 3 - 8, 2013.
6. A.P. Ladshaw, R. Lin, S. Yiacoumi, C. Tsouris, D.W. DePaoli, J. Gabitto, and L.L. Tavlarides, "Sorption modeling and verification for off-gas treatment", *Fuel Cycle Technologies Annual Review Meeting*, Argonne National Laboratory, November 5-7, 2013.
7. M. Babar, A. Badavi, A., Sabharwal, J.F. Gabitto, "Sorption Modeling and Verification for Off-Gas Treatment," presented at the *TAMUS Pathways Symposium* at Texas A&M University Kingsville on November 9-11, 2013.
8. A. Ladshaw, S. Yiacoumi, C. Tsouris, "A Generalized Procedure for the Prediction of Multicomponent Adsorption Equilibria", *18th Symposium on Separation Science and Technology for Energy Applications*, Oak Ridge, TN, October 27<sup>th</sup> - 30<sup>th</sup>, 2014.
9. A. Ladshaw, S. Yiacoumi, C. Tsouris, "Modeling Applications of Adsorption for Nuclear Fuel Cycle Separations", *18th Symposium on Separation Science and Technology for Energy Applications*, Oak Ridge, TN, October 27<sup>th</sup> - 30<sup>th</sup>, 2014.
10. R. Lin, Y. Nan, A. P. Ladshaw, S. Yiacoumi, C. Tsouris, D. W. DePaoli and L. L. Tavlarides. "Capture of tritiated water and radioactive iodine from spent fuel reprocessing off-gases by solid adsorbents", *18<sup>th</sup> Symposium on Separation Science and Technology for Energy Applications*, Oak Ridge National Laboratory, Oak Ridge, Tennessee, USA, October 27-30, 2014.
11. A. Ladshaw, S. Yiacoumi, C. Tsouris, D.W. DePaoli, R. Lin, L.L. Tavlarides, "Equilibrium and Kinetic Modeling for Gas Separations in Nuclear Fuel Reprocessing", *2014 AIChE Annual Meeting*, Atlanta, GA, November 16<sup>th</sup> - 21<sup>st</sup>, 2014.
12. A. Ladshaw, S. Yiacoumi, C. Tsouris, D.W. DePaoli, R. Lin, L.L. Tavlarides, "A Generalized Model for Gas-Solid Adsorption Equilibria", *2014 AIChE Annual Meeting*, Atlanta, GA, November 16<sup>th</sup> - 21<sup>st</sup>, 2014.
13. A. Ladshaw, S. Yiacoumi, C. Tsouris, "A Complete Set of Numerical Tools for Adsorption Equilibria and Diffusion Kinetics", *ACS 2014 Colloid and Surface Science Symposium*, Philadelphia, PA, June 22<sup>nd</sup> - 25<sup>th</sup>, 2014.
14. R. Lin, Y. Nan, A. P. Ladshaw, S. Yiacoumi, C. Tsouris, D. W. DePaoli and L. L. Tavlarides. "Adsorption of Water and Iodine on Molecular Sieve 3A", *AIChE 2014 Annual Meeting*, Atlanta, GA, USA, November 16-22, 2014.
15. J.F. Gabitto, C. Tsouris, "Sorption Modeling and Verification for Off-Gas Treatment," presented at the *AIChE Annual Meeting*, Atlanta, GA, November 16-21, 2014.